Coupled Models of Water on Terrestrial Planets Orbiting M-Dwarfs

A dissertation presented by

Keavin Moore

to the Department of Earth and Planetary Sciences

in partial fulfillment of the requirements for the degree of

Doctor of Philosophy

McGill University

Tiohtià:ke/Montréal, Québec

December 2023

Dissertation Advisor: Nicolas B. Cowan Keavin Moore

Coupled Models of Water on Terrestrial Planets Orbiting M-Dwarfs

Abstract

Terrestrial planets orbiting M-dwarf stars are more abundant than those orbiting Sun-like stars, but are susceptible to lose significant water to space due to higher irradiation from their host. Irradiation in the X-ray and extreme ultraviolet ("XUV") photodissociates water molecules and drives its loss to space, especially when a planet is hot and water is readily available in its upper atmosphere. In this thesis, we aim to predict surface water inventories — as a first-order proxy for habitability — throughout the lifetimes of terrestrial planets with pure water vapour atmospheres. We do this by developing a coupled model of magma oceans, deep-water cycling, and atmospheric loss. Our initial simulations provide a proof-of-concept for our hypothesis: water sequestered within the mantle can be protected from loss to space and degassed later to recover habitable surface conditions. Our model is then improved to include an early surface magma ocean. These simulations begin right after the planet's formation, when the surface is still molten and the planet is in a runaway greenhouse phase. Although water is highly soluble within the magma ocean, atmospheric loss rates are high during this phase. Once the magma ocean solidifies, surface temperatures become modest; loss to space decreases significantly, and we assume the planet shifts to plate-tectonics-driven deep-water cycling, akin to that of modern-day Earth. We also develop a model with a long-lived basal magma ocean, which could exist below the solid mantle following surface solidification and inject water into the overlying mantle for billions of years. Finally, we extend the model from Earth-mass planets to super-Earths to explore the effect of planetary mass on surface water and water partitioning between planetary reservoirs. More massive terrestrial planets are better at retaining water but tend to sequester it permanently in their mantle, sometimes leaving the surface desiccated. We find that coupled interior-surface-atmosphere models enhance planetary habitability prospects compared to previous literature results that neglected geophysical cycling and hence overestimated rates of water loss to space. Our results are important for near-term observations of M-dwarf rocky planets, and highlight the importance of studying terrestrial planets as a coupled system.

Superviseur de Thèse: Nicolas B. Cowan Keavin Moore

Modèles Couplés de l'Eau sur Planètes Terrestres en Orbite Autour des Naines-M

Abrégé

Les planètes terrestres en orbite autour d'étoiles naines-M sont plus abondantes que celles en orbite autour d'étoiles semblables au Soleil, mais elles sont susceptibles de perdre une quantité importante d'eau dans l'espace en raison de l'irradiation plus élevée de leur hôte. L'irradiation dans les rayons X et l'extrême ultraviolet ("XUV") photodissocie les molécules d'eau et entraîne leur perte dans l'espace, en particulier lorsqu'une planète est chaude et que la vapeur d'eau est disponible dans sa haute atmosphère. Dans cette thèse, nous visons à prédire l'inventaire d'eau de surface — étant un indice de premier ordre de l'habitabilité d'une planète terrestre — à traver l'évolution des planètes terrestres avec des atmosphères de vapeur d'eau pure. Pour ce faire, nous développons un modèle couplé d'océans magmatiques, de cycles d'eau profonde et de pertes atmosphériques. Nos simulations initiales fournissent une preuve de concept pour notre hypothèse : l'eau séquestrée dans le manteau peut être protégée de la perte dans l'espace et dégazée plus tard pour retrouver des conditions de surface habitables. Notre modèle est ensuite amélioré pour inclure un océan magmatique de surface précoce. Ces simulations commencent juste après la formation de la planète, lorsque la surface est encore en fusion et que la planète est en phase d'emballement de l'effet de serre. Bien que l'eau soit très soluble dans l'océan magmatique, les taux de perte atmosphérique sont élevés pendant cette phase. Une fois l'océan magmatique solidifié, les températures de surface deviennent modestes, les pertes dans l'espace diminuent considérablement et nous supposons que la planète passe à un cycle de l'eau profonde piloté par la tectonique des plaques, semblable à celui de la Terre actuelle. Nous développons également un modèle avec un océan magmatique basal de longue durée, qui pourrait exister sous le manteau solide après la solidification de la surface et injecter de l'eau dans le manteau sus-jacent pendant des milliards d'années. Enfin, nous étendons le modèle des planètes de masse terrestre aux super-Terres afin d'explorer l'effet de la masse planétaire sur l'eau de surface et la répartition de l'eau entre les réservoirs planétaires. Les planètes terrestres plus massives retiennent mieux l'eau, mais ont tendance à la séquestrer de façon permanente dans leur manteau, laissant parfois la surface desséchée. Nous constatons que les modèles couplés intérieur-surface-atmosphère améliorent les perspectives d'habitabilité des planètes par rapport aux résultats de la littérature antérieure qui négligeaient les cycles géophysiques et surestimaient donc les taux de perte d'eau dans l'espace. Nos résultats sont importants pour les observations à court terme des planètes rocheuses naines-M, et soulignent l'importance d'étudier les planètes terrestres comme un système couplé.

Contents

List of Figures

List of Tables

List of Abbreviations

atm Atmosphere
BMO Basal Magma Ocean
DL Diffusion-Limited (Escape Regime)
EL Energy-Limited (Escape Regime)
EUV Extreme-UV (Radiation)
Gyr Gigayear (1 billion or 10^9 years)
HZ Habitable Zone
JWST James Webb Space Telescope
Kepler *Kepler* space telescope
LUVOIR Large UltraViolet Optical Infrared surveyor (Telescope)
MO (Surface) Magma Ocean
MOR Mid-Ocean Ridge
Myr Megayear (1 million or 10^6 years)
PT Plate Tectonics
RG Runaway Greenhouse
RNA RiboNucleic Acid
SL Stagnant Lid
SM Solid Mantle
TESS Transiting Exoplanet Survey Satellite (Telescope)
TO Terrestrial Ocean
TRAPPIST TRAnsiting Planets and PlanetesImals Small Telescope
UV UltraViolet (Radiation)
VPLanet Virtual Planet Simulator
XUV X-ray & extreme UltraViolet (Radiation)

Acknowledgments

The past five years at McGill University have been a whirlwind experience, from planet discussions with free lunch and travelling internationally to share my Ph.D. research, to working from home and virtually collaborating during a global pandemic. I would not have completed this arduous journey without the love, support, and help of many people around me. While I cannot thank everyone explicitly (and likely not to the extent they deserve), there are a few that require special thanks and acknowledgement in this final document of my Ph.D. studies.

First, I need to thank my supervisor, Nick Cowan. Your unwavering support and willingness to learn through your students has pushed me to better myself and excel in a research area that was mostly new to me when I began at McGill. Your continued interest and enthusiasm for the research carried out by MEChA group members — spanning the entire range of exoplanets — has constantly motivated me to complete research goals, and inspired me to present these exciting results in various academic settings. After hearing stories of nightmare graduate school experiences, I truly feel like I won the lottery in having such a great supervisor to support, assist, and guide me through this final degree. I am forever grateful to Nick for his mentorship and this experience, and am now ready to move on from my life as a student.

During my time in Nick Cowan's research group, multiple group members have come and gone, with most of us sharing an office at one time or another. I can't thank each of them individually, but they have all impacted my Ph.D. experience in a net positive way. To Taylor, Lisa, and Dylan, my original officemates and Ph.D. compatriots, I cannot thank you enough for welcoming me into your group and commiserating on the potential roadblocks and pitfalls of graduate school. To Mahesh, Jared, Giang, and Vignesh, to whom I was somehow the "senior" of the group, thank you for all the fun and interesting chats, science-related or not, throughout the past couple years. No matter where we end up in the world and our careers, academic or otherwise, I hope to stay in touch with the other MEChA exoplaneteers.

I also must thank all of my colleagues in the Trottier Space Institute (TSI) at McGill, the Trottier Institute for Research on Exoplanets (iREx) at Université de Montréal, and the Earth & Planetary Sciences department at McGill. The space and exoplanet community in Montreal is exhilirating and thriving, and I'm glad I was able to be a part of it, even if just for a few years. The events, seminars, and gatherings provided a sense of community that is unmatched, and I will miss the afternoon coffee breaks and discussions of all things astronomy. I would be remiss not to specifically mention the EPS administration, Kristy Thornton and Anne Kosowski, who were the backbone of the department. Their importance to my Ph.D. experience cannot be understated, as they were always the go-to resource for all things graduate school; they showed immense care to all students and faculty, instilling a strong sense of family in the EPS department, and presented welcoming, smiling faces whenever visiting in-person.

I am extremely appreciative of the various funding sources that have aided me during the past five years. These include the McGill University Richard H. Tomlinson Doctoral Fellowship and the Natural Sciences and Engineering Research Council of Canada (NSERC) Post-Graduate Scholarship-Doctoral (PGS D). Further, I am very thankful to both the McGill University Graduate Mobility Award (GMA) and the Centre for Research in Astrophysics of Quebec (CRAQ) International Internship Scholarship for funding my transformative three-month internship to the Freie Universität Berlin in Berlin, Germany. I am grateful to Lena Noack for welcoming me into her group for this brief stint, and to the international colleagues I met along the way.

My family has been there throughout my 13-year journey as a "professional student", supporting me every step of the way and providing a loving environment either back home in Milton or wherever we may be visiting one another. My dad has always been my sounding board, and although he may have not liked the idea of such a long post-secondary career, I'm truly grateful for his love, respect, wisdom, and advice. He encouraged me to move to Montreal — a big move from Ontario — and helped with the details every step of the way. He has inspired me to become the (hopefully) well-rounded person I am today, and I would not be where I am today without his enduring support. I have to acknowledge my dad's partner, Kelly, as well; she has provided immense support throughout my graduate career, whether through attending my public talks (with no prior knowledge of the topic) or sending care packages with clothes and snacks.

My mom helped to shape the other big aspect of my personality: my love for all forms of media, whether TV shows, movies, or music. Without the comfort of consuming all media, I don't think I could have made it through school. It's hard to believe that my mom and I could talk about some obscure actor in an old TV show, and end up on a two-hour tangent about our favourite entertainment. I am glad I got to spend so much time with my mom growing up, and that we can continue to stay in touch in separate provinces, chatting on the phone about our current obsessions and reminiscing about shared memories. My sister, Shayla, is one of my best friends (even though I wasn't too thrilled when my "only child" status was rescinded). We have had similar interests and hobbies for as long as I can remember, and I love to chat about the newest superhero movie or strange, young adult TV show whenever

we get the chance. It is surreal to think about the people we are today, since it feels like only yesterday that we were playing with Barbies, Lego, and videogames in the basement playroom. Two paragraphs isn't enough to fully thank my family. I hope they know that I cherish them with all my heart, am extremely grateful for their support and sacrifice, and that they have shaped my life in ways that words cannot convey.

Last, but certainly not least, I have to express immense gratitude to my girlfriend, Julie. Ever since we met in an atmospheric radiation course, she has been my rock, with her unfaltering support and love forming one of the pillars of my motivation and drive to succeed. I would not have made it through the two years of isolation, nor the five years of my Ph.D., without her by my side, and nothing I can write will truly express my thanks for all of our shared experiences. Whether taking a spur-of-the-moment birthday trip to Vermont, having dinner at Le Boucan, or listening to the same conference talk for the umpteenth time, every moment has been special. *Je t'aime et je t'adore*; I love you so much, and now that I am (finally) done being a student, I am ecstatic for continued adventures and our next chapter together.

To everyone, including my childhood friends, high school friends, university friends, and family I did not mention by name, know that the person I am today, for better or worse, is thanks to the many enduring relationships I have forged during my time in Milton, Toronto, Berlin, and Montreal. In my M.Sc. thesis, I quoted Blink-182's "Dammit": *Well I guess this is growing up.* While that may have been true six(!) years ago, it rings true today as well. As I write the final words of my thesis, I am excited for what the future holds: its opportunities, challenges, and experiences are unknown, but the knowledge and skills gained during my graduate studies will be invaluable.

Contribution to Original Knowledge

The work presented within this Ph.D. dissertation contributed to the study and understanding of the habitability prospects of terrestrial planets orbiting M-dwarf host stars, using a coupled model incorporating geophysics, atmospheric science, and astronomy to predict surface water inventories as a first-order proxy for habitability.

Chapter 2, "Keeping M-Earths Habitable in the Face of Atmospheric Loss by Sequestering Water in the Mantle" (Moore & Cowan 2020), presents the results of our initial M-Earth model, one of the first to directly couple interior-atmosphere exchange through the deep-water cycle with the loss of water to space. We begin by reproducing the hybrid model of Komacek & Abbot (2016), and add parameterized loss to space to track planetary water inventories over time, since the long-lasting, high activity pre-main sequence phase of an M-dwarf can erode or completely remove the atmospheres of closely orbiting planets. The model presented — comparatively simple to the following model iterations — is essentially a "proof-of-concept" of the hypothesis that water hidden within a planetary interior, away from loss to space, can improve the habitability prospects of Earth-twin planets orbiting M-dwarf stars, which are expected to be very common in the Universe. We find that water sequestered in the planetary mantle can rehydrate a surface desiccated by water loss to space once loss decreases sufficiently. This result is critically dependent on coupling planetary interiors with their surfaces, atmospheres, and irradiation through evolution of the host star.

Chapter 3, "The Role of Magma Oceans in Maintaining Surface Water on Rocky Planets Orbiting M-Dwarfs" (Moore et al. 2023), presents an expanded and improved coupled model, now accounting for an early magma ocean stage due to the exceedingly high surface temperatures during the early lifetime of the planet, before surface solidification permits the plate-tectonics-driven deep-water cycle. We also test a second model incorporating a residual basal magma ocean, hypothesized to exist on rocky planets for Gyr timescales after surface solidification, to inject water into the solid mantle during deep-water cycling. Further, we use models of M-dwarf stars (Baraffe et al. 2015) to determine the planetary surface temperatures, calculate the rate of water loss to space, and calculate the orbital distances corresponding to the habitable zone. A magma ocean provides an additional reservoir, within which water is highly soluble and protected from loss to space; the timing of atmospheric degassing during the hot surface magma ocean period governs the amount of water lost in the energy-limited escape regime, which is shorter but more intense than diffusion-limited escape during deep-water cycling. We find that, although rocky planets around M-dwarf stars may be expected to lose up to 20 Earth oceans of water, many planets that form with less water than their expected loss survive our 5 Gyr simulations with sufficient surface water due to the nature of our coupled model, hiding water in the interior magma ocean and/or solid mantle. We also find that the lifetime of a basal magma ocean is critical, with a shorter lifetime being more beneficial to surface habitability. This paper hence further supports our coupled modelling approach and the potential to alleviate the problem of water loss to space through interior storage.

Finally, Chapter 4, "The Impact of Planetary Mass on the Surface Water Inventories of Terrestrial Planets Around M-Dwarfs", presents simulation results for various mass terrestrial planets, ranging from Earth-mass to super-Earths. This was mainly undertaken as the senior thesis project of Benjamin David and Albert Yian Zhang, while I advised on the project direction and discussed planetary-mass-dependent results with the students and my supervisor, Nicolas B. Cowan. Our results seem to support the habitability of lower-mass rocky planets undergoing plate tectonics over higher-mass ones, because more water becomes locked within the solid mantle with increasing planetary mass, and because a larger water inventory can lead to an uninhabitable, inundated surface. This means that a "waterworld" (i.e., no exposed continents), or a planet with a desiccated surface, may still have a hydrated mantle; while this enables plate tectonics to continue for a longer period, this hidden water is likely to remain trapped as the mantle cools over time and the rate of degassing from mantle to surface decreases. We also find that all else unchanged, if planets begin with the same water inventory, higher mass planets are more likely to become desiccated by water loss to space.

Overall, our coupled modelling approach presents robust results using 0-D box models to investigate the surface habitability of terrestrial planets orbiting M-dwarf stars. This thesis emphasizes the importance of water exchange and partitioning between interior, surface, and atmosphere when studying planetary habitability, and provides a comparison with recent and higher complexity models such as VPLanet (Barnes et al. 2020) and the coupled models of Krissansen-Totton et al. (2021a,b); Krissansen-Totton & Fortney (2022).

Contribution of Authors

The manuscript-based thesis presented here comprises three original works, for which I was the first author, completed under the supervision of Dr. Nicolas B. Cowan. Chapters 2 to 4 each present either a published or in-preparation manuscript tied together with bridging text written specifically for this dissertation to provide context and amalgamate these papers into a single cohesive narrative. Additionally, the Introduction and Discussion/Conclusion sections have not been published and are original to this work. I provide details of the authors' contributions below.

Paper 1, entitled "Keeping M-Earths Habitable in the Face of Atmospheric Loss by Sequestering Water in the Mantle", was published as Moore & Cowan (2020) in *Monthly Notices of the Royal Astronomical Society* with co-author Nicolas B. Cowan. I developed a modified deep-water cycling model based on code provided by Komacek & Abbot (2016), ran simulations of our new coupled model, analyzed the data, and wrote the majority of the manuscript. N.B.C. contributed ideas to the project, and provided critical feedback through discussion throughout the coding, writing, and editing processes.

Paper 2, "The Role of Magma Oceans in Maintaining Surface Water on Rocky Planets Orbiting M-Dwarfs", was published during the examination process of this thesis as Moore et al. (2023) in *Monthly Notices of the Royal Astronomical Society*. This paper was written with co-authors Nicolas B. Cowan and Charles-Édouard Boukaré. I implemented the atmospheric & geophysical improvements in the coupled model presented in Moore & Cowan (2020), and again ran the simulations, analyzed the data, and wrote the bulk of the manuscript. N.B.C. discussed ideas and provided critical feedback to the project — especially when suggestions of further model improvements than our initial ideas arose — and to the manuscript itself. C.-É.B. provided a simplified 0-D parameterization of magma ocean solidification and temporal water partitioning, and provided crucial insight from an academic background in geophysics as opposed to the astronomy backgrounds of myself and N.B.C.

Paper 3, "The Impact of Planetary Mass on the Surface Water Inventories of Terrestrial Planets", is an in-preparation manuscript with co-authors Benjamin David, Albert Yian Zhang, and Nicolas B. Cowan. I co-supervised with N.B.C. two undergraduate students — B.D. and A.Y.Z. — on their senior thesis project. I advised these students on modifying the coupled model to account for planetary mass, overseeing and checking their results throughout the academic year. I also wrote the manuscript, based on the simulation results of B.D. and A.Y.Z., although I contributed the final simulations, analysis, and created the figures presented within the paper. B.D. and

A.Y.Z collaborated closely, dividing the workload into digestible components. B.D. mainly focused on the theory of the project, exploring and investigating the concept of "super-Earths" for comparison with the Earth-mass coupled model used in Moore & Cowan (2020) and Moore et al. (2023). A.Y.Z. focused on the modification and improvement of the model itself, making it user-friendly. Both B.D. and A.Y.Z. ran simulations and analyzed the mass-dependent results. N.B.C. contributed ideas and helped guide the project, providing valuable feedback throughout the year and during the writing of the manuscript.

“You miss 100% of the shots you don’t take.
– Wayne Gretzky”
– Michael Scott, *The Office*, NBC, 2005–2013

“I hear the jury’s still out on science.”
– GOB Bluth, *Arrested Development*, Fox, 2003–2006

Chapter 1

Introduction

1.1 Exoplanets

For the majority of history, the only known planets were those within our own Solar System: four rocky planets, two gas giants, and two ice giants. Humans have been fascinated by these worlds outside the Earth, familiar yet distant. Science fiction writers, such as Arthur C. Clarke and Isaac Asimov, have long been enamored with the concept of extraterrestrial life existing elsewhere in our Solar System, or on planets speculated to orbit distant stars, some visible in the night sky. Today, scientists have discovered over 5500 planets outside of the Solar System.

The study of extra-solar planets — planets orbiting stars other than our Sun, and more commonly known as "exoplanets" — has risen to prominence since the first confirmed detection in 1992 (Wolszczan & Frail 1992) of a planet orbiting a pulsar. The first detection of a planet around a Sun-like star, 51 Pegasi b was published in

1995 (Mayor & Queloz 1995), a feat for which the authors later won a Nobel Prize. This detection presented evidence of a type of planet not present within the Solar System — a closely orbiting, inflated "hot Jupiter" — and began expanding our view of unfamiliar planetary systems.

As the field of exoplanets boomed and observational techniques improved, further novel discoveries were announced. Gliese 876 b was the first planet discovered around an M-dwarf star (Delfosse et al. 1998), colloquially known as "red dwarfs", while "super-Earth" GJ 1214 b was detected in 2009 orbiting an M-dwarf (Charbonneau et al. 2009), which may have a planet-wide ocean. Although detections continued to gradually increase the number of known exoplanets, a dedicated space telescope known as *Kepler* was launched by NASA in 2009 and an abundance of new discoveries followed, including its first rocky planet detection in 2011 (Batalha et al. 2011).

The past 10 year have reignited interest in and guided studies of exoplanets orbiting M-dwarf hosts. Two of the closest Earth-like planets that could potentially harbour life orbit M-dwarf stars: Proxima Centauri b (Anglada-Escudé et al. 2016) and Ross 128 b (Bonfils et al. 2018). The discovery of a compact multi-planet system in orbit around an M-dwarf in 2017 was amazing (Gillon et al. 2017): TRAPPIST-1 hosts seven rocky planets, three or four of which may host conditions suitable for life. Further planets have been discovered orbiting M-dwarf stars at distances amenable for extraterrestrial life including TOI-700d (Gilbert et al. 2020), the first Earth-sized exoplanet within the so-called "habitable zone" detected using the *Transiting Exoplanet Survey Satellite*, or *TESS*, a follow-up mission to *Kepler*. As we look to the future of exoplanet detection and characterization, it is important to perform theoretical studies of how exoplanets around M-dwarfs will evolve and change throughout their lifetimes, and how this could impact the origin and evolution of some form of life.

1.2 M-Dwarf Stars

Different types of stars can be distinguished by their distinct spectral features, giving rise to a stellar classification system. Our Sun is a G-dwarf star, specifically G2V: this means that its effective temperature is ∼5800 K, and the "V" refers to its existence on the "main sequence", the long-lived, relatively steady period of ongoing nuclear fusion where hydrogen is fused to helium within the core. G-type stars may have masses ranging from 0.9–1.06 $M_\odot$, where 1 $M_\odot = 1.99 \times 10^{30}$ kg is the mass of the Sun (Pecaut & Mamajek 2013). The bolometric luminosity of G-dwarf stars, i.e., their energy output integrated across all wavelengths of the electromagnetic spectrum, can range from 0.55–1.35 $L_\odot$(Pecaut & Mamajek 2013) , where 1 $L_\odot = 3.83 \times 10^{26}$ W is the luminosity of the Sun.

M-dwarf stars, on the other hand, are much smaller and much less luminous than G-dwarf stars. M-dwarfs span a range of masses from 0.08 $M_\odot$ (the lower-limit for hydrogen fusion within a star) to ∼0.6 $M_\odot$, with luminosities ranging from 0.0003–0.069 $L_\odot$ (Pecaut & Mamajek 2013). Further, the time spent during formation before the star spins down and settles onto the main sequence — the extremely high stellar activity "pre-main sequence" phase — is expected to be prolonged compared to G-dwarfs: while the Sun took roughly 20 million years (20 Myr) to reach the main sequence, M-dwarfs may take 600 Myr–3 Gyr (Pass et al. 2022), with enhanced activity for up to 8 Gyr (West et al. 2006). Further, the main sequence lifetime (i.e., the long-lived, more quiescent period amenable to the development of life) of an M-dwarf star is expected to be trillions of years, compared to the shorter 10 billion year main sequence lifetime of the Sun. While a longer main sequence lifetime is likely beneficial to life, the extended pre-main sequence phase may cause catastrophic effects that preclude the origin of complex molecules and make a planet permanently uninhabitable through erosion of its atmosphere or desiccation of its surface oceans.

1.3 The Habitable Zone & Habitability

The concept of the "habitable zone" — the region around a star where life could arise and flourish on an orbiting planet — has existed since Huang (1959). Later authors extended the notion to define habitability with respect to the presence and persistence of liquid surface water (e.g., Hart 1978; Kasting 1988). Indeed, the concept of the habitable zone, and by extension habitability, is based on the requirements for life as we know it: organic life on Earth.

The liquid water habitable zone was popularized by Kasting et al. (1993), and its definition later improved by Kopparapu et al. (2013). The habitable zone is defined today as the range of orbital distances around a given host star where the stellar energy imparted on a planet with an Earth-like atmosphere is comparable to the energy received by Earth today, permitting liquid water to exist on the surface. This concept can inform whether a planet *might* be habitable based on its instellation, and whether habitable conditions could exist for periods amenable to the evolution of life.

Owing to their smaller size and lower luminosities, the habitable zone around an M-dwarf star is much closer than the habitable zone within the Solar System, as shown in Fig. 1.1. While this is highly beneficial for observations and follow-up of detections of M-dwarf planets, the high irradiation and abundant flares during the extended pre-main sequence phase may preclude the emergence of extraterrestrial life.

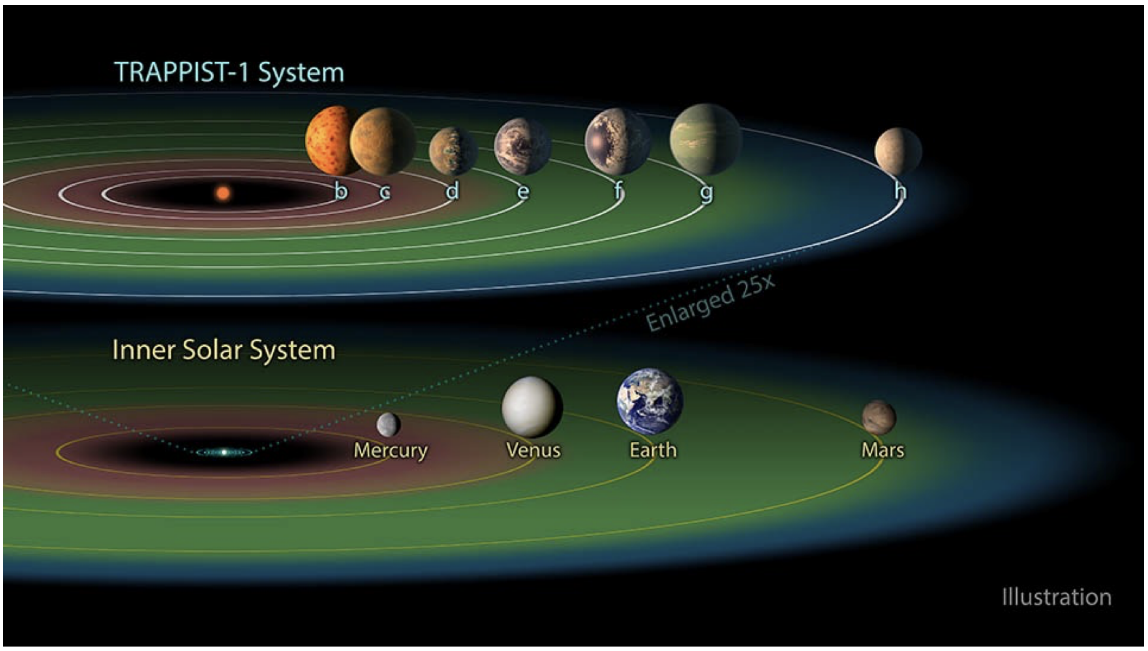

Figure 1.1: Comparison of circumstellar habitable zones around TRAPPIST-1, an ultracool M-dwarf star (top) and the Sun, a more massive and more luminous G-dwarf star (bottom). The habitable zone around TRAPPIST-1 is much closer than the habitable zone within the Solar System, so planets must orbit closer to receive the correct, "Goldilocks" amount of energy permitting liquid surface water. ©NASA Jet Propulsion Laboratory (https://www.jpl.nasa.gov/images/pia21424-the-trappist-1-habitable-zone)

Liquid surface water along with exposed continents on the Earth's surface regulates the climate on geological timescales, important for the origination and evolution of life (Walker et al. 1981; Kasting et al. 1993; Sleep & Zahnle 2001; Hakim et al. 2020). This climate regulation is provided through the carbonate-silicate cycle, as shown in Fig. 1.2. Rain, containing dissolved carbon dioxide, weathers the land of the continents, releasing carbonates and silicates to the ocean. Organisms within the oceans incorporate carbonates into their shells; when they die, they sink to the bottom, and these carbonate shells become sediment. Through plate tectonics (see Section 1.7), this sediment is subducted into the Earth, where the carbonates react with the silicates and create carbon dioxide, which is then released to the atmosphere. This carbon dioxide can then dissolve in rain, beginning the cycle again, and regulating the levels of atmospheric carbon dioxide and by extension surface climate since carbon dioxide is a strong greenhouse gas. Note that abiological carbonate deposition also occurs, and thus life is not a precursor nor a requirement for an operating carbonate-silicate cycle.

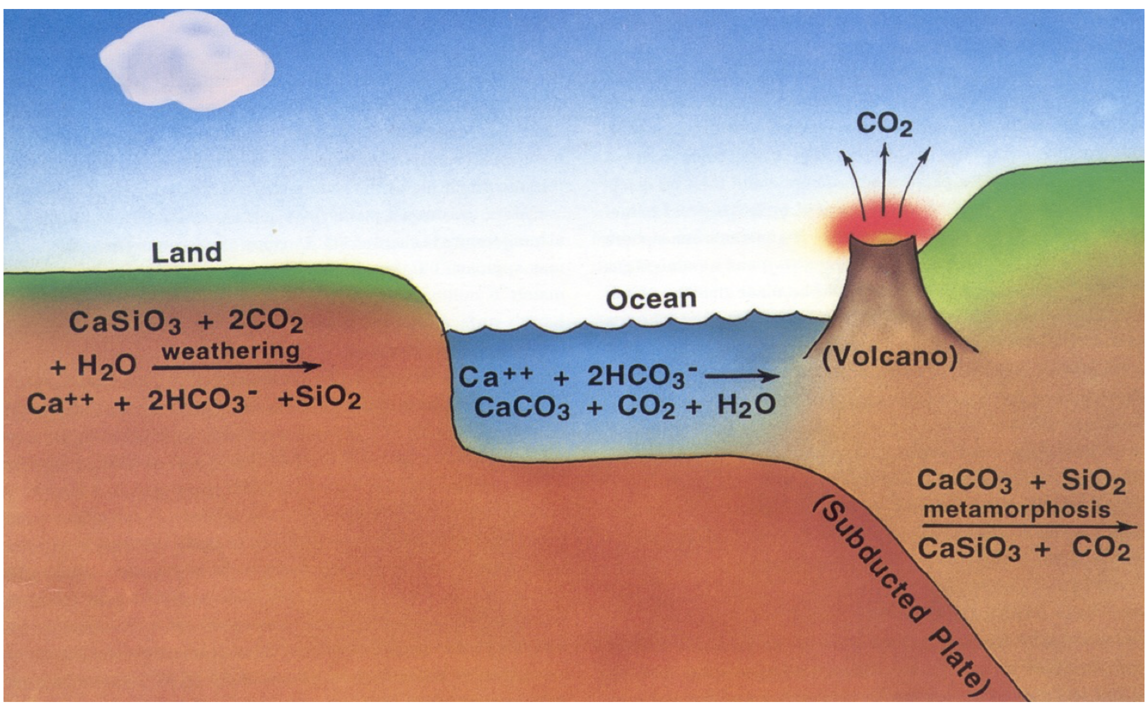

Figure 1.2: Illustration of the carbonate-silicate cycle on the Earth, which acts as a thermostat to maintain surface conditions ideal for life as we know it. ©J. Kasting (https://personal.ems.psu.edu/ jfk4/PersonalPage/ResInt2.htm)

1.4 The Runaway Greenhouse

As detailed in Section 1.2, stars begin in a very active state during the pre-main sequence phase, which can last for billions of years before settling onto the main sequence. The exceptionally high radiation from a star will then impinge on the atmospheres of orbiting planets, especially those on close orbits. When the amount of incoming irradiation cannot be compensated by the outgoing flux from the planet, surface temperatures rapidly increase and the planet enters a "runaway greenhouse" (Ingersoll 1969; Kasting 1988; Nakajima et al. 1992). During this period, any surface oceans will completely evaporate, forming a thick steam atmosphere which insulates and maintains the exceedingly high surface temperatures. Boukrouche et al. (2021) find that the inflection point for a runaway greenhouse atmosphere is never below the solidus of the surface for any rock type. Dorn & Lichtenberg (2021) also note that a solid rock surface existing below a thick steam atmosphere is "physically implausible" due to the extremely high surface temperatures.

The runaway greenhouse is especially concerning for planetary habitability, as it is governed by hot, uninhabitable surface temperatures. Moreover, because water is available throughout the upper atmosphere, it is readily available to escape to space, lost from the planet. As shown in Fig. 1.3, following their formation, planets orbiting M-dwarfs are in a runaway greenhouse phase for longer periods compared to planets around G-dwarfs. Indeed, this is a negative for persistent liquid surface water, a first-order proxy for habitability, and must be considered when assessing a planet's habitability throughout its evolution.

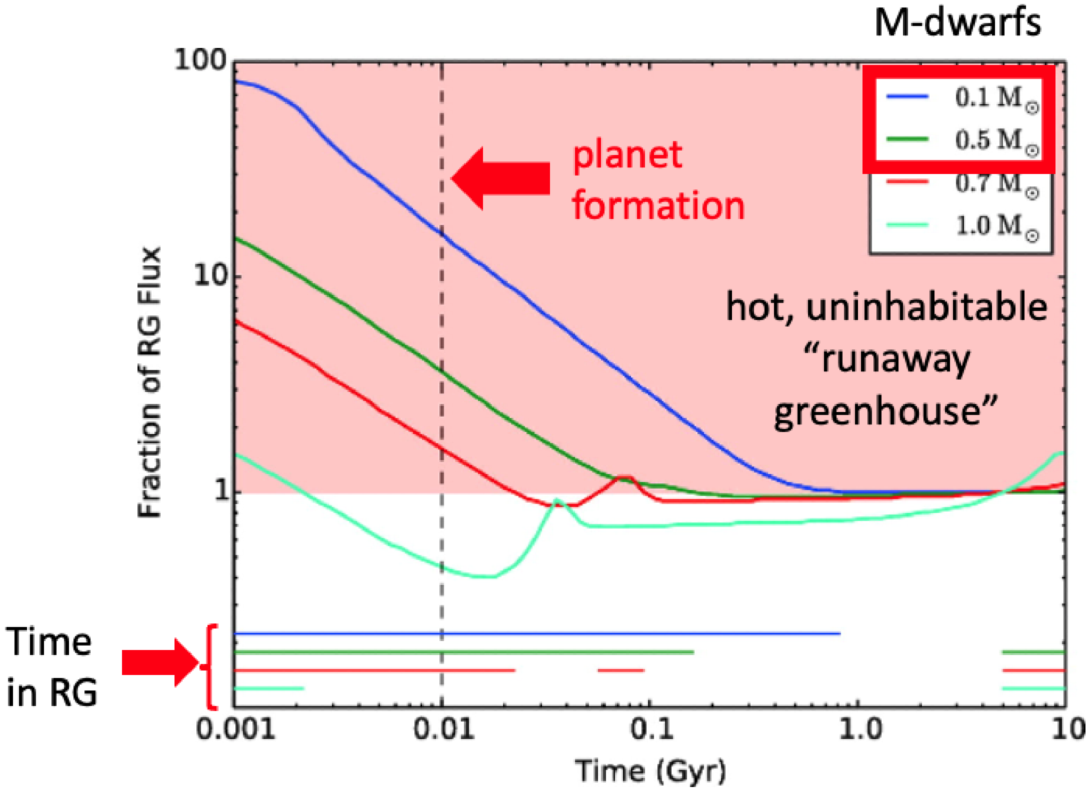

Figure 1.3: Time, in Gyrs, during which a planet is experiencing a runaway greenhouse following its formation. The red curve corresponds to a larger K-dwarf host, while the cyan curve is for an even larger G-dwarf host (like the Sun). Planets around the smallest stars, the two highlighted M-dwarfs, are in a runaway greenhouse for extended periods following their formation, during which their hot temperatures cause all water to evaporate into a steam atmosphere, from which water is readily available to be lost to space. Modified from Luger & Barnes (2015); ©Mary Ann Liebert, Inc.

1.5 Magma Oceans

Immediately following terrestrial planetary formation, energy from accretion and core formation can lead to a “magma ocean”: a potentially global silicate melt, which may extend from surface to core (e.g., Wood et al. 1970; Solomon 1979; Wetherill 1990; Elkins-Tanton 2008). Indeed, owing to the high temperatures associated with the runaway greenhouse, it is likely that magma ocean and runaway greenhouse phases are concurrent. The magma ocean will solidify from the bottom–up, gradually sequestering some water into the solid mantle governed by a solid-melt partition coefficient, while the majority remains dissolved in the magma ocean. Throughout this period, the partial pressure of atmospheric water is set through equilibrium with the molten surface (e.g., Elkins-Tanton 2008). The magma ocean could hence protect against the escape of water to space during the hot temperatures associated with the runaway greenhouse, but will also govern the partitioning of water between interior and atmosphere once the magma ocean solidifies.

Earth, too, began in a magma ocean phase, which likely lasted between 1.5 Myr (Lebrun et al. 2013) and 5 Myr (Hirschmann 2006). With no atmosphere, Earth’s magma ocean would have rapidly cooled in only 4000 yr (Lebrun et al. 2013). However, due to the extended runaway greenhouse phase around M-dwarf stars, the magma ocean phase on terrestrial planets may be prolonged to 100s of Myrs or Gyrs. Further, if a magma ocean were to solidify from the middle–out instead of the bottom–up, an isolated “basal magma ocean” could form below the solid mantle (Labrosse et al. 2007), providing an additional reservoir for water long after the surface has solidified. Hence, magma oceans can protect water from being lost to space through dissolution, and this water may then be rapidly or gradually released to the surface and atmosphere.

1.6 Atmospheric Loss

Planetary atmospheres may be eroded or stripped through various thermal and non-thermal mechanisms (Pierrehumbert 2010; Taylor 2010; Sanchez-Lavega 2011; Gronoff et al. 2020). The simplest form, thermal or Jeans escape to space, is essentially a "boiling off" of the upper atmosphere, and occurs when a molecule's thermal velocity exceeds the planet's escape velocity. However, thermal escape is slow and only relevant to the lightest atmospheric constituents. Non-thermal mechanisms are more numerous. Examples include hydrodynamic escape, which is fueled by the absorption of ultraviolet photons high in the atmosphere and the energy diffused to lower levels, and involves a sustained, bulk outflow of a lighter species to space that can become powerful enough to drag heavier species that would not otherwise escape (e.g., a strong hydrogen outflow dragging oxygen with it). Stellar wind erosion occurs when high energy protons from the host star deliver enough energy to atmospheric constituents to drive their escape, and its effect will be more prevalent for planets without a magnetic field. Through impact erosion, as its name suggests, different sized impactors can remove proportional amounts, or even the entirety of, the atmosphere; this was an important process during the early Solar System.

The rate of atmospheric escape will naturally evolve over time as both the space and planetary environments evolve, and the irradiation will vary depending on the stellar type of the host star. Importantly, this means that planets orbiting closer to younger, more active stars will be more susceptible to have their atmosphere eroded or completely removed. Indeed, atmospheric escape from rocky planets orbiting M-dwarf stars has been extensively studied (e.g., Wordsworth & Pierrehumbert 2013, 2014; Luger & Barnes 2015; Bolmont et al. 2017a; France et al. 2020; Krissansen-Totton & Fortney 2022), Specifically, many studies have focused on the XUV irradiation impinging on the atmospheres of orbiting planets, which can photodissociate water molecules — critical in determining a planet's habitability — high in the atmosphere and drive their loss to space, and constraint of XUV output from particular M-dwarf hosts is of ongoing interest (e.g., Fleming et al. 2020; King & Wheatley 2021). Further, many of these calculated water escape rates presume extensive water readily available in the atmosphere while neglecting its exchange with, and potential isolation within, the planetary interior.

1.7 Plate Tectonics & Earth's Deep-Water Cycle

Earth is the only confirmed planet that experiences plate tectonics (Fig. 1.4). This planet-wide process has transformed the Earth's surface throughout its history, reshaping and rearranging continents, and allowing exchange of materials between surface and interior on geological timescales (see, e.g., Langmuir & Broecker 2012). Water vapour is present within the Earth's atmosphere, and liquid oceans persist on Earth's surface covering about 70% of the surface; however, the Earth's mantle also holds water in nominally anhydrous minerals in the form of protons and OH^- ions (e.g., Hirschmann 2006; Hirschmann & Kohlstedt 2012; Korenaga et al. 2017). This dissolved water depresses the mantle viscosity sufficiently to allow it to readily flow on geological timescales, one of the requirements for plate tectonics along with relatively cool surface temperatures. The amount of water in the Earth's mantle is an ongoing debate, with estimates ranging from $\sim$0.1–10 Earth Oceans (Hauri et al. 2006; Hirschmann 2006; Hirschmann & Kohlstedt 2012; Pearson et al. 2014; Guimond et al. 2023).

The exchange of water between surface and interior, governed by plate tectonics, is known as Earth's deep-water cycle (Hirschmann 2006; Langmuir & Broecker 2012; Korenaga et al. 2017), and explains the steady-state "freeboard" of Earth, i.e., the level of the oceans with respect to the contents, over geological time (Hynes 2001). Water is degassed from mantle to surface through mid-ocean ridge volcanism; these mid-ocean ridges, visible in Fig. 1.4, are also spreading centres where new crust is created. This crust is then transported away from the mid-ocean ridges, towards subduction zones (in Fig. 1.4, the subduction zone is at a contintental margin), during which the crust is hydrothermally altered and gradually incorporates water into its structure. The hydrated crust is then subducted below the adjacent plate, and while much of the water will remain in volcanic gases erupted by convergent margin volcanoes (Gaillard & Scaillet 2014), some water will be regassed from the surface back into the mantle, where the deep-water cycle can begin again. Indeed, it is this unique geophysical aspect of the Earth that could hide and protect water on rocky planets orbiting highly active M-dwarf stars from extensive loss to space. The importance of coupling tectonic mode, surface climate, and planetary interior to determine habitability has been explored and emphasized in the literature (e.g., Foley 2015; Foley & Driscoll 2016), and within this thesis, we seek to further explore this concept through coupling geophysics with water loss to space for rocky worlds around M-dwarf hosts.

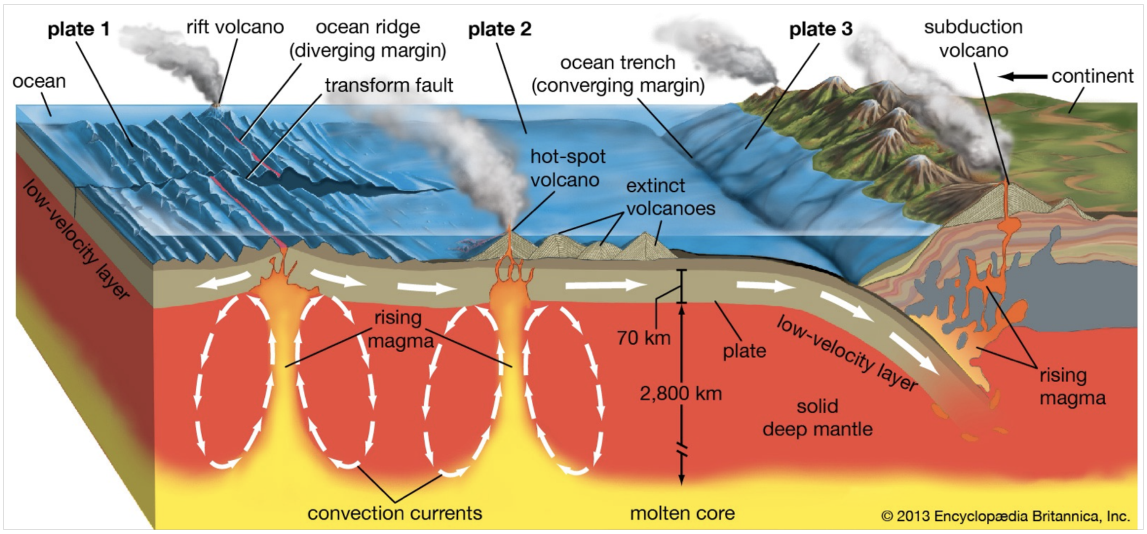

Figure 1.4: Plate tectonics on the Earth, which governs the exchange of water between atmosphere, surface, and interior through the deep-water cycle. Water dissolved within the mantle allows it to readily flow, a requirement for plate tectonics. ©Encyclopedia Britannica, Inc. (https://kids.britannica.com/students/article/plate-tectonics/276460)

1.8 M-Dwarf Planets & Their Habitability

Rocky planets orbiting M-dwarf stars are expected to be the most abundant potentially habitable planets in the Universe (Dressing & Charbonneau 2015; Sabotta et al. 2021). The contrast ratio with their host star, along with their short orbits (see Fig. 1.5), have made rocky M-dwarf planets prime targets for observation and characterization (through transmission spectroscopy) for many years. Indeed, the "M-dwarf opportunity" (Charbonneau & Deming 2007) refers to the fact that M-dwarf planets are likely the only planets we can characterize until next-generation, extra-large telescopes and dedicated space missions are in operation.

Why, aside from the aforementioned reasons, should we target M-dwarfs? (For an extensive review, see, e.g., Shields et al. 2016.) Around 70% of the stars in our Galaxy are M-dwarfs (Henry 2004), and multiple planet M-dwarf systems are common; M-dwarfs host nearly 3.5 times more small planets than around FGK stars (i.e., the three larger classes of "dwarf stars"; while M-dwarfs are commonly known as "red dwarfs", FGK-dwarfs range from white to orange), with roughly 1/3 orbiting within the habitable zone (Shields et al. 2016). The very long lifetime of M-dwarfs — trillions of years, thousands of times longer than our Sun — provides more time for life to originate and develop. Since M-dwarf planets orbit closer, transits are deeper (as shown in Fig. 1.5) and more frequent, and the radial velocity (i.e., variations in stellar velocity due to the gravitational pull of an unseen companion) will be higher. Unfortunately, because of the smaller size of M-dwarfs, the habitable zone is much closer (see Fig. 1.1). This is even more troublesome because of the extended pre-main sequence phase, intense flaring, and very high irradiation across the electromagnetic spectrum compared to FGK stars; in particular, the combination of X-ray and extreme ultraviolet (XUV) radiation is detrimental to planets' habitability, as it can erode or remove the atmosphere, potentially desiccating the surface in the process.

The most well-known M-dwarf planetary system is probably TRAPPIST-1 (Gillon et al. 2017), an ultracool M-dwarf harbouring seven closely-orbiting rocky planets, although our nearest neighbour Proxima Centauri b (Anglada-Escudé et al. 2016) also orbits an M-dwarf. Because of the problematic environment these planets face, we are uncertain whether these planets will have thick atmospheres, thin atmospheres, or be stripped bare rocks. The James Webb Space Telescope should begin to answer this question; indeed, recent observations have determined that TRAPPIST-1b — the closest planet — likely had no atmosphere (Greene et al. 2023). The research presented within this thesis is complementary to this and upcoming results, exploring theoretically whether rocky M-dwarf planets have atmospheres and, importantly, surface water using predictive, coupled models.

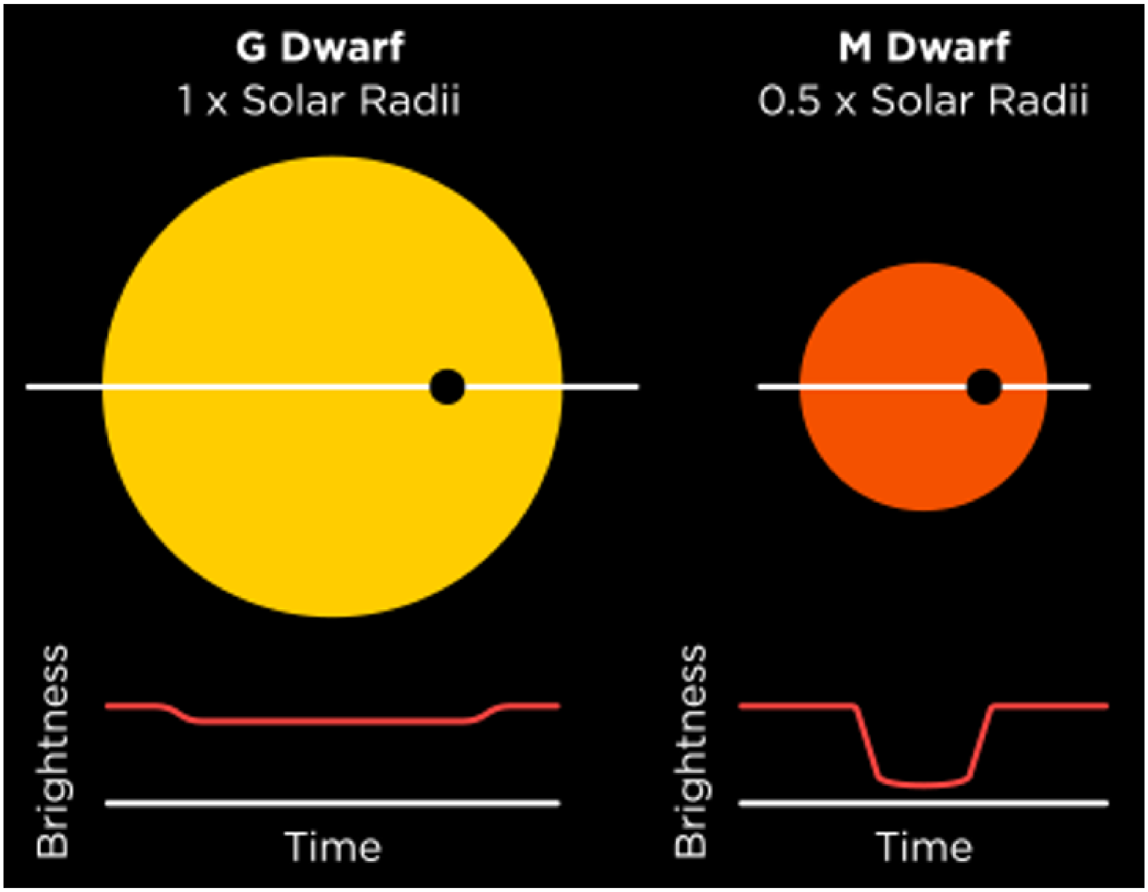

Figure 1.5: Comparison of a transit observation for a Sun-like, G-dwarf star (left) and a smaller, less luminous M-dwarf (right). For the same sized planet, the transit around an M-dwarf is shorter and significantly more pronounced, ideal for observation and characterization. ©University of Nebraska-Lincoln (https://astro.unl.edu/newRTs/Transits/background/Transit1.html)

1.9 A Brief History of Box Models

Box models, although zero-dimensional (i.e., each "box" has one representative, average value for a given variable) can provide immense insight into the inner workings and underlying physical processes of more complex, higher-dimensional models by distilling model components into simple, digestible modules. Indeed, due to uncertainties related to high-pressure, interior geophysics and compositional effects, box models have long been a favoured first step for representing the evolution of Earth and other rocky exoplanets. For example, box models have been used to study the exchange of water between surface and mantle reservoirs — i.e., the deep-water cycle — through parameterization of processes such as mid-ocean ridge volcanism and subduction.

One of the earliest instances of a volatile cycling box model, which included thermal evolution, was that of McGovern & Schubert (1989), incorporating water-dependent mantle viscosity along water cycling through degassing and regassing. This model has inspired studies of the Earth (e.g., Kasting & Holm 1992; Williams & Pan 1992; Franck & Bounama 1997; Korenaga 2011) and exoplanets (e.g., Franck & Bounama 1995; van Thienen et al. 2007; Sandu et al. 2011; Cowan & Abbot 2014; Schaefer & Sasselov 2015; Komacek & Abbot 2016). Two of these exoplanet models, those of Cowan & Abbot (2014) and Schaefer & Sasselov (2015), were combined to create the "hybrid model" of Komacek & Abbot (2016) which served as the basis for the box models presented throughout this thesis. It is important to note that using box models to study M-dwarf planet habitability is predictive; however, in the near-future, these models will become interpretative.

1.10 Research Questions

With the above background in mind, we can now state the research questions of this thesis. We want to use predictive models, coupling geophysical processes of planetary interior and surface with the atmosphere and atmospheric loss to space, to determine whether rocky, terrestrial planets orbiting M-dwarf stars are likely to have persistent surface water, a first-order proxy for habitable surface conditions. Since rocky planets orbiting M-dwarfs are common, and present missions such as the James Webb Space Telescope are beginning to characterize rocky worlds around M-dwarf hosts, with upcoming missions pushing observational capabilities even farther, the question of whether or not these planets are amenable to the origin and evolution of life is, and will continue to be, a pressing matter in the near future.

Throughout the chapters of this thesis, we will explore the question of the surface water inventories of rocky planets orbiting M-dwarf stars using models of increasing complexity. Chapter 2 presents a proof-of-concept model, coupling the deep-water cycling model of Komacek & Abbot (2016) with parameterized loss to space based on the analysis of Luger & Barnes (2015). Chapter 3 then presents a model with improved atmospheric loss — accounting for the M-dwarf host evolution using the models of Baraffe et al. (2015) — and improved geophysics: the planet begins with a molten surface, in a magma ocean phase during runaway greenhouse, before initiating solid-surface plate tectonics and deep-water cycling. Next, Chapter 4 modifies the previous model to investigate the impact of planetary mass on the evolution of surface water inventory and planet-wide water partitioning, exploring Earth-size planets to super-Earths. Finally, in Chapter 5, we will discuss the results and consequences of all three studies in the context of M-dwarf rocky planet habitability.

Chapter 2

Keeping M-Earths Habitable in the Face of Atmospheric Loss by Sequestering Water in the Mantle

This thesis chapter originally appeared in the literature as
Moore & Cowan 2020, *Monthly Notices of the Royal Astronomical Society (MNRAS), 496, 3786. https://doi.org/10.1093/mnras/staa1796*

Authors

Keavin Moore [1,2], Nicolas B. Cowan [1,2,3]

[1]Department of Earth & Planetary Sciences, McGill University, 3450 rue University, Montréal, QC H3A 0E8, Canada

[2]McGill Space Institute, McGill University, 3550 rue University, Montréal, QC H3A 2A7, Canada

[3]Department of Physics, McGill University, 3600 rue University, Montréal, QC H3A 2T8, Canada

Preface

For a planet to be considered "habitable", it requires persistent liquid surface water, an appropriate environment in which organic molecules can form, and an energy source. To first-order, however, we wanted to explore the persistence of liquid surface water, which will strongly depend on the space environment and host star of a rocky planet. Previous studies had either used parameterized box models to investigate water exchange between interior and surface (Cowan & Abbot 2014; Schaefer & Sasselov 2015; Komacek & Abbot 2016), or focused solely on the loss of water to space (e.g., Wordsworth & Pierrehumbert 2013, 2014; Luger & Barnes 2015; Bolmont et al. 2017a). The cycling of water between interior and surface means there can be substantial water sequestered in the mantle while the surface is rapidly losing water to space and potentially becoming desiccated. However, we posited that if this interior water is degassed to the surface — especially once the host M-dwarf settles and loss rates decrease — liquid surface water may be maintained or even increased.

Inspired by these studies, we created a coupled box model of deep-water cycling and water loss to space for Earth-mass planets orbiting M-dwarf stars, since rocky planets around M-dwarf hosts are expected to be abundant. While we also initially explored the impact of water loss on the seafloor-pressure-dependent model of Cowan & Abbot (2014) and the mantle-temperature-dependent model of Schaefer & Sasselov (2015), we chose to focus on the hybrid model of Komacek & Abbot (2016) combining the previous two. Although the code was provided by T. Komacek, I re-coded the model to better understand its inner workings, fix any bugs, and better implement the parameterized water loss. Within this first model iteration, our parameterization for water loss is simple: a decreasing exponential that removes water directly from the surface reservoir, based on the decreasing exponential XUV luminosity of the host M-dwarf.

This chapter presents the results of our first simulations, in which we explore the question: can water stored in a planetary mantle maintain or recover habitable surface conditions in the presence of potentially intense water loss to space? The simulation results provide strong evidence that interior water can be beneficial to surface habitability, and the rather simple model acts as a "proof-of-concept" model for coupled water cycling and loss to space, which I will improve in the following papers.

Abstract

Water cycling between Earth's mantle and surface has previously been modelled and extrapolated to rocky exoplanets, but these studies neglected the host star. M-dwarf stars are more common than Sun-like stars and at least as likely to host temperate rocky planets (M-Earths). However, M dwarfs are active throughout their lifetimes; specifically, X-ray and extreme ultraviolet (XUV) radiation during their early evolution can cause rapid atmospheric loss on orbiting planets. The increased bolometric flux reaching M-Earths leads to warmer, moister upper atmospheres, while XUV radiation can photodissociate water molecules and drive hydrogen and oxygen escape to space. Here, we present a coupled model of deep-water cycling and water loss to space on M-Earths to explore whether these planets can remain habitable despite their volatile evolution. We use a cycling parameterization accounting for the dependence of mantle degassing on seafloor pressure, the dependence of regassing on mantle temperature, and the effect of water on mantle viscosity and thermal evolution. We assume the M dwarf's XUV radiation decreases exponentially with time, and energy-limited water loss with 30% efficiency. We explore the effects of cycling and loss to space on planetary water inventories and water partitioning. Planet surfaces desiccated by loss can be rehydrated, provided there is sufficient water sequestered in the mantle to degas once loss rates diminish at later times. For a given water loss rate, the key parameter is the mantle overturn timescale at early times: if the mantle overturn timescale is longer than the loss timescale, then the planet is likely to keep some of its water.

2.1 Introduction

Habitability critically depends on the presence of liquid water on the surface of a planet. Earth is the only planet in the Universe with confirmed surface oceans and life as we know it, and as such, it is our template for a habitable planet (Langmuir & Broecker 2012). The habitable zone (HZ) around a star is usually defined by the stellar flux at a given orbital distance, which influences the surface temperature (Kasting et al. 1993) — planets at the hot inner edge vaporize their oceans, while the oceans of a planet at the cold outer edge will freeze. Water is not only important for biological processes; it also influences planetary climate through the silicate weathering thermostat (Walker et al. 1981; Sleep & Zahnle 2001; Abbot et al. 2012; Alibert 2014).

It must be noted that the presence of liquid surface water may constitute habitability in the classical definition (Kasting et al. 1993), but this does not necessarily mean the planet is hospitable and conducive to the origin of life. Rather, liquid surface water is a first step towards life as we know it, and our results only support the presence of liquid surface water and thus the classical definition of habitability. Recent studies find that the orbital environment around M dwarfs may lack the necessary levels of UV radiation to form RNA monomers, which are critical to the development of Earth-like biology (Ranjan et al. 2017; Rimmer et al. 2018); however, the scarcity of UV may be overcome by transient flaring events. We must be careful in assuming liquid surface water means life due to the multitude of factors that allowed life to originate on the early Earth.

2.1.1 Water Cycling

It is speculated that there is at least as much water sequestered in the mantle as is present on the surface of Earth (Hirschmann 2006). Current estimates based on experimental data put the water capacity of Earth's mantle at 12 terrestrial oceans (TO, where 1 TO $\approx 1.4 \times 10^{21}$ kg; Hauri et al. 2006; Cowan & Abbot 2014).

Water is exchanged between the surface and mantle reservoirs of Earth on geological timescales. This water cycle is mediated by plate tectonics, which depend not only on the cool, brittle lithospheric plates, but also on the viscous, flowing mantle (see, e.g., Hirschmann 2006; Langmuir & Broecker 2012). Water dissolved in the mantle decreases its viscosity and allows it to flow more readily, a requirement for plate tectonics (Hauri et al. 2006). As plates separate from one another at mid-ocean ridges, the mantle below ascends to fill the gap and melts due to depressurization, and volatiles are released into the ocean by degassing as the new ocean crust solidifies. The ocean crust then spreads away towards subduction zones, and its minerals become hydrated due to hydrothermal interactions with seawater. This volatile-rich slab is then subducted back into the mantle. While most of the volatiles will contribute to water-rich magmas at convergent margin volcanoes, some water will continue into the deep mantle, regassing water into the interior.

2.1.2 Water Loss to Space

Roughly 70% of stars in the Galaxy are M dwarfs (Henry 2004), and about 30% are host to at least one rocky exoplanet in the HZ (Dressing & Charbonneau 2015). We should then expect that 90-99% of temperate terrestrial planets orbit an M dwarf instead of a Sun-like star; henceforth, we call such planets M-Earths.

M dwarfs are more active than Sun-like stars (Scalo et al. 2007), specifically in the X-ray and extreme ultraviolet, collectively known as XUV. An M dwarf emits more XUV radiation during the first billion years of its lifetime, as the star evolves onto the main sequence. Young planets orbiting within the HZ may lose multiple oceans of water to space as they are bombarded by XUV radiation. Water molecules are photodissociated high in the planetary atmosphere (Wordsworth & Pierrehumbert 2013, 2014; Luger & Barnes 2015; Bolmont et al. 2017b; Schaefer et al. 2016; Wordsworth et al. 2018; Fleming et al. 2020); the lighter hydrogen is lost to space, while the heavier oxygen remains behind, either reacting with the surface or accumulating in the atmosphere and creating a biosignature false positive (see, e.g., Wordsworth & Pierrehumbert 2013, 2014; Wordsworth et al. 2018). Some oxygen may also hydrodynamically escape, dragged to space by the escaping hydrogen (e.g., Hamano et al. 2013; Luger & Barnes 2015). Studies also indicate that factors of 5–10 more XUV irradiation than modern-day Earth can lead to runaway atmospheric loss (Tian et al. 2008), and that several Gyr-old planet-hosting M dwarfs may output 5–100 times more XUV radiation than the Sun today (e.g., Ribas et al. 2016, 2017; Youngblood et al. 2016). Moreover, it has recently been indicated that M dwarfs remain more active in the extreme-UV (EUV) for a given age than solar-type stars (see, e.g., Fig. 6 of France et al. 2018).

We hypothesize that a planet whose surface becomes desiccated by loss of water to space can recover an ocean through the degassing of water sequestered in the mantle. This will depend on the initial amount of water partitioned between the surface and mantle, the mantle overturn timescale, and the XUV-driven water loss rate and timescale. While the deep-water cycle and atmospheric loss have been separately modelled in previous work, we seek to couple these two phenomena, combining aspects of geophysics, astronomy, and space physics.

The paper continues as follows. We describe the cycling and loss equations of our model in Section 2.2, present our cycling results for various initial water inventories and loss rates in Section 2.3, and discuss the results of our study in Section 2.4.

2.2 Water Cycling & Loss Model

2.2.1 Previous Work

The deep-water cycle of Earth has previously been represented using two-box models. These models account for regassing of water from surface to mantle through subduction of hydrated basaltic oceanic crust, and degassing from mantle to surface by mid-ocean ridge volcanism. McGovern & Schubert (1989) incorporated reduction of mantle viscosity through the addition of regassed water, while parameterizing degassing and regassing rates as dependent on the amount of volatiles present in the mantle and basaltic oceanic crust, respectively, along with mid-ocean ridge spreading rate and subduction efficiency.

The mantle-temperature-dependent model of Schaefer & Sasselov (2015), based on the model of Sandu et al. (2011), also included mantle viscosity and two convection regimes: single layer and boundary layer. Komacek & Abbot (2016) simplified the mantle-temperature-dependent model of Schaefer & Sasselov (2015), and replaced the degassing rate with the seafloor-pressure-dependent degassing parameterization of Cowan & Abbot (2014) to create a hybrid model.

There are various water loss rates throughout the literature; for example, Wordsworth & Pierrehumbert (2014) note that an N_2-poor planet could lose up to 0.07 TO/Gyr, while loss rates from Luger & Barnes (2015) range from 0.02 TO/Gyr to about 2 TO/Gyr, depending on initial water inventory and orbital distance within the HZ.

2.2.2 Cycling & Loss Equations

We use the time-dependent hybrid cycling model of Komacek & Abbot (2016) and parameterize the water loss of Luger & Barnes (2015) to represent the cycling and loss to space of water on an M-Earth. Our model accounts for the fact that hydration depth of ocean crust is likely affected by mantle temperature, T, more than seafloor pressure, P, and that degassing would shut off at late times when the mantle is cool. Meanwhile, it has been shown that degassing should be P-dependent (Kite et al. 2009). Our two-box + sink model is shown schematically in Fig. 2.1, including surface and mantle reservoirs, exchange between the two, and water loss to space directly from the surface reservoir, for simplicity.

Any changes or additions to the relevant thermal evolution and cycling equations from Komacek & Abbot (2016) are described here and in Appendices 2.5.1 and 2.5.2. The thermal evolution and cycling equations were non-dimensionalized by Komacek & Abbot (2016) to emphasize the physical processes over the control variables themselves. While we use the non-dimensionalized code for our simulations, we present the dimensionful equations here. Appendix 2.5.3 contains a cheat sheet of all the model variables and parameters.

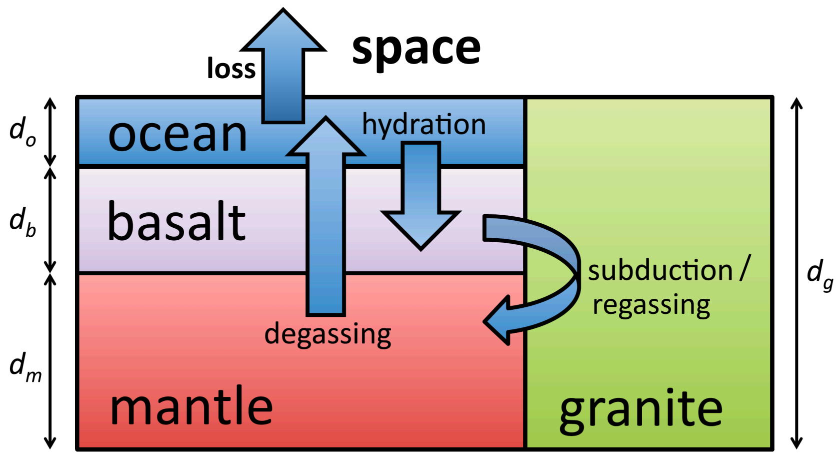

Figure 2.1: Two-box model of water cycling between surface and mantle reservoirs on Earth, adapted from Cowan & Abbot (2014) to include water loss to space (bolded). Water is degassed from the mantle to the surface through mid-ocean ridge volcanism, and regassed from the surface to the mantle through subduction of hydrated basaltic oceanic crust. Water is lost to space directly from the surface reservoir for simplicity, and is driven by XUV radiation from the host M dwarf, which decreases exponentially with time (Luger & Barnes 2015). ©AAS. Reproduced with permission.

The model developed by Komacek & Abbot (2016) incorporates P-dependent degassing (Cowan & Abbot 2014) and T-dependent regassing (Schaefer & Sasselov 2015). The authors note that this hybrid model may be the most realistic deep-water cycling model of their study; for this reason, we use it as our representative water cycling parameterization.

We restore the piecewise degassing limit of Cowan & Abbot (2014); while this makes the equation harder to manipulate analytically, it ensures that a parcel of mantle cannot degas more water than it contains. The change in mantle water mass

W_m with time t is,

$$\frac{dW_\mathrm{m}}{dt} = L_\mathrm{MOR}S(T)\Bigg[x_\mathrm{h}\rho_\mathrm{c}\chi_\mathrm{r}d_\mathrm{h}(T) \\ - x\rho_\mathrm{m}d_\mathrm{melt}\min\left[f_{\mathrm{degas},\oplus}\left(\frac{P}{P_\oplus}\right)^{-1},\ 1\right]\Bigg], \tag{2.1}$$

where the first term on the right-hand side is the regassing rate, $w_\downarrow$, and the second is the degassing rate, $w_\uparrow$. The other variables are as follows: $L_\mathrm{MOR} = 3\pi R_\mathrm{p}$ is the mid-ocean ridge length (with R_p the planetary radius), and $S(T)$ is the T-dependent spreading rate. The mass fraction of water in the hydrated crust is x_h, ρ_c is the density of the crust, χ_r is the subduction efficiency, and the hydrated layer depth is a function of mantle temperature, $d_\mathrm{h}(T)$. The mantle water mass fraction is x. The density of the upper mantle is ρ_m, d_melt is the mid-ocean ridge melting depth, $f_{\mathrm{degas},\oplus} = 0.9$ is the nominal value of melt degassing for present-day Earth, P is the seafloor pressure, and $P_\oplus$ is the seafloor pressure of Earth. The pressure dependence is defined as a power law, using the nominal value from Cowan & Abbot (2014) for the exponent.

The equivalent cycling equation for the surface water mass W_s is,

$$\frac{dW_\mathrm{s}}{dt} = L_\mathrm{MOR}S(T)\Bigg[x\rho_\mathrm{m}d_\mathrm{melt}\min\left[f_{\mathrm{degas},\oplus}\left(\frac{P}{P_\oplus}\right)^{-1},\ 1\right] \\ - x_\mathrm{h}\rho_\mathrm{c}\chi_\mathrm{r}d_\mathrm{h}(T)\Bigg] - \min\left[\phi_\mathrm{loss}\exp\left(\frac{-t}{\tau_\mathrm{loss}}\right),\ \frac{W_\mathrm{s}}{\tau_\mathrm{step}}\right]. \tag{2.2}$$

Here, the first term on the right-hand side is now the degassing rate, $w_\uparrow$, and the second is the regassing rate, $w_\downarrow$. The third term on the right-hand side is the water loss rate, w_loss, a decreasing exponential based on the M dwarf XUV evolution with time in Fig. 1 of Luger & Barnes (2015), which utilizes the stellar models of Ribas et al. (2005); note that we assume the XUV radiation simply decreases exponentially from its initial value, with the loss of water to space linearly correlated to this evolution. Note also we do not directly model the stellar evolution, nor do we account for a planetary magnetic field; as a result, we do not include flare- or stellar-wind-driven loss in this study. Recent studies support stellar-wind-driven ion pick-up escape leading to rapid, complete atmospheric erosion for planets orbiting ‘old’ (i.e., several Gyr) M dwarfs like Proxima Centauri b (Airapetian et al. 2017; Garcia-Sage et al. 2017), in the absence of a source of replenishment. Although ion escape is likely important for M-Earths, we do not include it in our current study. Instead, we solely focus on the energy-limited escape of Luger & Barnes (2015), adopting the same efficiency of 30% to test similar loss rates.

Our loss parameterization is piecewise-defined so that we do not lose more water than present on the surface in a given timestep. The exponential definition of loss to space stems from the exponential decrease of the M dwarf’s XUV luminosity, and includes a loss factor, ϕ_{loss}, and loss timescale, τ_{loss}. The former accounts for the range of water loss rates in the literature, and represents the energy-limited loss rate in a single variable, ϕ_{loss}; the latter represents the e-folding timescale of water loss to space, i.e., water loss is reduced by $1/e$ after τ_{loss}. For simplicity, we model loss of water directly to space from the surface. This approximation should be valid if the atmosphere is hot – and hence moist – in the era of high XUV. We include the hydrated layer check from Schaefer & Sasselov (2015) to ensure that the hydrated layer holds no more water than the surface itself.

The model explicitly depends on mantle temperature via the mid-ocean ridge spreading rate, $S(T)$. Moreover, we stop degassing if the mantle cools below the solidus temperature, since no more melt will be present in the boundary layer. We calculate the wet solidus temperature using the parameterization of Katz et al. (2003), since water in the mantle depresses the solidus of silicate minerals.

2.3 Simulation Results

We run simulations for various initial total water inventory, $W_{\rm m,0} + W_{\rm s,0}$, loss factor, $\phi_{\rm loss}$, and loss timescale, $\tau_{\rm loss}$. All simulations are run for 15 Gyr to allow our model to reach a steady state, if possible. Our parameter exploration is shown in Table 2.1. We test four orders of magnitude for both $\phi_{\rm loss}$ and $\tau_{\rm loss}$, due to the range of loss rates in the literature, and because of the large uncertainties in observations and models of M dwarfs. We also test various initial water inventories, since planets are expected to form with different volatile inventories due to stochastic delivery and accretion (Raymond et al. 2004, 2009). Note that all simulations begin with an initial mantle temperature of $T_0 = 3200$ K, i.e., $T_0 = 2T_{\rm ref}$, where $T_{\rm ref}$ is the reference temperature used in our thermal evolution calculations (detailed in Appendix 2.5.1).

Name	Parameter	Values Tested
Total water mass	$W_{\rm m,0} + W_{\rm s,0}$ [TO]	0.1, 1, 10, 25
Mantle temperature	T_0 [K]	3200
Loss factor	$\phi_{\rm loss}$ [TO/Gyr]	0.1, 1, 10, 100
Loss timescale	$\tau_{\rm loss}$ [Gyr]	10^{-3}, 10^{-2}, 10^{-1}, 1

Table 2.1: Parameter space for initial total water inventory, $W_{\rm m,0} + W_{\rm s,0}$, loss factor, $\phi_{\rm loss}$, and loss timescale, $\tau_{\rm loss}$. We initiate all simulations with the same mantle temperature, $T_0 = 2T_{\rm ref}$. Water mass is expressed in units of terrestrial oceans, where 1 TO $\approx 1.4 \times 10^{21}$ kg.

Each of the total water inventories from Table 2.1 is first run to steady-state partitioning between the mantle and surface reservoirs (Fig. 2.2), without loss to space and at a constant mantle temperature of $T = 3200$ K. To visualize the evolution of steady-state water partitioning as the mantle cools with time, we run simulations for various initial water inventories ($W_{\mathrm{m},0} + W_{\mathrm{s},0} = 0.1$, 1, 5, 10, 25, 50, 100 TO) at three constant mantle temperatures, $T = 3200$ K, 2500 K, 2000 K. As the mantle cools, the steady-state water partitioning moves towards the bottom right in Fig. 2.2, sequestering water in the mantle at the expense of surface water.

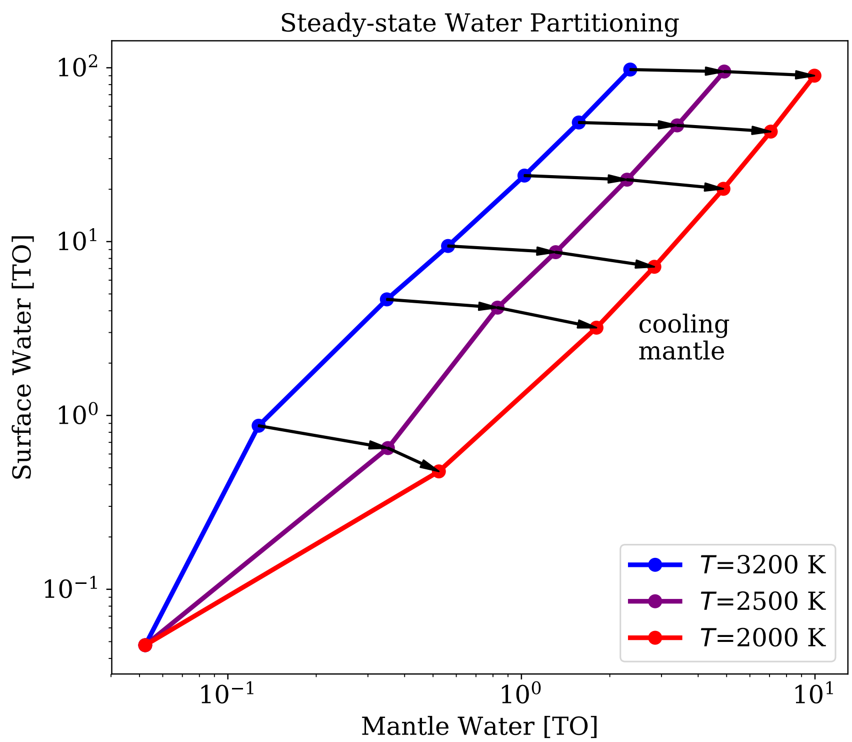

Figure 2.2: Steady-state water partitioning between surface, W_{s}, and mantle, W_{m}, reservoirs in units of terrestrial oceans (TO), for different mantle temperatures. Since the mantle cools with time, we would expect the steady state to change as well. Indeed, the steady-state curves shift towards the lower right; cooler temperatures lead to less surface water and more mantle water. For a given total water inventory and mantle temperature, there is a unique steady-state partitioning of water, and that is precisely the partitioning we use when initializing simulations in Figs. 2.3 & 2.4.

Schaefer et al. (2016) modelled atmosphere-interior exchange on a hot M-Earth, GJ 1132b, to determine atmospheric composition, beginning with a magma ocean and allowing solidification, and including loss to space, but the authors only simulate the first few 100 Myr. Our simulations begin after magma ocean solidification, once the steam atmosphere has mostly condensed onto the surface, and plate tectonics permit cycling. Nonetheless, our initial partitioning is qualitatively consistent with Schaefer et al. (2016), with the majority of water on the surface.

We are concerned with the surface water as it directly impacts habitability. We define four surface water regimes: a Dune planet, 10^{-5} TO $\leq W_{\rm s} < 10^{-2}$ TO (Abe et al. 2011); an Earth-like regime, 10^{-2} TO $\leq W_{\rm s} < 10$ TO; and a waterworld, where the surface is completely inundated, $W_{\rm s} \geq 10$ TO (Abbot et al. 2012)[1]. We designate planets with $\lesssim 0.1\%$ of the surface water of a Dune planet as desiccated. This is the amount of water currently in the atmosphere of Earth (1.29×10^{16} kg, or $\sim 10^{-5}$ TO; Gleick 1993); this amount of water is similar to Lake Superior. If precipitated onto the surface, it would produce a global ocean of depth ~2.5 cm (Graham 2010). While Dune planets, Earth-like planets, and waterworlds all have at least some liquid surface water and are thus habitable, only Earth-like planets are likely to have a silicate weathering thermostat.

If surface desiccation occurs, then regassing stops. Degassing will continue if the mantle is still warm; once the degassing rate surpasses the loss rate, surface water will increase. The surface is rehydrated when it exceeds our desiccation limit of $\sim 10^{-5}$ TO.

[1]The waterworld definition of Wordsworth & Pierrehumbert (2013) is similar — all land is covered by water, but this does not completely inhibit degassing from the interior. We assume this as well for M-Earths in the waterworld regime.

2.3.1 Individual Cycling Results

We first show the time-dependent cycling and loss results for two simulations from the parameter exploration (Fig. 2.3). Both begin with $W_{\mathrm{m},0} + W_{\mathrm{s},0} = 1$ TO of water, and loss factor $\phi_{\mathrm{loss}} = 10$ TO/Gyr. The "short loss" simulation uses a loss timescale of $\tau_{\mathrm{loss}} = 10^{-2}$ Gyr, while the "extreme loss" uses a longer loss timescale, $\tau_{\mathrm{loss}} = 10^{-1}$ Gyr. Since loss to space is occurring over a longer period for the latter, we expect a stronger reduction in surface water.

Water cycling with short loss is shown in Fig. 2.3(a). Degassing, $w_{\uparrow}$, and regassing, $w_{\downarrow}$, are initially equal since we begin our cycling simulation from steady-state water partitioning. As a result, there is much more water on the surface, W_{s}, than in the mantle, W_{m} (top panel). The loss rate to space, w_{loss}, is initially higher than the cycling rates.

Loss to space initially dominates, reducing the surface water inventory, which reduces the amount available to sequester back into the mantle at late times. The cycling rates surpass the loss rate at $t \approx \tau_{\mathrm{loss}} = 10^{-2}$ Gyr, and as loss slows, the water partitioning seeks a new steady state for the current total water inventory and cooler mantle temperature, T.

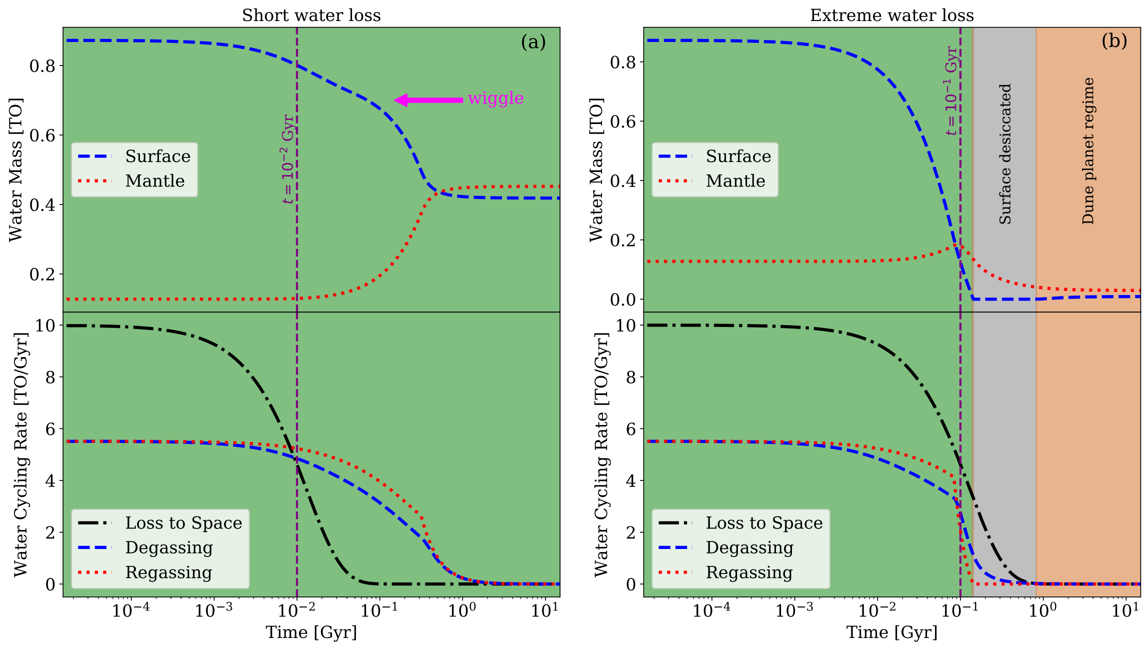

Short water loss
Extreme water loss
(a)
(b)
wiggle
$t = 10^{-2}$ Gyr
$t = 10^{-1}$ Gyr
Surface desiccated
Dune planet regime
Water Mass [TO]
Water Cycling Rate [TO/Gyr]
Surface
Mantle
Loss to Space
Degassing
Regassing
Time [Gyr]

Figure 2.3 *(previous page)*: (a) Water cycling with short-lived loss of water to space. The top panel shows water partitioning between mantle, W_m, and surface, W_s, over time, while the bottom panel shows the evolution of the degassing, $w_\uparrow$, regassing, $w_\downarrow$, and loss, w_loss, rates. Since we begin the simulation at steady-state partitioning, $w_{\uparrow,0} \simeq w_{\downarrow,0}$. The surface reservoir (top) is directly affected by loss to space; the loss rate is initially much higher than the cycling rates (bottom). Around $t = \tau_\mathrm{loss} = 10^{-2}$ Gyr, the cycling rates surpass the loss rate, causing the wiggle in W_s as cycling and loss compete to affect the surface water. Since regassing exceeds degassing during this time, some surface water is lost to space, while some is sequestered in the mantle. Eventually, the loss diminishes sufficiently to allow for a new steady state with a smaller total water inventory and cooler mantle temperature. The steady-state conditions will persist until the mantle cools below the solidus and degassing stops, which does not occur by 15 Gyr in this simulation. Despite the initial effect of water loss to space, the planet remains Earth-like throughout the simulation (as indicated by the green shaded region). (b) Extreme water loss, where the loss timescale is now 10× longer than Fig. 2.3(a). Note that the plotted loss rate, w_loss, in the bottom panel is an upper limit on the actual water lost, which is limited by the amount of water on the surface, W_s. The loss of water to space causes rapid reduction of surface water, W_s (top); the planet briefly exists in the Dune planet regime (thin left brown region), but regassing, $w_\downarrow$, quickly approaches zero (bottom) as the remaining surface water is lost, approaching desiccation just after $t = \tau_\mathrm{loss} = 10^{-1}$ Gyr. During the grey region, the surface briefly becomes desiccated by loss (i.e., $W_\mathrm{s} \to 0$), which completely stops regassing, so cycling only occurs in one direction; water degassed after this time is immediately lost to space since the loss rate, w_loss, still exceeds degassing, $w_\uparrow$. The degassing rate eventually surpasses the loss rate, and the surface is able to recover into the Dune planet regime (right brown region) before $t = 1$ Gyr. Since τ_loss is 10× longer than in Fig. 2.3(a), there is significantly less total water present on the planet by 15 Gyr; since the mantle remains warm and cycling continues, however, a new steady state is again approached.

The results for the extreme water loss simulation are shown in Fig. 2.3(b). The cycling begins similarly to the previous simulation, but the surface is rapidly desiccated (grey region). Degassing still provides water to the surface, where some is lost to space and a small amount is regassed, gradually reducing the mantle water inventory, while the surface water complement approaches zero.

Eventually, degassing from the mantle surpasses loss to space, and the surface recovers enough water to once again become a Dune planet (brown region). Even with continued cycling, there is not enough total water remaining on the planet to recover Earth-like surface conditions. Nonetheless, Fig. 2.3(b) demonstrates that water sequestered in the mantle can rehydrate the surface once loss to space diminishes.

2.3.2 Parameter Exploration

We now perform an exploration of the parameter space in Table 2.1. We focus on the final surface water inventories to determine what surface conditions to expect after 15 Gyr of water cycling and loss to space. Our results for the 64 simulations are illustrated in Fig. 2.4. We choose initial water inventories up to $W_{\rm m,0} + W_{\rm s,0} = 25$ TO, far below the high-pressure ice limit of $W_{\rm s,max} = 100$ TO (Nakayama et al. 2019), to allow plate tectonic-driven cycling to continue uninhibited.

As shown in Fig. 2.4, planets can evolve between surface water regimes. Certain rates of water loss to space cause waterworlds (blue) to lose sufficient water to expose continents and become Earth-like (similar to the "waterworld self-arrest" of Abbot et al. 2012), or Earth-like planets (green) to become dry Dune planets (brown) with little surface water, or even develop a completely desiccated, uninhabitable surface.

Water loss is limited by the amount of water on the surface (top left panel, Fig. 2.4). A loss rate of 10 TO/Gyr and a loss timescale of 0.1 Gyr might in principle desiccate a planet with a 0.1 TO inventory, but since the loss predominantly happens early in the evolution, it only removes the surface water present at that time.

Fig. 2.4 only shows the initial and final surface water contents, but we check for

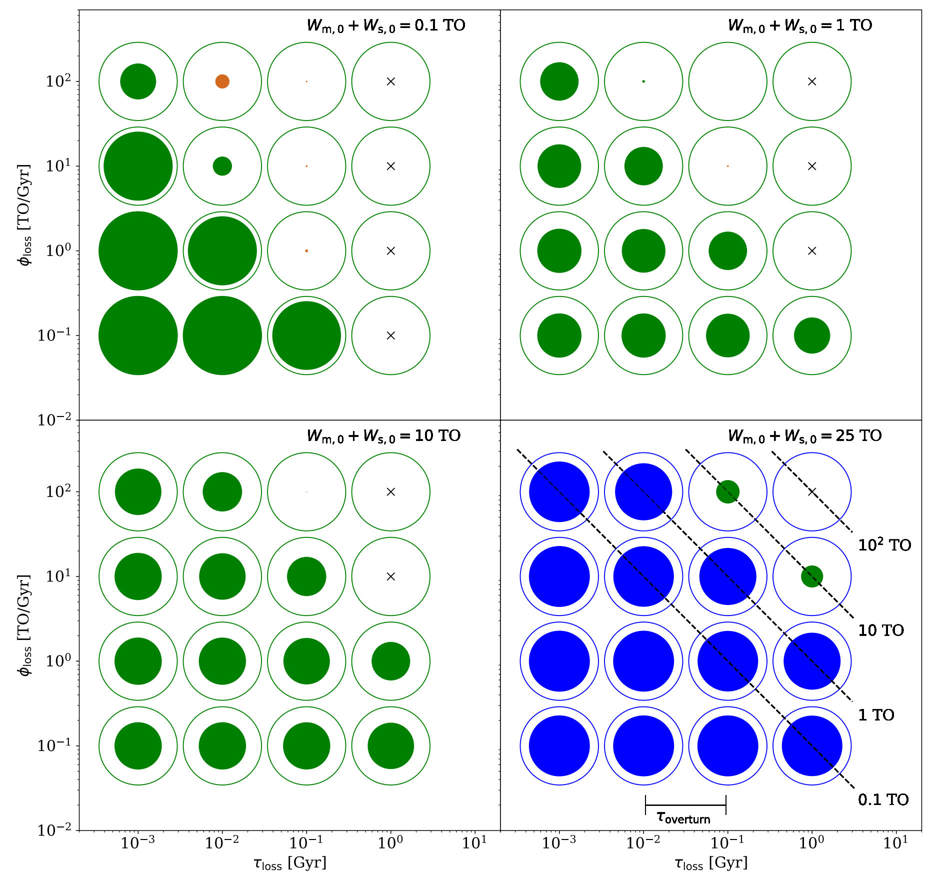

Figure 2.4: Evolution of surface water, W_s, for different loss factors, ϕ_{loss}, and loss timescales, τ_{loss}. The maximum amount of water a planet could lose is $\phi_{loss} \times \tau_{loss}$, as indicated in the bottom-right panel; diagonals correspond to simulations with equal $\phi_{loss}\tau_{loss}$. The open circles represent the amount of initial surface water, and the filled circles the surface water after 15 Gyr of cycling and loss to space. Colours indicate the surface water regime: waterworlds are blue, Earth-like planets are green, Dune planets are brown, and a desiccated surface is indicated by a black x. The initial total water inventories, $W_{m,0} + W_{s,0}$, are shown in the upper right of each panel, and filled circles are scaled based on the initial surface water of the open circles to visualize water loss. Planets subjected to water losses greater than their initial inventory, $\phi_{loss}\tau_{loss} \geq W_{m,0} + W_{s,0}$, would naively be expected to end up desiccated. Water sequestration in the mantle changes the picture dramatically, halving the simulations ending in desiccation. The approximate range of mantle overturn timescale, $\tau_{overturn}$, is indicated in the bottom-right panel; mantle overturn is faster at early times and slows as the mantle cools. Planets are able to evolve between surface water regimes (e.g., Earth-like to Dune planet, or waterworld to Earth-like), but also able to recover water on a desiccated surface at later times by degassing water sequestered in the mantle.

mid-simulation desiccation, as shown in Fig. 2.3(b). Ten of the 64 simulated planets recover from desiccation into either the Dune or Earth-like regime. This further supports our mechanism of sequestering water in the mantle and degassing it once atmospheric loss has decreased appreciably to restore habitable surface conditions.

2.4 Discussion & Conclusions

Our simulations show that sequestering water in the mantle and subsequent degassing enhances the likelihood of habitable M-Earths in the face of atmospheric loss, provided they have an Earth-like deep-water cycle.

2.4.1 Model Timescales

There are three relevant timescales in our model that permit a more thorough interpretation of our results (Figs. 2.3 & 2.4). These timescales are the time to reach steady state, τ_{ss}, the loss timescale, τ_{loss}, and the mantle overturn timescale, τ_{overturn}.

The surface water content and mantle temperature in our model change with time, not only due to loss but also water degassed and regassed from and to the mantle, respectively. The planet will therefore be approaching a changing steady state with time (Fig. 2.2). This steady state will not be reached until loss diminishes and mantle cooling slows at late times, allowing degassing and regassing rates to equilibrate. Indeed, we only see steady state achieved late in our simulations, and only as long as the mantle remains warm.

If the loss timescale is much longer than the mantle overturn timescale, $\tau_{\text{loss}} \gg$

τ_{overturn}, the water lost to space will be roughly $\phi_{\text{loss}}\tau_{\text{loss}}$, provided there is sufficient total water on the planet. This explains the different results for the same $\phi_{\text{loss}}\tau_{\text{loss}}$ in Fig. 2.4. Since the time to reach steady-state is closely related to the mantle overturn timescale, $\tau_{\text{loss}} \gg \tau_{\text{overturn}}$ also means that the planet is always at or near a steady state (equal degassing and regassing), but that steady state is a moving target due to atmospheric loss.

If $\tau_{\text{loss}} \ll \tau_{\text{overturn}}$, however, the total water lost is now limited by the initial surface water on the planet, $W_{\text{s},0}$. Since most loss happens early on and the loss rate diminishes with time, the surface can eventually be rehydrated, provided there is sufficient water sequestered within the mantle. This explains the similar results seen in each panel of Fig. 2.4, on the left and bottom-left. The greater a planet's initial water inventory, the farther towards the upper-right corner this plateau extends.

In summary, the total amount of water lost, W_{lost}, is,

$$W_{\text{lost}} = \begin{cases} \min[\phi_{\text{loss}}\tau_{\text{loss}},\ W_{\text{s},0} + W_{\text{m},0}] & \tau_{\text{loss}} \gg \tau_{\text{overturn}} \\ \min[\phi_{\text{loss}}\tau_{\text{loss}},\ W_{\text{s},0}] & \tau_{\text{loss}} \ll \tau_{\text{overturn}}. \end{cases} \tag{2.3}$$

2.4.2 Thermal Evolution & Tectonic Mode

The model can approach a steady state once loss has diminished significantly, as long as the mantle remains above the solidus temperature. Once the mantle cools below the solidus temperature, degassing stops due to the absence of melt below mid-ocean ridges. This leads to regassing-dominated evolution, eventually trapping all water in the mantle (Schaefer & Sasselov 2015).

It has been postulated, however, that when the mantle cools below the solidus temperature or becomes desiccated, convection may stop, along with plate tectonics, transitioning to a "stagnant lid" regime (Noack & Breuer 2014; Lenardic 2018). As noted by Schaefer & Sasselov (2015), transitioning to a stagnant lid would stop both degassing and regassing, preserving the water inventories in surface and mantle reservoirs at that time. A stagnant lid would greatly affect our cycling parameterizations, but volatiles can still be cycled in a stagnant-lid regime, albeit at a much slower rate (Höning et al. 2019). We leave this complication for future work; however, since our current simulations sometimes regas all water into the mantle, presumably accounting for a stagnant lid would merely result in more surface water at late times.

2.4.3 Observational Prospects

Observationally characterizing M-Earth atmospheres in the near future is viable (Cowan et al. 2015; Shields et al. 2016; Gillon et al. 2020), but direct detection of surface water on an exoplanet is probably still many years away (Cowan et al. 2009; Robinson et al. 2010; Lustig-Yaeger et al. 2018). To zeroth-order, our conclusions support continued observations of M dwarf systems in the search for habitability. Our results will be useful in interpreting observations, allowing inference of the cycling & loss history of M-Earths based on, e.g., the presence of H_2O in transit spectra. Connecting surface water to climate, atmospheric structure, and transit spectroscopy will be the subject of a future study. Increasing the fidelity of our M-Earth water cycling & loss model will narrow the gap between predictions and observations.

The key variables in our model include the initial water inventory, the initial water partitioning, the mantle overturn timescale, the loss rate and the loss timescale.

The initial water inventory may be difficult to determine due to the stochastic nature of volatile delivery during planet formation (Raymond et al. 2004, 2009); however, studies of volatiles in protoplanetary disks (e.g., using ALMA; Harsono et al. 2020; Loomis et al. 2020) and studies of polluted white dwarfs (e.g., Farihi 2016; Veras et al. 2017a,b; Doyle et al. 2019) may provide constraints. The geophysical processes that determine both the planetary water partitioning and mantle overturn timescale in our M-Earth model are based on present-day Earth. Determining the tectonic mode of an observed exoplanet will be difficult in the near future, but in principle, may be possible with LUVOIR (e.g., Cowan et al. 2009); nonetheless, modelling can allow exploration of the potential geophysics on distant planets. Many uncertainties in our model arise due to our treatment of stellar evolution, but we may be able to constrain the loss rate (i.e., the loss factor and timescale) through a combination of M dwarf observations and modelling to better represent the governing loss processes on an M-Earth.

Acknowledgements

We thank the anonymous referee for a beneficial referee report that strengthened this manuscript. We thank Tad Komacek for providing his hybrid model and for valuable correspondence while re-coding the model. We also acknowledge thesis committee members Yajing Liu, Vincent van Hinsberg, Don Baker, Galen Halverson, and Timothy Merlis, as well as insightful conversations with Christie Rowe and Mark Jellinek. We thank Dylan Keating and Lisa Dang for comments on a draft of this manuscript. K.M. acknowledges support from a McGill University Dr. Richard H. Tomlinson Doctoral Fellowship, and from the Natural Sciences and Engineering Research Council of Canada (NSERC) Postgraduate Scholarships-Doctoral Fellowship.

Data Availability

The model and data presented within this manuscript are available from the corresponding author at reasonable request.

2.5 Appendix

2.5.1 Thermal Evolution Equations

The thermal evolution of the mantle in our model, which incorporates parameterized convection, is a simplified version of the thermal evolution presented within Schaefer & Sasselov (2015), itself based on the model of Sandu et al. (2011). For simplicity, and to reproduce the low-viscosity model which reaches an analytic steady state (the goal of Komacek & Abbot 2016), the convection is constrained to a boundary layer in the upper mantle.

The evolution of the mantle temperature, T, with time, t, in our model is dependent on mantle water mass fraction $x = W_\mathrm{m}/M_\mathrm{m}$, where M_m is the mass of the mantle. The thermal evolution equation is:

$$\begin{aligned}\rho_\mathrm{m} c_\mathrm{p} \frac{dT}{dt} &= Q(t) - \frac{A}{V}\frac{k\Delta T}{h}\left(\frac{\mathrm{Ra}}{\mathrm{Ra}_\mathrm{crit}}\right)^{\beta} \\ &= Q(t) - \frac{kA\Delta T}{hV}\left(\frac{\alpha\rho_\mathrm{m} g h^3 \Delta T}{\mathrm{Ra}_\mathrm{crit}\kappa\eta(T,x)}\right)^{\beta}.\end{aligned} \tag{2.4}$$

The value of $\beta = 0.3$ in this equation was determined empirically (McGovern & Schubert 1989). The density of the upper mantle is ρ_{m}, and c_{p} is the mantle's specific heat capacity. The heating rate from radionuclides is $Q(t) = Q_0 \exp^{-t/\tau_{\mathrm{decay}}}$. The decay timescale $\tau_{\mathrm{decay}} = 2$ Gyr was nominally chosen by Komacek & Abbot (2016), based on the abundance and half-lives of radiogenic elements in the Earth's mantle from Turcotte & Schubert (2002). For reference, this value falls between the half-lives of ^{40}K (1.3 Gyr) and ^{238}U (4.5 Gyr). The thermal conductivity of the upper mantle is k, and $\Delta T = T - T_{\mathrm{s}}$ is the temperature contrast across the boundary layer, with T_{s} the surface temperature.

The scaling laws of terrestrial planets from Valencia et al. (2006) allow us to calculate the planet's mantle thickness, h, the planet's surface area, A, the mantle volume, V, and surface gravity, g. Planetary radius, R, and core radius, R_{c}, are related to planetary mass, M, by

$$R = R_{\oplus} \left(\frac{M}{M_{\oplus}} \right)^{p}, \tag{2.5}$$

$$R_{\mathrm{c}} = c R_{\oplus} \left(\frac{M}{M_{\oplus}} \right)^{p_{\mathrm{c}}}, \tag{2.6}$$

where $p = 0.27$, $c = 0.547$, and $p_{\mathrm{c}} = 0.25$. The remaining planet and mantle properties are:

$$h = R - R_{\mathrm{c}}, \tag{2.7}$$

$$A = 4\pi R^2, \tag{2.8}$$

$$V = \frac{4\pi}{3}(R^3 - R_{\mathrm{c}}^3), \tag{2.9}$$

$$g = \frac{GM}{R^2}. \tag{2.10}$$

The Rayleigh number of the mantle, $\mathrm{Ra} = \alpha\rho_{\mathrm{m}} g h^3 \Delta T/\kappa\eta(T,x)$, can be calculated using the upper mantle density, ρ_{m}, mantle thickness, h, and temperature contrast, ΔT, along with the characteristic thermal expansivity, α, the planet's gravity, g, and the thermal diffusivity of the boundary layer, κ. The critical Rayleigh number for convection to occur in the upper mantle is $\mathrm{Ra}_{\mathrm{crit}} = 1100$ (McGovern & Schubert 1989). Due to the dependence of temperature T on mantle water mass fraction x, the thermal evolution and cycling equations are integrated simultaneously.

For the mantle viscosity, $\eta(T,x)$, we use the same parameterization as Komacek & Abbot (2016), which in turn is a simplified version of that from the models of Sandu et al. (2011) and Schaefer & Sasselov (2015) (i.e., without the pressure-dependence, since we are restricted to the upper mantle):

$$\eta \approx \eta_0 f_{\mathrm{w}}^{-r} \exp\left[\frac{E_{\mathrm{a}}}{R_{\mathrm{gas}}}\left(\frac{1}{T} - \frac{1}{T_{\mathrm{ref}}}\right)\right]. \tag{2.11}$$

Here, η_0 is the viscosity scale (chosen so that $\eta(x = x_{\oplus}, T = T_{\mathrm{ref}}) = 10^{21}$ Pa·s to reproduce the viscosities of Earth's mantle), E_{a} is the activation energy, R_{gas} is the universal gas constant, $T_{\mathrm{ref}} = 1600$ K is the reference mantle temperature, f_{w} is water fugacity (see Eqn. 2.12 below), and $r = 1$ is the nominal value chosen by Schaefer & Sasselov (2015), based on measurements of wet olivine diffusion.

The water fugacity, f_{w}, can be calculated using experimental data from Li et al.

(2008),

$$\ln f_{\mathrm{w}} = c_0 + c_1 \ln\left(\frac{Bx\mu_{\mathrm{oliv}}/\mu_{\mathrm{w}}}{1 - x\mu_{\mathrm{oliv}}/\mu_{\mathrm{w}}}\right) + c_2 \ln^2\left(\frac{Bx\mu_{\mathrm{oliv}}/\mu_{\mathrm{w}}}{1 - x\mu_{\mathrm{oliv}}/\mu_{\mathrm{w}}}\right) + c_3 \ln^3\left(\frac{Bx\mu_{\mathrm{oliv}}/\mu_{\mathrm{w}}}{1 - x\mu_{\mathrm{oliv}}/\mu_{\mathrm{w}}}\right), \tag{2.12}$$

where $c_0 = -7.9859$, $c_1 = 4.3559$, $c_2 = -0.5742$, $c_3 = 0.0337$, $B = 2 \times 10^6$ (which converts to number concentration of H atoms per 10^6 Si atoms), μ_{oliv} is the molecular weight of olivine, and μ_{w} is the molecular weight of water.

2.5.2 Model Improvements & Constraints

Our improvements to the hybrid model of Komacek & Abbot (2016) include restoring the degassing limit from Cowan & Abbot (2014), and capacity limits for mantle water (to account for a saturated mantle, $W_{\mathrm{m}} \leq 12$ TO; Hauri et al. 2006; Cowan & Abbot 2014) and surface water ($W_{\mathrm{s}} \leq 100$ TO, above which high-pressure ices will form at the ocean floor and significantly alter or hinder the degassing/regassing rates; Nakayama et al. 2019).

The addition of a simultaneous loss term in the cycling equations brings the model closer to predictions for XUV-driven water loss to space on M-Earths (e.g. Luger & Barnes 2015). Our current loss factors, ϕ_{loss}, and timescales, τ_{loss}, allow for a phenomenological exploration of parameter space to show the effect of water loss rather than being directly calculated from, for example, stellar evolution models of XUV flux from M dwarfs (e.g., Ribas et al. 2005).

While coupled integrations of the thermal evolution in Eqn. 2.4 and the cycling of Eqns. 2.1 and 2.2 can be performed using the `scipy.integrate` package in Python, restrictions must be placed to ensure we do not obtain meaningless, unphysical results. Our hybrid model is robust to either or both reservoirs going to zero, an improvement over Komacek & Abbot (2016). At each timestep, surface and mantle water inventories are checked, and the cycling equations are adjusted accordingly:

1. If mantle water mass $W_{\rm m}$ and surface water mass $W_{\rm s}$ are both greater than zero, then normal cycling and loss occurs, and the cycling equations are integrated as they appear in §2.2.

2. If $W_{\rm m} = 0$ but $W_{\rm s} > 0$, the degassing rate, $w_{\uparrow}$, is set to zero (i.e., it shuts off since there is no water in the mantle) in Eqns. 2.1 and 2.2, and the integration is performed.

3. If $W_{\rm m} > 0$ but $W_{\rm s} = 0$, the regassing rate, $w_{\downarrow}$, and loss rate, $w_{\rm loss}$, are set to zero (since there is no water on the surface) in Eqns. 2.1 and 2.2, and the integration is performed. We also set the fraction of water in melt that is degassed $f_{\rm degas}(P) = 1$, due to its piecewise definition. We do this because the P-dependent degassing rate depends on the overlying surface water, $W_{\rm s}$; if there is no water on the surface, degassing should neither go to zero and shut off (or else water would stay in the mantle indefinitely), nor go to infinity (or all water would be instantaneously degassed from the mantle).

4. If both $W_{\rm m} = 0$ and $W_{\rm s} = 0$, the degassing, regassing, and loss rates are all set to zero, since the planet is completely desiccated. The integration continues so we can observe the thermal evolution of the mantle (i.e., its cooling with time), but there is no cycling or loss since there is no more water present on the surface or within the mantle of the planet.

Our piecewise definition of loss in Eqn. 2.2 ensures that the amount of surface water that is regassed and lost at a given timestep does not exceed the amount present on the surface, and the regassing/loss rates are adjusted accordingly based on the surface water mass, W_s.

Although it is a result we have yet to encounter, to account for complete mantle desiccation (a scenario proposed in the literature; see, e.g., Hamano et al. 2013), we choose a minimum water fugacity to avoid $f_w \to 0$ and mantle viscosity $\eta \to \infty$. We can then define a piecewise mantle water fugacity, $f_{w,eff}$, represented by the equation,

$$f_{w,eff} = \max[10^{-5} f_w(\tilde{x} = 1),\ f_w] \tag{2.13}$$

where $f_w(\tilde{x} = 1)$ is used to define the non-dimensional fugacity within our model code, $\tilde{f}_w = f_w/f_w(\tilde{x} = 1)$. This definition requires the non-dimensional water mass fraction $\tilde{x} = x f_m/(\omega_0 \tilde{f}_b)$, where f_m is the mantle fraction, ω_0 is the surface water mass fraction of Earth, and $\tilde{f}_b = f_b/f_{b,\oplus} = 1.3$ is the non-dimensional ocean basin covering fraction, with $f_{b,\oplus} = 0.7$ and $f_b = 0.9$ (i.e., 90% of planet covered in water). The value for f_b was chosen by Cowan & Abbot (2014), which we also optimistically adopt for an Earth-like planet.

The minimum value, $f_{w,eff} = 10^{-5} f_w(\tilde{x} = 1)$, assumes that even in the case of a completely desiccated mantle, there will be a small amount of water trapped in the minerals (e.g., within the transition zone; Hirschmann 2006). This allows the mantle to continue convecting and our plate-tectonics-dependent cycling to proceed. Note that, throughout the thermal evolution equations presented above, f_w is used in place of $f_{w,eff}$ for consistency with the literature.

Finally, we note that the water fugacity was calculated incorrectly in many places in the original hybrid cycling model due to a misplaced bracket (Komacek 2019, priv. comm.). While this error does not significantly impact the final results, it does slightly change the time-dependent cycling results, and has been fixed in the model presented here.

2.5.3 Model Parameters

There are many variables throughout this paper. As such, we detail them all in Table 2.2, including their nominal values.

Name	Parameter	Value
Mantle water mass[ab]	$W_{\rm m}$	$W_{\rm m,\oplus} = 2.36 \times 10^{21}$ kg ≈ 1.7 TO
Surface water mass[ab]	$W_{\rm s}$	$W_{\rm s,\oplus} \approx 1.4 \times 10^{21}$ kg $= 1$ TO
Mantle temperature[a]	T	$T_{\rm ref} = 1600$ K
Loss factor[b]	$\phi_{\rm loss}$	10 TO Gyr^{-1}
Loss timescale[b]	$\tau_{\rm loss}$	10^8 yr
Mid-ocean ridge length	$L_{\rm MOR}$	$L_{\rm MOR,\oplus} = 60 \times 10^6$ m
Spreading rate[a]	S	$S_{\oplus,\rm avg} \approx 0.1$ m yr^{-1}
Water mass fraction in hydrated crust	$x_{\rm h}$	0.05
Crust density	$\rho_{\rm c}$	3.0×10^3 kg m^{-3}
Regassing efficiency	$\chi_{\rm r}$	0.03
Hydrated layer depth[a]	$d_{\rm h}$	$d_{\rm h,\oplus} = 3.0 \times 10^3$ m
Mantle water mass fraction	x	$x_\oplus = 5.8 \times 10^{-4}$
Mantle density	$\rho_{\rm m}$	3.3×10^3 kg m^{-3}
Mid-ocean ridge melting depth	$d_{\rm melt}$	60×10^3 m
Melt degassing efficiency of Earth	$f_{\rm degas,\oplus}$	0.9
Seafloor pressure[a]	P	$P_\oplus = 4 \times 10^7$ Pa
Timestep	$\tau_{\rm step}$	$\sim$28700 yr
Mantle overturn timescale	$\tau_{\rm overturn}$	$\tau_{\rm overturn,\oplus} \approx 6 \times 10^6$ yr
Mantle specific heat capacity	$c_{\rm p}$	1200 J kg^{-1} K^{-1}
Radionuclide decay factor	Q_0	5×10^{-8} J m^{-3} s^{-1}
Decay timescale	$\tau_{\rm decay}$	2 Gyr
Mantle thermal conductivity	k	4.2 W m^{-1} K^{-1}
Surface temperature	$T_{\rm s}$	280 K
Mantle critical Rayleigh number	${\rm Ra}_{\rm crit}$	1100
Heat flux exponent	β	0.3
Mantle characteristic thermal expansivity	α	2×10^{-5} K^{-1}
Mantle thermal diffusivity	κ	10^{-6} m^2 s^{-1}
Planet radius	R	$R_\oplus = 6.371 \times 10^6$ m
Planet mass	M	$M_\oplus = 5.972 \times 10^{24}$ kg
Gravitational constant	G	6.67×10^{-11} m^3 kg^{-1} s^{-2}
Mantle viscosity[a]	η	$\eta(x = x_\oplus, T = T_{\rm ref}) = 10^{21}$ Pa s
Water fugacity[a]	$f_{\rm w}$	$f_{\rm w}(x_\oplus) \approx 17 \times 10^3$ Pa
Fugacity exponent	r	1
Activation energy	$E_{\rm a}$	335×10^3 J mol^{-1}
Universal gas constant	$R_{\rm gas}$	8.314 J mol^{-1} K^{-1}
Molecular weight of olivine	$\mu_{\rm oliv}$	153.31 g mol^{-1}
Molecular weight of water	$\mu_{\rm w}$	18.02 g mol^{-1}
Planetary mantle fraction	$f_{\rm m}$	0.68
Ocean basin covering fraction	$f_{\rm b}$	0.9
Earth ocean basin covering fraction	$f_{\rm b,\oplus}$	0.7

Notes.

[a]: These parameters are calculated during our coupled thermal evolution and cycling & loss integrations.

[b]: These parameters are varied during our parameter exploration.

Table 2.2: Parameters & constants used in our M-Earth thermal evolution and cycling & loss model. The corresponding equations from which they are taken appear throughout this paper.

Interlude I

This chapter presented our first iteration of a coupled deep-water cycling & atmospheric loss to space box model, with simulations exploring a parameter space to investigate whether this coupled model could improve otherwise negative habitability prospects. For the remainder of my Ph.D., I continued to improve and build upon this coupled box model to further study the habitability of terrestrial planets around M-dwarf stars. Following completion of this first paper, I believed the best next step would be to improve the parameterized atmospheric loss through adding a 1-D pure water atmosphere on top of the box model, and began a literature search on the topic of rocky planet atmospheres. To help with this, we contacted Colin Goldblatt at the University of Victoria, an expert on the runaway greenhouse and planetary atmospheres.

It proved quite difficult to reconcile a 1-D atmosphere with a 0-D box model, and in fact, the implementation of a 1-D atmosphere became unnecessary. The timesteps within our simulations were much longer than the time it would take to replenish water lost from the upper atmosphere, and hence we could treat the atmospheric reservoir as a subset of the surface reservoir. This brief collaboration provided us with data to calculate the surface temperature for a planet with a pure water atmosphere (Goldblatt et al. 2013), given its absorbed flux from the host star which could be determined, given some orbital distance, using M-dwarf stellar models (Baraffe et al. 2015); however, this was later simplified to a step function for surface temperature representing the hot, runaway greenhouse state, as well as the post-runaway, moderate temperature phase.

While creating this new model, however, we encountered another issue that seemed mostly unaddressed in the literature: the surface temperatures during the early, very hot runaway greenhouse meant that below the thick steam atmosphere, the rocky surface was molten. Since the runaway greenhouse phase accounted for the earliest evolution of the planet, we would need to account for this molten surface. By chance, we had been introduced to Charles-Édouard Boukaré, a French postdoctoral geophysicist working in Montreal on planetary interiors and magma oceans. With this new collaboration, the direction for the next model iteration became clear: our box model simulations will begin from an early magma ocean phase before transitioning to deep-water cycling, while water may be lost to space throughout at a rate determined by its top-of-atmosphere irradiation.

Chapter 3

The Role of Magma Oceans in Maintaining Surface Water on Rocky Planets Orbiting M-Dwarfs

This thesis chapter originally appeared in the literature as
Moore, Cowan, & Boukaré 2023, *Monthly Notices of the Royal Astronomical Society (MNRAS), 526, 6235. https://doi.org/10.1093/mnras/stad3138*

Authors

Keavin Moore [1,2], Nicolas B. Cowan [1,2,3], Charles-Édouard Boukaré [4]

[1]Department of Earth & Planetary Sciences, McGill University, 3450 rue University, Montréal, QC H3A 0E8, Canada

[2]Trottier Space Institute, McGill University, 3550 rue University, Montréal, QC H3A 2A7, Canada

[3]Department of Physics, McGill University, 3600 rue University, Montréal, QC H3A 2T8, Canada

[4]Institut de Physique du Globe de Paris, 1 rue Jussieu, Paris CEDEX 05, 75238, France

Preface

In this chapter, we present the second iteration of our box model which improved both the atmospheric loss and the geophysics. The atmospheric loss is now calculated in one of two escape regimes, governed by the surface temperature through irradiation calculated from stellar evolution models. The magma ocean box model was inspired by previous magma ocean studies such as Elkins-Tanton (2008) and Hamano et al. (2013), and we adopted suitable values for each variable, assumed constant where appropriate; some uncertain variables were varied in an exploration of parameter space, such as the water saturation limit of the magma ocean and the planet's initial water inventory. The magma ocean water partitioning parameterization was based on Boukaré et al. (2019).

Although we initially treated the magma ocean solidification timescale as a free parameter and calculated the duration of the runaway greenhouse phase at some fixed orbital distance, this created a strange, unphysical stage where the surface had solidified but the runaway greenhouse was ongoing, meaning surface temperatures were still hot enough to melt the silicate surface. This led to another significant model improvement, where we directly tied the runaway greenhouse and magma ocean solidification together by assuming their timescales were the same, i.e., that the duration of the runaway greenhouse controls the solidification of the magma ocean.

There is also a suggestion in the literature that if the magma ocean solidifies from middle–out instead of bottom–up, a basal magma ocean may persist below the solid mantle for Gyr timescales (Labrosse et al. 2007), a significant fraction of our 5 Gyr simulations; it is even speculated that basal magma oceans may exist within the

Solar System. Because of this, we test another box model with a residual basal magma ocean — providing an additional internal reservoir for water — for comparison with the simulations without a basal magma ocean. This paper presents the simulation results for box models with and without a basal magma ocean, which further supports the idea that water sequestered in the planetary interior (whether magma ocean or solid mantle) can improve habitability prospects by reducing the amount of water lost to space, but this advantage is strongly dependent on the lifetime of a basal magma ocean, if one is present.

Abstract

Earth-like planets orbiting M-dwarf stars, M-Earths, are currently the best targets to search for signatures of life. Life as we know it requires water. The habitability of M-Earths is jeopardized by water loss to space: high flux from young M-dwarf stars can drive the loss of 3–20 Earth oceans from otherwise habitable planets. We develop a 0-D box model for Earth-mass terrestrial exoplanets, orbiting within the habitable zone, which tracks water loss to space and exchange between reservoirs during an early surface magma ocean phase and the longer deep-water cycling phase. A key feature is the duration of the surface magma ocean, assumed concurrent with the runaway greenhouse. This timescale can discriminate between desiccated planets, planets with desiccated mantles but substantial surface water, and planets with significant water sequestered in the mantle. A longer-lived surface magma ocean helps M-Earths retain water: dissolution of water in the magma provides a barrier against significant loss to space during the earliest, most active stage of the host M-dwarf, depending on the water saturation limit of the magma. Although a short-lived basal magma ocean can be beneficial to surface habitability, a long-lived basal magma ocean may sequester significant water in the mantle at the detriment of surface habitability. We find that magma oceans and deep-water cycling can maintain or recover habitable surface conditions on Earth-like planets at the inner edge of the habitable zone around late M-dwarf stars — these planets would otherwise be desiccated if they form with less than $\sim$10 terrestrial oceans of water.

3.1 Introduction

3.1.1 Habitability

Planetary habitability requires persistent liquid surface water. The habitable zone around a host star is classically defined as the orbital distance where the incoming stellar flux permits the existence of liquid surface water, assuming an Earth-like atmosphere and silicate weathering thermostat (Kasting et al. 1993; Abe 1993; Kopparapu et al. 2013), with the runaway greenhouse defining the inner edge and freeze-out of carbon dioxide the outer edge.

The surface water of an Earth-like planet orbiting in the habitable zone of an M-dwarf star is endangered due to flaring and X-ray and extreme ultraviolet radiation emitted by the host star, especially early on when the M-dwarf is most active. Surface temperatures are exceedingly hot and water is readily available in the upper atmosphere to be photodissociated and lost to space (e.g., Wordsworth & Pierrehumbert 2013, 2014; Luger & Barnes 2015; Bolmont et al. 2017a; Fleming et al. 2020).

M-Earths are common in the Galaxy (e.g., Dressing & Charbonneau 2015; Sabotta et al. 2021), motivating theoretical studies of their habitability using predictive coupled models including loss to space. Depending on the space environment and planetary processes, M-Earths could hold onto their surface water throughout their lifetime, recover habitable conditions through degassing of water sequestered within the mantle (Moore & Cowan 2020), or become desiccated by the intense irradiation.

3.1.2 The Runaway Greenhouse Phase

Earth-like planets rapidly form within the habitable zone of M-dwarf stars on Myr timescales (e.g., Raymond et al. 2007; Lissauer 2007; Ribas et al. 2014) or migrate into the habitable zone (e.g, Petrovich 2015a,b). Because of the extended, highly-active pre-main sequence phase of its host star, an M-Earth will be highly irradiated following its formation. High surface temperatures on a young M-Earth induce a moist greenhouse, and the high water vapour mixing ratio in the upper atmosphere permits the loss of water to space (Kasting et al. 1993). If it absorbs too much shortwave radiation then the M-Earth will enter a runaway greenhouse phase.

Classically, the runaway greenhouse occurs when the incoming irradiation exceeds a critical value; above this value, the moist atmosphere cannot emit sufficient longwave radiation. The oceans completely evaporate into an insulating steam atmosphere, and the greenhouse effect causes surface temperatures to "run away" (Ingersoll 1969; Kasting 1988; Nakajima et al. 1992; Goldblatt et al. 2013; Goldblatt 2016). The length of the runaway greenhouse phase will depend not only on the orbital distance and amount of water in the atmosphere, but also the partial pressure of carbon dioxide and rock vapour (due to the very high temperatures), which cause a blanketing effect. Importantly, since all surface water evaporates into the atmosphere during a runaway greenhouse, the planet is susceptible to lose substantial water to space.

3.1.3 Water Loss Regimes

Water may be lost to space from an M-Earth if it is present above the exobase, or driven by a strong hydrodynamic wind originating deeper in the atmosphere. The loss of water to space from M-Earths is driven by X-ray and extreme ultraviolet ("XUV"; 0.1–120 nm) radiation from the host M-dwarf, which decreases with time (Ribas et al. 2005; Luger & Barnes 2015). XUV radiation can photodissociate water molecules and drive their escape to space; for our study, this means the escape of hydrogen atoms as we do not explicitly track atmospheric oxygen. Since the amount of atmospheric water vapour increases with increasing temperature, a hotter planet will lose more water to space. The total amount of water lost may be limited by either incoming energy, or by vertical diffusion of molecules through the atmosphere.

We posit that the loss to space is energy-limited (Watson et al. 1981; Erkaev et al. 2007) when the planet is in a runaway greenhouse. For energy-limited escape, a fixed fraction of the incoming XUV flux, typically 1–10% (e.g., Ercolano & Clarke 2010; Barnes et al. 2016; Lopez 2017), powers the photodissociation of water and drives its loss to space. Following the end of the runaway greenhouse phase, once temperatures become more modest, the loss rate is the lower of energy-limited and diffusion-limited. Diffusion-limited escape describes a limit in the upwards diffusion of water towards the exobase (Hunten 1973); effectively, the diffusion limit corresponds to the vertical diffusion of hydrogen atoms through a background atmosphere of, e.g., oxygen or nitrogen. The diffusion limit applies to minor atmospheric species and thus would not be relevant in a steam atmosphere; however, assuming our model atmosphere consists of water, hydrogen, and oxygen, we can treat the diffusion limit as hydrogen diffusing vertically through an oxygen background.

3.1.4 Surface & Basal Magma Oceans

Surface temperatures of ∼1500–1800 K are expected during the runaway greenhouse phase (Kasting 1988; Goldblatt et al. 2013; Goldblatt 2016): a steam atmosphere overlies a molten surface — a surface magma ocean (MO) — which gradually solidifies from the bottom up over ∼10s–100s of Myr (e.g., Elkins-Tanton 2008; Hamano et al. 2013; Lebrun et al. 2013), although this may be extended due to tidal heating, enhanced irradiation, and additional greenhouse gases. The adiabat within the cooling MO crosses the liquidus and solidus. Hence, there are three distinct water reservoirs during the surface magma ocean phase: the steam atmosphere, the shrinking magma ocean, and the growing, solidifying mantle. The partitioning of water during this earliest stage of an M-Earth is critical in determining its water inventory, and its habitability, throughout the planet's lifetime (Ikoma et al. 2018).

The surface magma ocean is a substantial water reservoir due to the high solubility of water within silicate melts; indeed, for hot planets (such as the young M-Earths investigated in this study), the MO can hold onto enormous amounts of water, up to ∼10 wt.% (Dorn & Lichtenberg 2021), which is ∼427 Earth Oceans for an Earth-mass planet. This dissolution of water in the surface magma ocean protects water against the highest irradiation, and against escape to space due to XUV radiation.

A thick steam atmosphere could extend the surface magma ocean phase, prolonging a reservoir which could sequester substantial oxygen within the mantle (Barth et al. 2021) and preventing the build-up of abiotic O_2 in the atmosphere often associated with significant water loss to space (e.g., Luger & Barnes 2015; Krissansen-Totton et al. 2021b). Throughout this work, we refer to the early, post-formation magma ocean phase concurrent with the runaway greenhouse as a "surface magma ocean", to distinguish it from the later residual "basal magma ocean" underlying a solid mantle.

A basal magma ocean (BMO) may form if the mantle solidifies from the middle–out rather than from the bottom–up. A BMO will cool on the order of Gyrs (Labrosse et al. 2007; Blanc et al. 2020), providing a long-lived water reservoir protected from atmospheric loss. A BMO can also form by density cross-over between solid and liquid silicates (Boukaré et al. 2015; Boukaré & Ricard 2017; Caracas et al. 2019). Regardless of its origin, a BMO will solidify from the top–down, from the base of the solid mantle towards the core-mantle boundary (Labrosse et al. 2007). A basal magma ocean is likely more common for planets larger than Earth, and has recently been invoked for Venus (O'Rourke 2020), Mars (Samuel et al. 2021), and the Moon (Walterová et al. 2023).

3.1.5 Deep-Water Cycle

Active plate tectonics provides Earth with a deep-water cycle (McGovern & Schubert 1989): water is exchanged between surface and mantle reservoirs on geological timescales, driven by the creation and subduction of lithospheric plates. Water is degassed from mantle to surface through mid-ocean ridge volcanism, corresponding to the "upwelling" branch of plate tectonics. In the other direction, water is regassed from surface to mantle through subduction of hydrated oceanic crust, corresponding to the "downwelling" branch. Although other tectonic modes exist (e.g., stagnant lid, sluggish convection; Lenardic 2018; Lourenço et al. 2020), we restrict the current study to the plate-tectonic mode.

The paper is structured as follows. In Section 3.2, we outline the equations governing stellar evolution and the loss of water to space within our model. The methods and equations of our magma ocean and deep-water cycling models are then outlined in Section 3.3, followed by simulation results in Section 3.4. We then discuss our results in Section 3.5, and our conclusions in Section 3.6.

3.2 Stellar Evolution & Water Loss

We use stellar models of the bolometric luminosity of M-dwarf stars (Baraffe et al. 2015) to calculate the absorbed flux and surface temperature of a terrestrial planet orbiting in the habitable zone. These stellar models also allow us to calculate the host star's XUV flux as a function of time, and hence estimate the rate of water loss to space in either the energy-limited or diffusion-limited regimes.

During planet formation, the protoplanetary disk blocks XUV radiation for a few Myr of the ∼10 Myr formation timescale (e.g., Barth et al. 2021). Ribas et al. (2014) estimate the lifetimes of protoplanetary disks around low-mass stars to be 4.2–5.8 Myr. Following Ribas et al. (2014) and Barth et al. (2021), we choose to offset the stellar track of Baraffe et al. (2015) by 5 Myr to allow the circumstellar disk to dissipate and the M-Earth to be fully formed.

We parameterize the evolution of stellar XUV luminosity over time as (Ribas et al. 2005; Luger & Barnes 2015):

$$L_{\mathrm{XUV}}(t) = \begin{cases} f_{\mathrm{sat}} L_{\mathrm{bol}}(t), & t \leq t_{\mathrm{sat}}, \\ f_{\mathrm{sat}} \left(\frac{t}{t_{\mathrm{sat}}}\right)^{\beta_{\mathrm{XUV}}} L_{\mathrm{bol}}(t), & t > t_{\mathrm{sat}}. \end{cases}$$

Here, t corresponds to the time after the gas disk dissipates, $L_{\rm bol}(t)$ is the bolometric luminosity interpolated from the stellar tracks of Baraffe et al. (2015), $f_{\rm sat} = 10^{-3}$ is the saturation fraction, $\beta_{\rm XUV} = -1.23$, and $t_{\rm sat} = 1$ Gyr is the assumed constant saturation time of an M-dwarf. The timescale of spin-down for M-dwarfs — signalling the end of their highly active phase — is poorly constrained, and may vary from as low as 600 Myr to >3 Gyr (Pass et al. 2022). The bolometric and XUV fluxes at the orbital distance of the M-Earth can then be calculated as $F_{\rm bol/XUV} = L_{\rm bol/XUV}/(4\pi a_{\rm orb}^2)$, where $a_{\rm orb}$ is the M-Earth's orbital distance, a value which we hold fixed throughout each simulation.

3.2.1 Parameterization of Atmosphere

We assume a pure water atmosphere for our model M-Earth. H_2O molecules can be broken into two H atoms and one O atom by XUV irradiation. We also adopt a planetary albedo of $A_{\rm p} = 0.3$ for all simulated M-Earths, appropriate for water-dominated atmospheres (Kopparapu et al. 2013). Given the calculated absorbed flux, we can then determine the surface temperature, $T_{\rm surf}$, assuming a step-wise relation depending on whether or not the planet is in a runaway greenhouse.

If the planet absorbs less than the runaway greenhouse limit for a pure water vapour atmosphere of $\approx$325 W/m^2 (i.e., the "water condensation insolation threshold" of Turbet et al. 2021), we simply set $T_{\rm surf} = 293.15$ K $= 20^\circ$ C. The surface temperature only affects mantle convection, and differences of tens of degrees are negligible. If the planet absorbs more than the runaway greenhouse limit, however, all surface water evaporates into a steam atmosphere, pushing the planet into a runaway greenhouse phase (Goldblatt et al. 2013; Kopparapu et al. 2013). The surface temperature thus runs away to $T_{\mathrm{surf}} = 1800$ K in our model, following Barth et al. (2021). We note that this surface temperature arises following the evaporation of 1 Earth Ocean into the atmosphere, although for 8 Earth Oceans, the value is closer to $T_{\mathrm{surf}} = 2500$ K (Turbet et al. 2019); while we do not explicitly model evaporation, this distinction may be important for future studies.

Loss to space can only occur for particles that are above the exobase, located around 500 km altitude for the Earth (Pierrehumbert 2010) — unless a hydrodynamic wind is present, which is beyond the scope of this study. Within our model, the loss of water (effectively H atoms) to space will occur in either the energy-limited or diffusion-limited regime.

3.2.2 Energy-Limited Escape

Previously, Luger & Barnes (2015) assumed that atmospheric loss to space (either energy-limited or diffusion-limited, tested separately) only occurs during the runaway greenhouse phase. We explicitly account for a steam atmosphere throughout our model. This not only improves its generality, but also allows direct calculation of the amount of water lost to space. We assume water is readily available in the atmosphere due to our relatively long timesteps compared to the short timescales for replenishment by evaporation of surface water.

During runaway greenhouse, we assume that any photodissociated oxygen will dissolve in the surface magma ocean, avoiding the build-up of a significant oxygen background often seen in atmospheric escape studies — especially Luger & Barnes

(2015) — that could hinder the escape of hydrogen to space. Because of the very high surface temperatures, we assume that the loss during runaway greenhouse is always energy-limited.

We adopt the energy-limited escape rate for a pure water atmosphere that can be broken into its constituent hydrogen and oxygen (see Watson et al. 1981, or Equation (2) of Luger & Barnes 2015):

$$\dot{M}_{\mathrm{EL}} = \frac{\epsilon_{\mathrm{XUV}} \pi F_{\mathrm{XUV}} R_{\mathrm{p}} R_{\mathrm{XUV}}^2}{G M_{\mathrm{p}} K_{\mathrm{tide}}}, \tag{3.1}$$

where F_{XUV} is the XUV flux at the orbital distance of the M-Earth, R_{p} the planetary radius, R_{XUV} the XUV deposition radius, M_{p} the mass of the planet, and ϵ_{XUV} is the XUV absorption efficiency. Although Luger & Barnes (2015) tested $\epsilon_{\mathrm{XUV}} = 0.15$–$0.3$, recent estimates for low-mass planets are closer to 0.1 (e.g., Owen & Wu 2017), while Barnes et al. (2016) tested 0.01–0.15 for Proxima Centauri b; we adopt $\epsilon_{\mathrm{XUV}} = 0.1$ for all host stars. We assume $R_{\mathrm{XUV}} = R_{\mathrm{p}}$ and $K_{\mathrm{tide}} = 1$, since it is of order unity, for simplicity. The former assumption was also made by Luger & Barnes (2015), and may lead to an underestimate of the true energy-limited escape rate (Krenn et al. 2021). However, Krenn et al. (2021) also note that $\epsilon_{\mathrm{XUV}} = 0.1$ may in fact overestimate the energy-limited escape rates; thus, our chosen parameters seem justified. Note that adopting $\epsilon_{\mathrm{XUV}} = 0.01$ would reduce the amount of water lost through energy-limited escape by an order-of-magnitude, predictably improving water retention (Lopez 2017).

3.2.3 Diffusion-Limited Escape

We adopt the diffusion-limited escape parameterization of Luger & Barnes (2015), specifically their Equation (13) (see also Walker 1977, pg. 164). The diffusion-limited escape mass flux of hydrogen atoms is:

$$\dot{M}_{\rm DL} = m_{\rm H} \pi R_{\rm p}^2 \frac{bg(m_{\rm O} - m_{\rm H})}{k_{\rm B} T_{\rm therm}(1 + X_{\rm O}/X_{\rm H})}. \tag{3.2}$$

Here, $m_{\rm H}$ and $m_{\rm O}$ are the atomic masses of hydrogen and oxygen, respectively, $b = 4.8 \times 10^{17} (T_{\rm therm})^{0.75}$ cm^{-1} s^{-1} is the binary diffusion coefficient for hydrogen and oxygen, and $X_{\rm O}/X_{\rm H} = 1/2$ presumes two hydrogen atoms for every one oxygen atom when water is photodissociated. This assumes that when two hydrogen atoms escape, the corresponding single oxygen atom either escapes as well, or is sequestered through reaction with the solid or molten surface, so that oxygen does not build up in the atmosphere. Finally, we assume a constant thermospheric temperature of $T_{\rm therm} = 400$ K, as did Luger & Barnes (2015).

3.3 Magma Oceans & Deep-Water Cycling

Moore & Cowan (2020) presented a coupled water cycling and loss model with a seafloor-pressure-dependent degassing rate and a mantle-temperature-dependent regassing rate based on Komacek & Abbot (2016). We improve that model by accounting for more dependencies in degassing and regassing. First, however, we will outline the thermal evolution during the surface magma ocean and deep-water cycling phases.

3.3.1 Thermal Evolution Equations

The surface magma ocean (MO) solidifies from the bottom–up. Due to uncertainties in the timing of magma ocean solidification, especially for planets around M-dwarfs with extended runaway greenhouse phases, we parameterize the surface magma ocean thickness at time t as a function of the MO solidification timescale, τ_{MO}:

$$d_{\mathrm{MO}}(t) = \beta_{\mathrm{MO}} d_{\mathrm{MO},0} \left[\exp\left(\frac{-t}{\tau_{\mathrm{MO}}} + 1 \right) - 1 \right]. \tag{3.3}$$

Here, $\beta_{\mathrm{MO}} = 1/(\exp(1) - 1) \approx 0.582$, and $d_{\mathrm{MO},0}$ is the initial MO depth, from surface to core. Since surface magma ocean and runaway greenhouse phases are concurrent, throughout this work we set $\tau_{\mathrm{MO}} = \tau_{\mathrm{RG}}$ (see Table 3.1) for each host star/orbital distance combination.

The depth of the surface magma ocean decreases as it solidifies from the bottom–up; at time t, the bottom of the MO will be located at radius $r(t) = R_{\mathrm{p}} - d_{\mathrm{MO}}(t)$. We assume the core heat flux is negligible. We use Equation (1) of Elkins-Tanton (2008) to estimate the solidus temperature, based on experimental data of Earth, to determine the MO temperature for a given $r(t)$:

$$T_{\mathrm{MO}}(r) = -1.16 \times 10^{-7} r^3 + 0.0014 r^2 - 6.382 r + 1.444 \times 10^4. \tag{3.4}$$

We adopt a timestep during MO of $\mathrm{d}t_{\mathrm{MO}} = \tau_{\mathrm{step,MO}} = 2000$ yr due to the comparatively short duration of the surface magma ocean/runaway greenhouse phase compared to the 5 Gyr simulation. Once the surface magma ocean solidifies, the mantle begins solid-state convection, initiating plate tectonics and the deep-water cycle on the M-Earth, and we adopt a longer timestep of $\mathrm{d}t = \tau_{\mathrm{step}} = 20,000$ yr for the remainder of the simulation.

The mantle temperature during deep-water cycling is calculated following Moore & Cowan (2020), now assuming an initial average mantle temperature of $T_{\mathrm{m},0} = 3000$ K following surface magma ocean solidification. We improve the radionuclide heating rate, $Q(t)$, using the equation from Schaefer & Sasselov (2015):

$$Q(t) = \rho_{\mathrm{m}} \sum C_{\mathrm{i}} H_{\mathrm{i}} \exp\left[\lambda_{\mathrm{i}}\left(4.6 \times 10^9 - t\right)\right]. \tag{3.5}$$

Here, ρ_{m} is the mantle density. We assume nominal bulk silicate Earth (i.e., ~21 ppb U contained in the primitive mantle; McDonough & Sun 1995). We use the same values as Schaefer & Sasselov (2015), taken from Schubert et al. (2001), for element concentration by mass, C_{i}, heat production per unit mass, H_{i}, and decay constants, λ_{i}, for ^{238}U, ^{235}U, ^{40}K, and ^{232}Th. We again assume the core heat flux is negligible.

3.3.2 Surface Magma Ocean Water Partitioning

An M-Earth orbiting within the habitable zone of its host star begins in a surface magma ocean (MO) phase, concurrent with a runaway greenhouse, before surface solidification partitions water between distinct surface and mantle reservoirs. Magma ocean dynamics are significantly different than solid mantle dynamics (e.g., Elkins-Tanton 2008; Hamano et al. 2013; Ikoma et al. 2018). We thus begin our M-Earth simulations with a separate parameterization for MO water partitioning. There are three distinct reservoirs for water during this earliest stage of M-Earth evolution: the steam atmosphere, the surface magma ocean (which shrinks over time), and the solidifying mantle (which grows over time). A box model representation of the surface magma ocean stage is shown in Fig. 3.1(a).

Our surface magma ocean approximation assumes bottom–up solidification, typical of many magma ocean studies (e.g., Elkins-Tanton 2008, Hamano et al. 2013, Lebrun et al. 2013, Schaefer et al. 2016). Water is exsolved into a steam atmosphere once the magma ocean becomes saturated. This canonical bottom–up solidification occurs through fractional crystallization and settling, which leads to a growing solid mantle underlying the shrinking MO. This geologically rapid process usually leads to MO solidification in tens of Myr, but may be extended by an insulating steam atmosphere or high bolometric stellar flux. We posit that the magma ocean lasts as long as the runaway greenhouse: $\tau_{\mathrm{MO}} = \tau_{\mathrm{RG}}$. The hot runaway greenhouse temperatures will maintain a molten surface, while the end of runaway greenhouse and the corresponding decrease in surface temperature will permit surface solidification.

We assume that the surface magma ocean is composed of olivine and pyroxenes; these nominally anhydrous silicates have solid-melt water partition coefficients of $D = 0.002$ and 0.02, respectively, and saturate at 800–1500 ppm (0.08–0.15 wt.%, depending on mantle composition) of water (see Table 1S of Elkins-Tanton 2008). In their magma ocean model, Hamano et al. (2013) assume a water partition coefficient of $D = 0.0001$. Katz et al. (2003) adopt $D = 0.01$, due to its similar behaviour to cerium, for their upper mantle melting parameterization. Although the partition coefficient is pressure-dependent and will change with depth as the MO solidifies upwards, we adopt a constant solid-liquid partition coefficient for water of $D = 0.001$, intermediate between the values of Katz et al. (2003) and Hamano et al. (2013), since our surface magma ocean is assumed to solidify beginning from the core-mantle boundary at much higher pressures than would be present in the upper mantle.

We adopt an upper limit on solid mantle water capacity of 12 Earth Oceans (Cowan & Abbot 2014), corresponding to ∼3458 ppm. We vary the surface magma ocean water saturation limit from 0.1 wt.%, or $C_{\mathrm{sat}} = 0.001$, to 10 wt.% (Elkins-Tanton 2008) or $C_{\mathrm{sat}} = 0.1$. Decreasing C_{sat} leads to earlier degassing of an atmosphere during the MO phase; beginning with a water inventory larger than the saturation limit will cause an atmosphere to be degassed immediately, resulting in atmospheric loss throughout the surface magma ocean period.

We assume that, for initial water inventories below C_{sat}, all water is initially dissolved within the surface magma ocean with no overlying atmosphere. In reality there would always be some partial pressure of water in the atmosphere in equilibrium with the molten surface (e.g., Elkins-Tanton 2008, Hamano et al. 2013), but the mass of that atmosphere would be dwarfed by the water dissolved in the MO. We bracket this behaviour by testing three values of C_{sat}, which changes the timing of the onset of atmospheric degassing.

For high enough C_{sat}, due to the large extent of the MO, the initially dissolved water content is far below the saturation limit. As the MO cools and solidifies, the magma becomes more enriched in water; once C_{sat} is exceeded, a steam atmosphere is degassed, from which water may then be lost to space. We assume the entire mantle to be initially molten (see Eqn. 3.3). As the MO solidifies, water is partitioned between solid mantle and silicate melt according to our adopted $D = 0.001$. Using a value of $C_{\mathrm{sat}} = 0.001$, smaller than the MO concentration of all tested initial water inventories, captures the ongoing degassing of a potentially substantial atmosphere for the entirety of the surface magma ocean, providing a better comparison with simulations that directly calculate the partial pressure of atmospheric water during that stage.

During the surface magma ocean phase, we use a simple analytical model following Boukaré et al. (2019) to track the amount of water in the three reservoirs — solid mantle, magma ocean, and steam atmosphere — as a function of the radius of the bottom of the MO, $r(t)$. Throughout the surface magma ocean phase, we assume a constant density for the silicate melt $\rho = 3000$ kg/m^3 for mass balance purposes, although we note that the solid mantle will have a slightly higher density of $\rho_\mathrm{m} = 3300$ kg/m^3.

The partitioning model used in this study is based on mass conservation written in an integral form (see Boukaré et al. 2019). The concentration of water in the solid phase, $C_\mathrm{s}(r)$, is governed by

$$C_\mathrm{s}(r) = DC_\mathrm{l}(r), \tag{3.6}$$

where $D = 0.001$ is the solid-liquid partition coefficient for water, and $C_\mathrm{l}(r)$ the concentration of water in the liquid phase of the melt.

While the MO is unsaturated, mass balance allows us to determine $C_\mathrm{l}(r)$ using R_p, the core radius, R_c, and D:

$$C_\mathrm{l}(r) = C_0 \left(\frac{R_\mathrm{p}^3 - R_\mathrm{c}^3}{R_\mathrm{p}^3 - r^3} \right)^{1-D}. \tag{3.7}$$

Here, C_0 corresponds to the initial concentration of water within the MO, which we vary to account for different amounts of planetary water inventory from planet formation. Water delivery to terrestrial planets is an ongoing debate (e.g., O'Brien et al. 2018). We assume that no more water is accreted by the planet during or after MO solidification. The above equation can also be rearranged to determine the radius at which the MO will be saturated,

$$R_\mathrm{sat} = \left(R_\mathrm{p}^3 - \frac{R_\mathrm{p}^3 - R_\mathrm{c}^3}{\left(\frac{C_\mathrm{sat}}{C_0}\right)^{\frac{1}{1-D}}} \right)^{1/3}, \tag{3.8}$$

where C_sat is the water saturation limit of the surface magma ocean.

The mass of water in each reservoir (magma ocean, MO; solid mantle, SM; and atmosphere, atm) can then be determined at each radial extent $r(t)$ for a given time. While the mantle is unsaturated ($r \leq R_{\rm sat}$) we have:

$$M_{\rm MO}^{\rm uns}(r) = C_{\rm l}(r)\frac{4\pi}{3}\rho\left(R_{\rm p}^3 - r^3\right), \tag{3.9}$$

$$\begin{aligned} M_{\rm SM}^{\rm uns}(r) &= C_0\frac{4\pi}{3}\rho\left(R_{\rm p}^3 - R_{\rm c}^3\right)^{1-D}\left[\left(R_{\rm p}^3 - R_{\rm c}^3\right)^D - \left(R_{\rm p}^3 - r^3\right)^D\right] \\ &= M_{\rm init} - M_{\rm MO}^{\rm uns}(r), \end{aligned} \tag{3.10}$$

$$M_{\rm atm}^{\rm uns}(r) = 0. \tag{3.11}$$

Once the surface magma ocean saturates (i.e., $r > R_{\rm sat}$), water is degassed into the atmosphere. The mass of water in each reservoir following MO saturation is:

$$M_{\rm MO}^{\rm sat}(r) = C_{\rm sat}\frac{4\pi}{3}\rho\left(R_{\rm p}^3 - r^3\right), \tag{3.12}$$

$$M_{\rm SM}^{\rm sat}(r) = M_{\rm SM}^{\rm uns}(R_{\rm sat}) + DC_{\rm sat}\frac{4\pi}{3}\rho\left(r^3 - R_{\rm sat}^3\right), \tag{3.13}$$

$$M_{\rm atm}^{\rm sat}(r) = M_{\rm tot} - M_{\rm SM}^{\rm sat}(r) - M_{\rm MO}^{\rm sat}(r) - \min\left[\dot{M}_{\rm EL}, \frac{M_{\rm atm}}{\tau_{\rm step,MO}}\right], \tag{3.14}$$

where $M_{\rm tot}(t)$ is the total water remaining in the system, accounting for all water that has been lost to space at either the energy-limited rate (due to the runaway greenhouse temperatures) or the entire atmospheric water content in a given timestep. Initially $M_{\rm tot} = M_{\rm init}$, where,

$$M_{\rm init} = C_0\frac{4\pi}{3}\rho\left(R_{\rm p}^3 - R_{\rm c}^3\right). \tag{3.15}$$

Since we treat the initial amount of water on the M-Earth, $M_{\rm init} = W_{{\rm MO},i}$, as a free parameter, we can rearrange Eqn. 3.15 to determine C_0 for a given simulation. In cases where $C_0 > C_{\rm sat}$, we include an additional first step: the water corresponding to $C_{\rm sat}$ is placed in the surface magma ocean, while the excess is immediately degassed into a steam atmosphere. This scenario captures atmospheric degassing and loss throughout the lifetime of the surface magma ocean.

3.3.3 Coupled Cycling & Loss Equations: Model Without a Basal Magma Ocean (Sans BMO)

Once the planet leaves the runaway greenhouse and the surface solidifies, it begins deep-water cycling; the corresponding box model is shown in Fig. 3.1(b). As an improvement to Komacek & Abbot (2016) and Moore & Cowan (2020), we incorporate seafloor-pressure, P, and mantle-temperature, $T_{\rm m}$, dependence into both the degassing and regassing rate. Due to our relatively long timesteps ($\tau_{\rm step} = 20,000$ yr), we assume that surface water is readily available to vertically diffuse and replenish any water lost to space from the upper atmosphere during a timestep; hence, the atmospheric reservoir is essentially a subset of the surface reservoir in our model.

The degassing rate, $w_{\uparrow}$, is given by,

$$w_{\uparrow}(P, T_{\rm m}) = x\rho_{\rm m} d_{\rm melt} f_{\rm degas}(P) f_{\rm melt}(T_{\rm m}), \tag{3.16}$$

where the pressure dependence is contained in the melt degassing efficiency, $f_{\rm degas}(P)$:

$$f_{\rm degas}(P) = \min\left[f_{\rm degas,\oplus}\left(\frac{P}{P_{\oplus}}\right)^{-\mu},\ 1\right], \tag{3.17}$$

and the temperature dependence is within the melt fraction, $f_{\rm melt}(T_{\rm m})$:

$$f_{\rm melt}(T_{\rm m}) = \left(\frac{T_{\rm m} - (T_{\rm sol,dry} - Kx^{\gamma})}{T_{\rm liq,dry} - T_{\rm sol,dry}}\right)^{\theta}. \tag{3.18}$$

The rest of the above variables are as follows: x is the mantle water mass fraction,

$\rho_{\rm m}$ is the upper mantle density, $d_{\rm melt}$ is the mid-ocean ridge melting depth, P is the seafloor pressure, $P_\oplus = 4 \times 10^7$ Pa is the seafloor pressure for Earth, $T_{\rm m}$ is the average mantle temperature, $T_{\rm sol,dry}$ is the dry solidus temperature of the mantle, K and γ are empirically determined constants for solidus depression of a wet mantle (Katz et al. 2003), θ is an empirically determined exponent (Schaefer & Sasselov 2015), and $T_{\rm liq,dry}$ is the dry liquidus temperature of the mantle.

Note that degassing will occur throughout the deep-water cycling simulation provided there is sufficient water in the mantle and the mantle does not cool below the solidus. We nominally set the exponent $\mu = 1$, following Cowan & Abbot (2014) and Komacek & Abbot (2016).

In the other cycling direction, the regassing rate includes $T_{\rm m}$-dependent partial melting and P-dependent water solubility within the melt, both of which are incorporated into the hydrated layer depth, $d_{\rm h}(P, T_{\rm m})$. The regassing rate, $w_\downarrow$, is given by

$$w_\downarrow(P, T_{\rm m}) = x_{\rm h} \rho_{\rm c} \chi_{\rm r} d_{\rm h}(P, T_{\rm m}), \tag{3.19}$$

where the hydrated layer depth, $d_{\rm h}(P, T_{\rm m})$, is,

$$\begin{aligned} d_{\rm h}(P, T_{\rm m}) = \min\Bigg[& h^{(1-3\beta)} (T_{\rm m} - T_{\rm surf})^{-(1+\beta)} (T_{\rm serp} - T_{\rm surf}) \\ & \times \left(\frac{\eta(T_{\rm m}, x) \kappa {\rm Ra}_{\rm crit}}{\alpha \rho_{\rm m} g} \right)^{\beta} \left(\frac{P}{P_\oplus} \right)^{\sigma},\ d_{\rm b} \Bigg]. \end{aligned} \tag{3.20}$$

The regassing-related variables are as follows: $x_{\rm h}$ is the water mass fraction in the hydrated crust, $\rho_{\rm c}$ is the density of the crust, $\chi_{\rm r}$ is the regassing/subduction efficiency, h is the mantle thickness (calculated using the relations of Valencia et al. 2006 for a 1 $M_\oplus$ terrestrial planet), $\beta = 0.3$ is an empirically determined constant (McGovern & Schubert 1989), $T_{\rm serp}$ is the serpentinization stability temperature, $\eta(T_{\rm m}, x)$ is the mantle viscosity, κ is the mantle thermal diffusivity, $\mathrm{Ra}_{\mathrm{crit}} = 1100$ is the critical Rayleigh number for mantle convection, α is the mantle characteristic thermal expansivity, g is the surface gravity, and d_{b} is the thickness of the basaltic crust.

We also nominally set $\sigma = 1$ (Cowan & Abbot 2014; Komacek & Abbot 2016). For consistency with Moore & Cowan (2020), we include the hydrated layer check from Schaefer & Sasselov (2015) to ensure the hydrated layer does not contain more water than is present on the surface. Many of the aforementioned deep-water cycling variables can be found in Table C1 of Moore & Cowan (2020).

Combining the equations for degassing, regassing, and loss to space, we can define the evolution of mantle water, W_{m}, and surface water, W_{s}, over time during the plate-tectonics-driven deep-water cycling of Fig. 3.1(b). The change in mantle and surface water inventories over time are,

$$\frac{\mathrm{d}W_{\mathrm{m}}}{\mathrm{d}t} = w_{\downarrow} - w_{\uparrow}, \tag{3.21}$$

and

$$\frac{\mathrm{d}W_{\mathrm{s}}}{\mathrm{d}t} = w_{\uparrow} - w_{\downarrow} - \min\left[\dot{M}_{\mathrm{DL}}, \dot{M}_{\mathrm{EL}}, \frac{W_{\mathrm{s}}}{\tau_{\mathrm{step}}}\right]. \tag{3.22}$$

The amount of water lost to space is either the minimum of the energy-limited or diffusion-limited escape rates during a timestep or the total available surface water during that timestep, as the upper atmosphere water replenishment times are very short compared to τ_{step}. For the majority of our simulations, once the surface has solidified, the loss to space is diffusion-limited. Depending on the combination of host star and orbital distance, however, it is possible for the loss to again become energy-limited late in the simulation (see, e.g., Fig. 3.2).

Following Moore & Cowan (2020), we make important checks at each timestep. If the mantle temperature cools below the solidus, melt will no longer be present in the boundary layer, and degassing stops, $w_{\uparrow} = 0$; this is less of an issue for the shorter $t = 5$ Gyr simulations within the current study. We also set the minimum water in the mantle to be the same as the desiccation limit for the surface, $W_{\mathrm{m,min}} \approx 10^{-5}$ Earth Oceans, to avoid mantle viscosity going to infinity.

3.3.4 Coupled Cycling & Loss Equations: Basal Magma Ocean Model

Following the surface magma ocean phase and surface solidification, a residual basal magma ocean (BMO) may persist below the solid mantle (Labrosse et al. 2007). As the BMO solidifies, it will slowly inject water into the overlying mantle. A box model representation of a BMO within an M-Earth during deep-water cycling is shown in Fig. 3.1(c). The general idea behind this box model is that a substantial molten reservoir — within which water is highly soluble — may exist below the relatively dry mantle following surface magma ocean solidification, and the slow incorporation of this water into the mantle should prevent mantle desiccation.

The two key parameters governing the magma ocean in our model are its extent, which determines water storage, and the solidification timescale. To roughly mimic the behaviour of a BMO, we run our MO simulations using an exceedingly high $D = 0.2$ to account for water stored in both the solid mantle and in the BMO; this higher D will result in a significant portion of the water locked into the planetary interior at the end of the MO phase. Once the MO solidifies, the mantle contains the same small amount as the corresponding $D = 0.001$ MO simulation, while the remainder — and the lion's share — is attributed to the BMO.

Following surface magma ocean solidification, the cycling equation for the surface remains unchanged, while the solid mantle equation now accounts for a slow but constant injection of water until the basal magma ocean solidifies at $t = \tau_{\mathrm{BMO}}$:

$$\frac{\mathrm{d}W_{\mathrm{m}}}{\mathrm{d}t} = w_{\downarrow} - w_{\uparrow} + \left(\frac{W_{\mathrm{BMO,i}}}{\tau_{\mathrm{BMO}} - \tau_{\mathrm{MO}}}\right), \tag{3.23}$$

where $W_{\mathrm{BMO,i}}$ is the initial amount of water in the basal magma ocean at the time of surface solidification. Since a basal magma ocean cools on the order of Gyrs (Labrosse et al. 2007; Blanc et al. 2020), we adopt $\tau_{\mathrm{BMO}} = 1$, 2, or 3 Gyr.

There are two potential evolutionary pathways for each simulated M-Earth, illustrated in Fig. 3.1: either our sans basal magma ocean simulations (left), or simulations incorporating a basal magma ocean (right), which solidifies to the deep-water cycling box model.

3.3.5 Model Inputs

The M stellar type spans a wide range of masses and radii. To bracket the potential impact of different host stars on the water evolution of an orbiting M-Earth, we test three host M-dwarf stars using the stellar tracks of Baraffe et al. (2015): a Proxima Centauri-like M5 ($0.13M_{\odot}$), a smaller M8 ($0.09M_{\odot}$), and a larger M1 ($0.50M_{\odot}$). We test three fixed orbital distances within the habitable zone (HZ) of each host star, calculated at $t = 4.5$ Gyr using the HZ calculator of Kopparapu et al. (2013). We can then calculate the duration of runaway greenhouse at this fixed orbital distance for

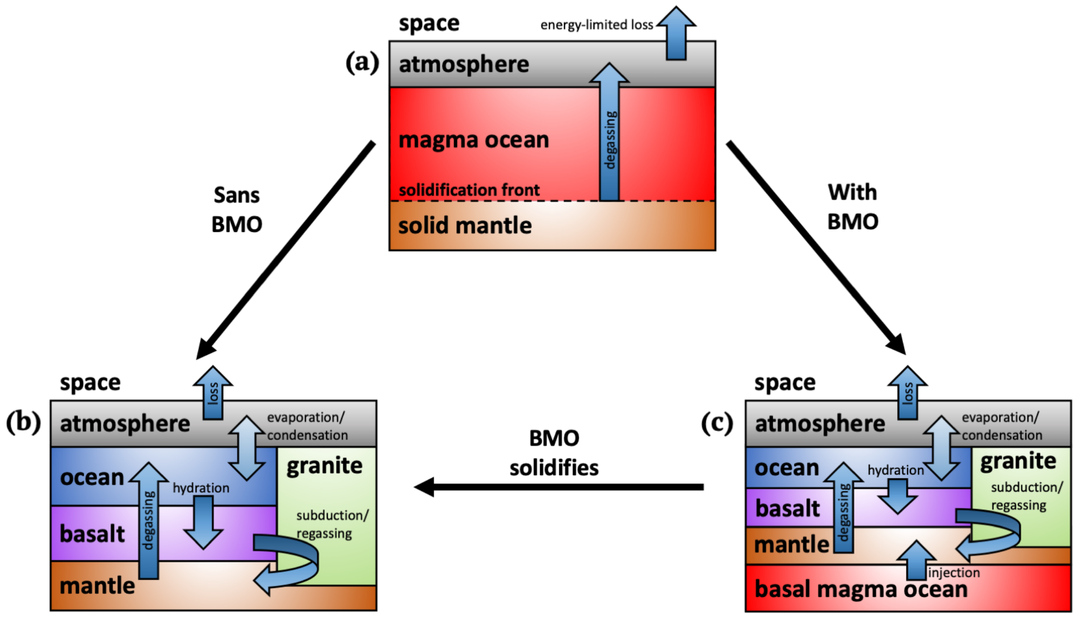

Figure 3.1: Flowchart illustrating the three possible stages in our box model of M-Earth evolution. (a) Surface magma ocean (MO). We assume bottom–up solidification of the MO lasting as long as the runaway greenhouse ($\tau_{\rm MO} = \tau_{\rm RG}$). As it solidifies from the bottom–up, the magma ocean eventually becomes saturated with water, and excess water is degassed into a steam atmosphere, from which it may be lost to space through energy-limited escape. (b) Plate-tectonics-driven deep-water cycling including a pure water vapour atmosphere. Water is photodissociated into hydrogen and oxygen high in the atmosphere. Hydrogen may then be lost to space. Water is degassed from mantle to surface through mid-ocean ridge volcanism and regassed from the surface to the mantle through subduction of hydrated oceanic crust. (c) Water cycling in the presence of a basal magma ocean (BMO). After MO solidification, a residual BMO remains below the solid mantle (Labrosse et al. 2007). While the BMO is present, water may be degassed/regassed, following our deep-water cycling parameterization, or lost to space. Additionally, water is slowly injected into the solid mantle at a constant rate until the BMO completely solidifies. Once the basal magma ocean solidifies at $\tau_{\rm BMO}$, the M-Earth evolves from the basal magma ocean model to the deep-water cycling model for the remainder of the simulation. Hence, the two evolutionary pathways are (a)-(b) and (a)-(c)-(b).

each combination of host star and location within HZ, to be adopted as the duration of the surface magma ocean, i.e., $\tau_{\rm MO} = \tau_{\rm RG}$; these values can be found in Table 3.1. For simplicity in our comparisons, we neglect the difference in runaway greenhouse length when varying the atmospheric water content, although we note that complete desiccation of the planet would end the runaway greenhouse.

Recall that we offset the stellar tracks of Baraffe et al. (2015) by 5 Myr to account for planet formation. For simplicity, throughout this work we assume a constant planetary albedo for all simulated M-Earths of $A_{\rm p} = 0.3$ motivated by Earth's present-day albedo, a parameter also assumed constant in the magma ocean simulations of Hamano et al. (2013). This albedo is intermediate between that of a water-covered surface, $A_{\rm p} = 0.05$–0.1 (Peixoto & Oort 1992) and the albedo of the "steam atmosphere" of Venus, $A_{\rm p} = 0.75$ (Schaefer et al. 2016; Barth et al. 2021); hence, assuming $A_{\rm p} = 0.3$ may overestimate the absorbed radiation during runaway greenhouse.

Predictions for water inventories of terrestrial exoplanets vary wildly (e.g., Raymond et al. 2004, 2007; Lissauer 2007; O'Brien et al. 2018; Lichtenberg et al. 2019; Kimura & Ikoma 2022). Earth's oceans contain $\sim 1.4 \times 10^{21}$ kg $\equiv$ 1 Earth Ocean of water, and the mantle's capacity may be up to 12 Earth Oceans (Bercovici & Karato 2003; Hirschmann 2006; Cowan & Abbot 2014; Guimond et al. 2023). The water capacity of a planetary mantle will depend on its mineralogy/composition, oxygen fugacity, and planetary mass. Shah et al. (2021) determined constraints on the internal storage of water in terrestrial planets, estimated to be 0–6 wt.% (0 to $\sim$250 Earth Oceans). Recently, Barth et al. (2021) found that for initial water inventories ranging from 1–100 Earth Oceans, only 3–5% (0.03–5 Earth Oceans) will be sequestered within the mantle of TRAPPIST-1e, 1f, and 1g after surface magma ocean solidification.

We test a range of initial water inventories, surface magma ocean water saturation limits, and basal magma ocean lifetimes. We explore the parameter space in Table 3.2 for the first 5 Gyr of an M-Earth's lifetime. We test water inventories from $M_{\mathrm{init}} =$ 2 to 400 Earth Oceans (initially completely dissolved in the surface magma ocean if possible; otherwise, the excess above saturation is immediately degassed), three surface magma ocean water saturation limits — $C_{\mathrm{sat}} = 0.001$, 0.01, and 0.1 — and three basal magma ocean lifetimes of $\tau_{\mathrm{BMO}} = 1$, 2, and 3 Gyr.

Recall that for each simulation, we set $\tau_{\mathrm{MO}} = \tau_{\mathrm{RG}}$; we avoid explicitly modelling the feedback between water degassing into a (potentially) runaway greenhouse atmosphere and surface magma ocean solidification. Variation in τ_{RG}, and hence τ_{MO}, is achieved through the combination of host star and orbital distance (see Table 3.1). Our surface magma ocean solidification timescales roughly correspond to the range found by Schaefer et al. (2016) (their Fig. 5, for the highly-irradiated GJ 1132b) and Barth et al. (2021) (their Fig. 2), while Hamano et al. (2013) note that planets with comparable water budgets to the modern Earth require a few Myr to 100 Myr for surface magma ocean solidification.

Stellar Type	Stellar Mass	Location Within Habitable Zone (HZ)	Orbital Distance	Runaway Greenhouse (RG) Duration, τ_{RG}	Maximum Water Loss [Earth Oceans]			
					EL during RG	DL rest of sim	Total	Max, EL only
M8	$0.09M_{\odot}$	Hot, Inner Edge	0.025 AU	335 Myr (0.335 Gyr)	7.72	2.82	10.5	19.7
		Middle (Mid)	0.037 AU	110 Myr (0.110 Gyr)	2.18	2.95	5.13	8.64
		Cold, Outer Edge	0.050 AU	48.2 Myr (0.048 Gyr)	0.833	2.99	3.83	4.83
M5	$0.13M_{\odot}$	Inner	0.045 AU	155 Myr (0.155 Gyr)	2.92	2.92	5.85	15.8
		Mid	0.067 AU	44.5 Myr (0.044 Gyr)	0.713	2.99	3.71	7.09
		Outer	0.089 AU	17.5 Myr (0.018 Gyr)	0.235	3.01	3.25	4.01
M1	$0.50M_{\odot}$	Inner	0.196 AU	33.8 Myr (0.034 Gyr)	0.475	3.00	3.50	13.8
		Mid	0.286 AU	6.59 Myr (0.0066 Gyr)	0.074	3.02	3.09	6.47
		Outer	0.377 AU	0.36 Myr (0.00036 Gyr)	0.003	3.02	3.02	3.73

Table 3.1: Host star spectral classification and mass used in our simulations, from stellar evolution tracks of Baraffe et al. (2015). The corresponding location within the habitable zone (HZ) and orbital distance around each star is calculated at $t = 4.5$ Gyr using the HZ calculator of Kopparapu et al. (2013). We compute the runaway greenhouse (RG) duration from the time-dependent irradiation, assuming a constant planetary albedo of $A_{\text{p}} = 0.3$. The potential water loss in different regimes is included in the next columns: energy-limited (EL) loss assuming an efficiency of $\epsilon_{\text{XUV}} = 0.1$ during RG, diffusion-limited (DL) loss following the end of RG, and the combined total potential water loss. The final column shows the maximum potential water loss if energy-limited for the entire simulation; due to our parameterization, the maximum water loss when diffusion-limited for the entire simulation is always 3.02 Earth Oceans. Potential water loss is expressed in units of Earth Oceans, $\approx 1.4 \times 10^{21}$ kg. Depending on the details of atmospheric loss, M-Earths can lose 3–20 Earth Ocean of water after 5 Gyr. Note that reducing ϵ_{XUV} by an order-of-magnitude, from 0.1 to 0.01 (Lopez 2017), would also reduce the amount of water lost through energy-limited escape by an order-of-magnitude.

Name	Parameter	Values Tested
Total initial water mass	M_{init} [Earth Oceans]	**2, 4, 6, 8**, 12, 16, 20, 24, 50, 100, 200, 400
Surface magma ocean (MO) saturation limit	C_{sat}	0.001, **0.01**, 0.1
Basal magma ocean (BMO) solidification timescale	τ_{BMO} [Gyr]	1, **2**, 3
Orbital distance/location within HZ	a_{orb}	**Inner HZ, Mid HZ, Outer HZ**
Host stellar type	—	**M8, M5, M1**
Water loss prescription	—	$\dot{M}_{\text{EL}}$ **during MO,** min $\left[\dot{M}_{\text{DL}}, \dot{M}_{\text{EL}}\right]$ **otherwise**; $\dot{M}_{\text{EL}}$ throughout

Table 3.2: Parameters explored in this study. Water mass is expressed in units of Earth Oceans, $\approx 1.4 \times 10^{21}$ kg, while the value of a_{orb} varies depending on the combination of host star and location within the habitable zone. Bold values indicate our nominal parameter space.

3.4 Results: Coupled Magma Oceans & Deep-Water Cycling

3.4.1 Temporal Fluxes & Expected Water Loss

Our chosen stellar hosts, locations within the habitable zone, and orbital distances are listed in Table 3.1. Further, we report the duration of the runaway greenhouse (RG) based on absorbed flux, which will later be used as the surface magma ocean duration ($\tau_{\rm MO} = \tau_{\rm RG}$). We calculate the maximum water that could be lost using the most likely scenario of energy-limited loss during RG and diffusion-limited loss otherwise, along with the maximum if energy-limited loss occurs for the entirety of each simulation. An M-Earth orbiting at the inner edge of the habitable zone loses much more water through energy-limited loss during runaway greenhouse than the rest of the simulation; conversely, at the outer edge of the habitable zone, more water is lost during the long diffusion-limited stage than during the brief runaway greenhouse phase.

Fig. 3.2 shows the evolution of radiative fluxes, surface temperature, and atmospheric loss rate for an Earth-like planet orbiting at the outer edge of the habitable zone (Outer HZ) of an M8 host star. The runaway greenhouse phase is shaded grey. Once the absorbed flux falls below the runaway greenhouse limit of 325 W/m^2 (Turbet et al. 2021), the surface temperature decreases from the runaway greenhouse limit of $T_{\rm surf} = 1800$ K to a temperate $T_{\rm surf} = 293.15$ K. The evolution of the rate of loss to space is clear in the lower right panel: during runaway greenhouse, the loss to space is energy-limited, before switching to diffusion-limited when the runaway greenhouse ends, and once again becoming energy-limited (the lower of the two escape rates) near the end of the simulation.

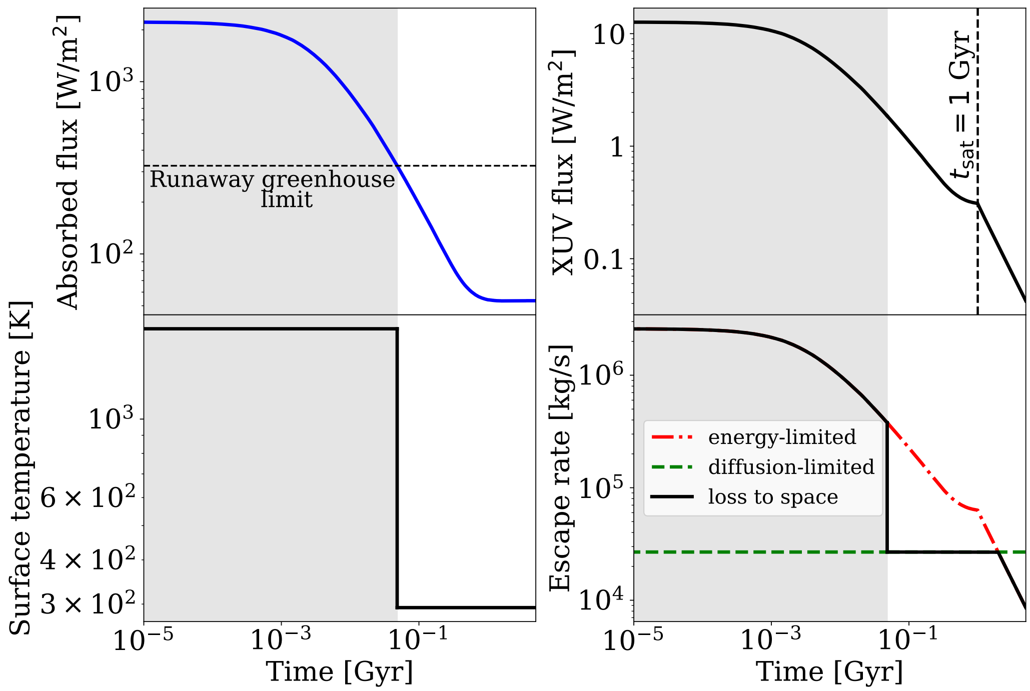

Figure 3.2: Evolution of the absorbed flux assuming a constant $A_\mathrm{p} = 0.3$ (top left), surface temperature (bottom left), X-ray and extreme ultraviolet flux (top right), and atmospheric escape rate (bottom right). This figure corresponds to an Earth-like planet orbiting at the outer edge of the habitable zone of an M8 host star. During the runaway greenhouse phase (shaded grey), loss to space is energy-limited with an efficiency of $\epsilon_\mathrm{XUV} = 0.1$, and T_surf is held constant at 1800 K. Once the M-Earth exits the runaway greenhouse, loss to space becomes diffusion-limited, and T_surf is fixed at 293.15 K. The loss again becomes energy-limited (i.e., the lower of diffusion- and energy-limited) near the end of the simulation. The cusp in F_XUV and the energy-limited escape rate corresponds to our adopted stellar XUV saturation timescale of $t_\mathrm{sat} = 1$ Gyr. Although loss rates are much greater during runaway greenhouse, the integrated loss for many planets is dominated by diffusion-limited loss during post-runaway greenhouse, especially for higher magma saturation limits C_sat which leads to later degassing of an atmosphere.

3.4.2 Water Evolution on Specific Planets

We present in Fig. 3.3 a representative example of the temporal evolution of water inventories for the first 5 Gyrs of an Earth-like planet orbiting an M8 host star at the Inner HZ with an initial water inventory of 6 Earth Oceans; this figure includes simulations without and with a basal magma ocean for various basal magma ocean lifetimes. The left part of the figure (grey area, and plotted on a reverse-log scale) corresponds to the concurrent surface magma ocean/runaway greenhouse phase, while the right part (white area) corresponds to the longer deep-water cycling phase.

In the sans basal magma ocean simulation (top of Fig. 3.3), an atmosphere is degassed during the surface magma ocean (MO) phase once the shrinking MO reaches saturation. Water is then lost from the atmosphere at the energy-limited rate. By τ_{MO}, the time of surface solidification, $\sim$1 Earth Ocean has been lost to space; most of the remaining $\sim$5 Earth Oceans ends up in the surface/atmosphere reservoir. A small amount of water remains in the solid mantle throughout the simulation, governed by our water partition coefficient $D = 0.001$. Water is lost at the diffusion-limited rate following surface solidification, and the M-Earth ends the 5 Gyr simulation in a habitable regime with $\sim$2 Earth Oceans of surface water. Note that following surface solidification, water loss to space remains diffusion-limited for the rest of the simulation, as opposed to the brief switch back to energy-limited shown in Fig. 3.2

A basal magma ocean (BMO) does not significantly alter the habitability prospects of this M-Earth (bottom three panels of Fig. 3.3) regardless of BMO lifetime, τ_{BMO}. Following MO solidification and the energy-limited loss of $\sim$0.8 Earth Oceans to space, only $\sim$2.8 Earth Oceans of water has been degassed into the atmosphere, while $\sim$2.4

Earth Oceans remain locked within the BMO. Water is injected into the overlying solid mantle by the slowly solidifying BMO at a constant rate governed by τ_{BMO}. Although the total final water inventory is the same for all basal magma ocean simulations in Fig. 3.3, the temporal evolution and final partitioning of water between reservoirs differs.

A shorter τ_{BMO} leads to injection of water into a still relatively hot mantle, which permits the surface inventory to increase, even in the face of energy-limited loss, until the basal magma ocean disappears. Increasing τ_{BMO} leads to slower water injection into a cooler mantle which does not release the water to the surface; as a result, mantle water inventory increases with increasing BMO lifetime. Indeed, the shortest τ_{BMO} leads to substantial surface water and some mantle water, while the longest τ_{BMO} results in $\sim$50% more water sequestered within the mantle than is present on the surface.

Regardless of whether a basal magma ocean is included in the simulation, by 5 Gyr this particular M-Earth is in a habitable regime with $\sim$1–2 Earth Oceans on its surface. This is all the more impressive because the planet was expected to lose 10.5 Earth Oceans (Table 3.1). Fig. 3.3 therefore demonstrates the ability of a long-lived magma ocean, along with a deep-water cycle, to maintain the habitability of an M-Earth in the face of predicted significant loss to space based solely on stellar evolution.

Although these simulations present a clear benefit of a coupled magma ocean and deep-water cycle, the basal magma ocean itself does not seem to significantly aid in maintaining habitable conditions, with the final total water inventory only slightly higher than in the simulations without a basal magma ocean. Many BMO simulations in our tested parameter space end up with a significant portion of water trapped within the solid mantle and little to none on the surface when compared to the same scenario in the simulations sans BMO. This reiterates the previous results of, e.g., Schaefer & Sasselov (2015) and Korenaga et al. (2017): an aging planet soaks up water in the mantle, sometimes to the detriment of surface habitability.

Depending on τ_{BMO}, the basal magma ocean injection rate could be similar to the diffusion-limited loss rate. If atmospheric loss is predominantly diffusion-limited for the majority of the simulation, as our model inherently assumes, then a long-lived basal magma ocean helps keep the mantle hydrated but does not keep the surface habitable.

Before moving on, we include Fig. 3.4 to display the evolution of water inventories when varying the surface magma ocean water saturation limit C_{sat}. The top two panels show similar behaviour for $C_{\mathrm{sat}} = 0.1$ and 0.01, albeit with different amounts of water loss to space. This is expected, since decreasing C_{sat} leads to earlier atmospheric degassing and hence earlier energy-limited loss, which then occurs for the remainder of the MO phase.

The bottom panel of Fig. 3.4 shows $C_{\mathrm{sat}} = 0.001$, a value which is below the initial water inventory of 6 Earth Oceans. Because $C_0 < C_{\mathrm{sat}}$, an atmosphere is immediately degassed, and energy-limited loss is ongoing for the entire MO phase. Since atmospheric desiccation is very rapid, the inset panel makes the evolution of the various water inventories much clearer: the planet nearly becomes completely desiccated, save for a small amount of water sequestered in the solid mantle. Hence,

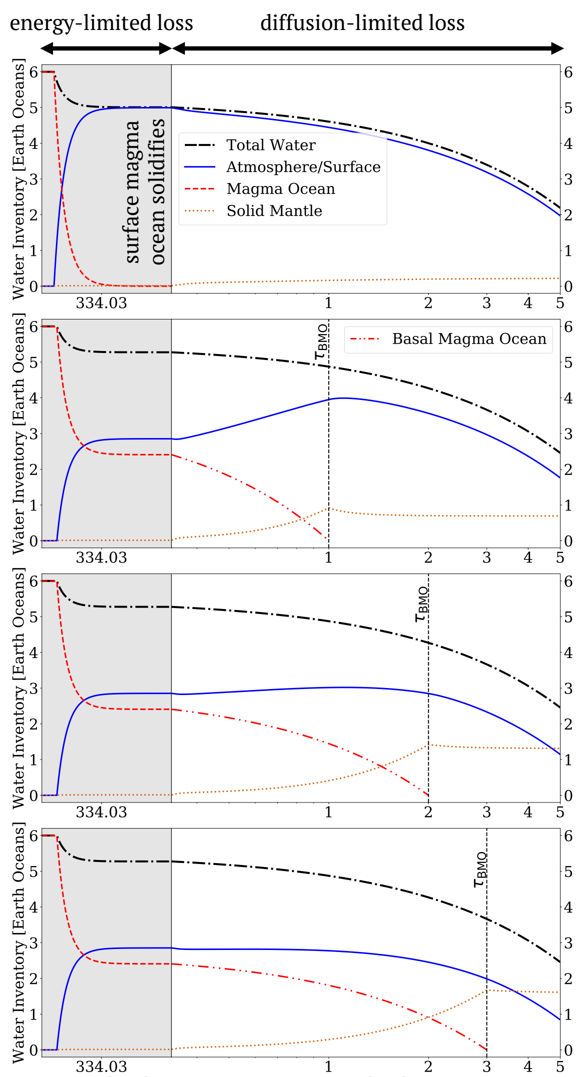

Figure 3.3: Water evolution for an M-Earth orbiting at the inner edge of the habitable zone (Inner HZ) of an M8 host star. The planet is initialized with 6 Earth Oceans; the surface magma ocean water saturation limit is $C_{\text{sat}} = 0.01$, and the surface magma ocean/runaway greenhouse phase (left part of the figure, shaded grey and plotted on a reverse log scale) lasts $\tau_{\text{MO}} = \tau_{\text{RG}} \approx 335$ Myr. The topmost panel corresponds to the model without a basal magma ocean, while the following three display results for different basal magma ocean (BMO) lifetimes, τ_{BMO}. In the simulation sans BMO (top), most water is in the atmosphere/surface reservoir following surface magma ocean solidification, where it is susceptible to be lost to space. In contrast, substantial water remains sequestered within a BMO while only ∼60% of the total water is degassed into the atmosphere. Longer-lived basal magma oceans lead to slower injection and more water trapped in the cooling mantle; indeed, for $\tau_{\text{BMO}} = 1$ Gyr, the injection into the relatively hot mantle allows the surface water inventory to briefly grow, while $\tau_{\text{BMO}} = 3$ Gyr results in more water within the mantle than at the surface. Following BMO solidification, water continues to be lost from the surface at the diffusion-limited rate; by 5 Gyr, the planet retains water and remains habitable in all scenarios. The presence of a basal magma ocean improves water retention, but at the detriment of surface habitability: the water sequestered in the basal magma ocean tends to remain in the mantle.

Fig. 3.4 shows that, depending on C_{sat}, an M-Earth which may be expected to lose substantial water to space can be saved through dissolution of water within the surface magma ocean for extended periods. We further explore this behaviour as we explore parameter space in the following section.

3.4.3 Parameter Space Exploration

Next, we include results for a region of parameter space explored for a given host star. Specifically, we can represent the evolution of water inventory for each combination of initial water inventory M_{init} and location within the habitable zone.

The parameter space results for M1, M5, and M8 host stars (not shown) look nearly identical between their corresponding simulations without and with a basal magma ocean (BMO), albeit with final water inventories differing by a few percent. This supports the result of Fig. 3.3: regardless of host star, a BMO does not significantly alter the habitability prospects when surface water is used as a proxy for habitability. Indeed, a longer BMO can be detrimental to surface habitability as water becomes trapped in the mantle below a desiccated surface. For all host stars, M-Earths initiated with 2 Earth Oceans become completely desiccated, while M-Earths with more initial water are often able to avoid or recover from desiccation, depending on their orbital distance and surface magma ocean/runaway greenhouse duration. Interestingly, for the M5 host star, $C_{\mathrm{sat}} = 0.01$, and an initial water content of 4 Earth Oceans at the Inner HZ leads to a desiccated surface for the BMO simulation, but the sans BMO simulation survives in a habitable regime; this also occurs for 6 Earth Oceans when $C_{\mathrm{sat}} = 0.001$, and for the M1 host star for 4 Earth Oceans

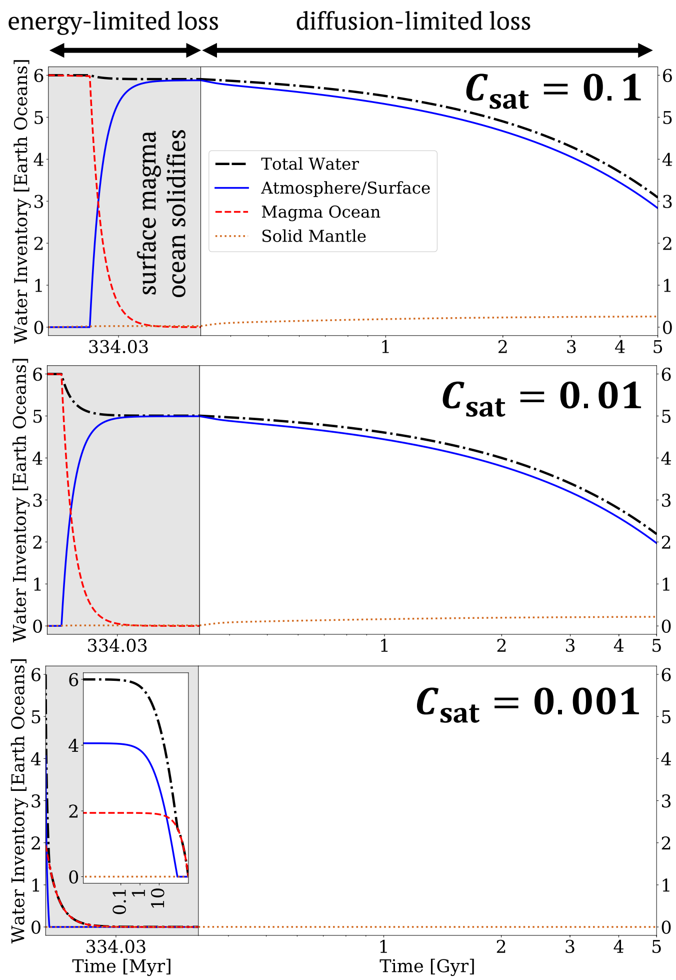

Figure 3.4: Same as the case in the top panel of Fig. 3.3, but now for different surface magma ocean (MO) water saturation limits, C_{sat}. Decreasing C_{sat} leads to earlier degassing of an atmosphere during MO, meaning energy-limited loss of water to space begins earlier as well. This is clear when comparing the top two panels: $\sim$1 Earth Ocean more water is lost when C_{sat} is decreased from 0.1 to 0.01. For $C_{\text{sat}} = 0.001$ (bottom panel), an atmosphere is degassed immediately since the saturation limit is below the initial water inventory. Because the evolution of water inventories is difficult to see on the reverse-log scale, we include an inset panel during the MO phase, which makes it clear that immediate degassing and ongoing energy-limited loss with $\epsilon_{\text{XUV}} = 0.1$ rapidly leads to desiccation of the atmosphere/surface, and a very small amount of water locked within the solid mantle. For sufficiently high water saturation limits, an M-Earth is able to survive desiccation, despite the expected 10.5 Earth Oceans of loss, through dissolution of water within the surface magma ocean, which can protect it from loss to space for long periods.

and $C_{\mathrm{sat}} = 0.1$. This is due to water becoming trapped in the solid mantle as water is injected into the mantle from the basal magma ocean at a constant rate.

Further, the results are almost the same for surface magma ocean (MO) water saturation limits of $C_{\mathrm{sat}} = 0.1$ and 0.01. For these highest tested values of C_{sat}, water is protected from extensive loss to space during the MO phase, as atmospheric degassing is delayed until very close to the end of the MO phase due to the high solubility of water within the magma. For $C_{\mathrm{sat}} = 0.01$, substantial water becomes locked in the mantle during the deep-water cycling phase, which can result in a desiccated surface above a hydrated mantle.

For $C_{\mathrm{sat}} = 0.001$, however, planets lose significantly more water to space, with more planets becoming desiccated due to the earlier atmospheric degassing and ongoing energy-limited loss during the surface magma ocean/runaway greenhouse phase. This low magma ocean saturation limit is below the concentration of all tested M_{init}, meaning the surface magma ocean begins saturated with water and thus an atmosphere is immediately degassed. The M1 host star simulations are the most similar for different values of C_{sat}, owing to the comparatively shorter runaway greenhouse phases experienced by the orbiting planets.

Fig. 3.5 presents the parameter space results, as M_{init} vs. Location within HZ, for the sans basal magma ocean simulations of an M8 host star and $C_{\mathrm{sat}} = 0.1$, 0.01, and 0.001. Decreasing C_{sat} leads to earlier degassing and less total final water: less water becomes sequestered in the mantle and more water is lost to space. As expected, there is slightly more total water at the end of simulations with a basal magma ocean than simulations sans basal magma ocean, but often water becomes trapped in the mantle while the surface becomes desiccated through loss to space.

Although energy-limited loss is ongoing for the entire lifetime of the surface magma ocean for $C_{\mathrm{sat}} = 0.001$, the atmosphere is able to grow near the end of surface magma ocean phase in some regions of parameter space. Fig. 3.5 shows that coupled magma ocean and deep-water cycling can maintain habitable surface conditions on a planet that would naively be expected to become desiccated based solely on the expected atmospheric loss; the planets rescued from desiccation by our model are indicated by purple boxes. This coupling may be a useful mechanism for the closely-orbiting planets of the TRAPPIST-1 system (Gillon et al. 2017), specifically TRAPPIST-1d (e.g., Krissansen-Totton & Fortney 2022).

For the highest initial water inventory simulations — $M_{\mathrm{init}} = 50$, 100, 200, and 400 Earth Oceans — only a maximum of $\sim$6 Earth Oceans becomes locked in the solid mantle, which is still far below our adopted mantle saturation limit of 12 Earth Oceans. This is likely because of our chosen basal magma ocean partition coefficient of $D = 0.2$; it is conceivable that, for huge M_{init} or higher D, the mantle could become saturated and the BMO would effectively inject water directly to the surface, potentially counteracting the loss of water to space depending on the rates of injection and loss. Although we do not see this behaviour in our model, there are regions of parameter space that allow the atmosphere to grow during deep-water cycling, in particular when the basal magma ocean lifetime is short and the injection rate is high (see, e.g., Fig. 3.3).

For simulations assuming energy-limited loss to space throughout, the loss of water to space is predictably much greater than when loss is diffusion-limited during deep-water cycling. Loss to space is especially devastating for simulations with $C_{\text{sat}} = 0.001$ for which an atmosphere is present and the MO is saturated throughout the entirety of the MO phase. For comparison, for both sans BMO and BMO simulations with $C_{\text{sat}} = 0.01$ and energy-limited loss only, 3/12 simulations around an M8 star end in a habitable surface regime compared to 9/12 with our our nominal energy-limited loss during MO, diffusion-limited loss during deep-water cycling prescription shown in the middle panel of Fig. 3.5; for $C_{\text{sat}} = 0.001$, this is further reduced from 5/12 (bottom of Fig. 3.5) to 2/12. These excessive amounts of energy-limited water loss are more comparable to the results of Luger & Barnes (2015) when they adopted energy-limited loss for the entirety of their simulations.

3.5 Discussion

The majority of our basal magma ocean simulations lead to a similar result: substantial water becomes trapped in the solid mantle — an increasing amount with increasing basal magma ocean lifetime due to slower injection — which can lead to dry, or even desiccated, surfaces but water-rich mantles. This means that, generally, the surface water inventory simply decreases with time as water is lost to space.

However, there are regions of parameter space where the surface inventory is able to grow following surface magma ocean solidification. This can occur when the basal magma ocean lifetime is short enough that the water injection rate is high and the mantle is still hot and actively degassing to the surface. Regardless, this does not occur over the entirety of the parameter space, and thus this mechanism — effectively injecting water from the basal magma ocean to the surface — may be

Figure 3.5: Parameter space results for an Earth-like planet without a basal magma ocean orbiting an M8 host star. Each panel corresponds to a different surface magma ocean (MO) water saturation limit, $C_{\rm sat}$. Within each panel, the initial water inventory is illustrated by a dashed orange circle, while the final water inventory is represented by a green-filled circle, scaled relative to the dashed orange circle to represent the fraction of water lost (a black X denotes a desiccated surface). The expected loss shown along the bottom of the figure is taken from Table 3.1. Decreasing $C_{\rm sat}$ leads to earlier degassing of an atmosphere during the surface magma ocean phase, and hence more extensive energy-limited loss. Indeed, the bottom panel corresponds to a water saturation limit *below* all tested initial water inventories; since the MO begins saturated, a substantial atmosphere is immediately degassed, and atmospheric degassing is ongoing throughout the MO phase. Purple boxes indicate scenarios where the M-Earth started with less water than it was expected to lose (Table 3.1), but nonetheless ended with significant surface water: these survivors are a testament to the ability of a long-lived magma ocean to protect a planet's water from loss to space.

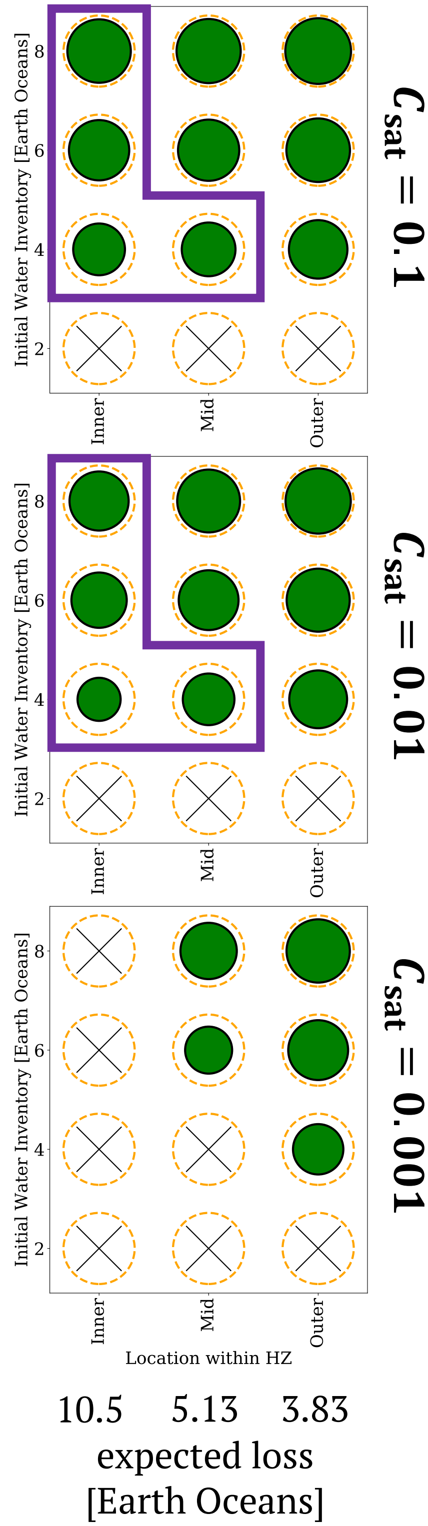

unlikely, especially if basal magma oceans persist for a few Gyr. Hence, the lifetime of a basal magma ocean is critical to the fate of water partitioning on an M-Earth. Based on this study, however, it appears that a basal magma ocean may not actually benefit habitability save for a few specific regions of parameter space.

A key assumption of the present study is that the orders-of-magnitude higher energy-limited escape only occurs during the earliest stage of the M-Earth, the concurrent surface magma ocean/runaway greenhouse phase, a time during which water could be mostly dissolved and protected depending on the water saturation limit of the magma. The loss of water to space is greatest at the inner edge of the habitable zone, and around late M-dwarfs.

Based on our simulation results, it seems that Luger & Barnes (2015) may have overestimated the loss of water to space when assuming energy-limited loss throughout; our energy-limited-only simulations exhibit catastrophic loss rates similar to Luger & Barnes (2015), even with our tested $\epsilon_{\mathrm{XUV}} = 0.1$ lower than their tested range of 0.15–0.3, while our nominal loss prescription (energy-limited during surface magma ocean and predominantly diffusion-limited otherwise) — coupled with magma oceans and a deep-water cycle — indicate more modest amounts of water loss, much less than the maximum expected amounts in Table 3.1. Recent studies of the TRAPPIST-1 planets find more modest loss rates of water — roughly 1-10s of Earth Oceans, depending on the initial water content of the planet — with less water lost from the further-out planets (Bolmont et al. 2017a; Barth et al. 2021). If the surface magma ocean behaves in the way we have modelled, and if our prescription for atmospheric loss is correct, then we have done a thorough exploration of parameter space.

Another key question involves our treatment of atmospheric loss, and whether either of our loss prescriptions are realistic. For example, how well are we capturing diffusion-limited escape, which we presume predominantly occurs when the surface is solid? Perhaps a more realistic parameterization (i.e., one in which we calculate T_{therm} instead of holding it fixed, or include a background atmosphere such as the build-up of oxygen through water loss) would change the overall amount of water lost.

Moreover, the tail end of the surface magma ocean/basal magma ocean periods are the most important, especially their details; indeed, increasing C_{sat} leads to later degassing of an atmosphere from which water can be lost to space. Based on our energy-limited-only simulations, it appears that if energy-limited loss persists long after the surface magma ocean/runaway greenhouse period, a basal magma ocean could potentially be the saviour for habitability if injection continues once the host M-dwarf becomes less active. The treatment of atmospheric loss is crucial in determining when and how much water is lost from an M-Earth.

Our treatment of surface temperature T_{surf} is effectively a step function: $T_{\text{surf}} =$ 1800 K during runaway greenhouse, and $T_{\text{surf}} = 293.15$ K otherwise. However, since neither the energy-limited nor diffusion-limited loss rates explicitly depend on surface temperature, the main impact will be on the thermal evolution of the mantle, which depends on the temperature contrast between the surface and the mantle, and the cycling rates, which depend on the mantle temperature. Because of this, we test two additional fixed temperate surface temperatures: $T_{\text{surf}} = 273.15$ K and $T_{\text{surf}} = 313.15$ K. Since the mantle is still an order-of-magnitude hotter than the surface, there is little effect: we find no discernible differences in the temporal plots or parameter space plots (for sans BMO simulations around an M8 host star, initiated with 6 Earth Oceans at the Inner HZ, and $C_{\mathrm{sat}} = 0.01$). Hence, a step-wise T_{surf} seems suitable for the present study.

Early stage variables of our model are critical in determining the outcome and partitioning of water on an M-Earth, whether related to the host star or the planet itself. For example, we hold both the XUV saturation timescale and XUV absorption efficiency constant regardless of host star or orbital distance; the former may vary from 100s of Myr to multiple Gyrs and governs the energy-limited loss rate, while the latter, if decreased, would also decrease the energy-limited loss rate. Although we adopt a fixed $\epsilon_{\mathrm{XUV}} = 0.1$, which falls roughly in the middle of the literature range, adopting $\epsilon_{\mathrm{XUV}} = 0.01$ for a pure water atmosphere as suggested by recent studies (e.g., Ercolano & Clarke 2010; Lopez 2017) would reduce the amount of water lost through energy-limited escape by an order-of-magnitude and improve water retention, potentially making the magma ocean stage — during which water is hidden from high rates of energy-limited loss — moot.

As a sensitivity analysis check, we run the parameter space simulation shown in Fig. 3.5 using a lower $\epsilon_{\mathrm{XUV}} = 0.01$. This order-of-magnitude lower energy-limited escape results in all simulated planets maintaining water for the 5 Gyr simulations. If energy-limited escape only has an efficiency of $\epsilon_{\mathrm{XUV}} = 0.01$ for terrestrial planets orbiting M-dwarfs, then these planets should often be habitable, in contrast with the dire predictions of Luger & Barnes (2015).

We also assume that the surface magma ocean solidifies on the same timescale as the runaway greenhouse duration, $\tau_{\mathrm{MO}} = \tau_{\mathrm{RG}}$, since the very high runaway greenhouse temperatures should maintain a molten silicate surface and slow magma ocean cooling. This seems like a reasonable assumption, and could be further improved by linking the runaway greenhouse duration directly to the water inventory of an M-Earth, but it would not change our results: once all of the water has been lost from a planet, the rate of atmospheric loss is irrelevant.

The water partition coefficient, D, governs the partitioning of water between atmosphere/solid mantle following surface solidification, and the amount locked within the solid mantle is either very low (sans BMO, $D = 0.001$) or moderate (with BMO, $D = 0.2$); however, as previously mentioned, the latter may lead to a substantial portion of the final water trapped in the mantle by 5 Gyr. This could be made more realistic with a higher-complexity model of the surface magma ocean phase including a pressure-dependent D that changes as the solidification front moves up towards the surface (see, e.g., Papale 1997, 1999).

Another important early-stage variable is the water saturation limit of the surface magma ocean, C_{sat}. Based on our simulation results, we find that for higher saturation limits, water is protected against loss to space during the earliest stages of M-Earth evolution, the simultaneous surface magma ocean/runaway greenhouse stage, due to its very high solubility within the silicate melt. For lower C_{sat} — especially when the initial dissolved water inventory is greater than the saturation limit of the magma — an atmosphere is degassed much earlier and sometimes immediately, and thus loss persists at the energy-limited rate throughout this early stage. Indeed, the dissolution of water within a surface magma ocean protects it against the most significant energy-limited loss to space, and this protection persists longer with increasing C_{sat}.

Many nuances of the habitability of terrestrial planets around M-dwarfs are not included in our box model. For example, we hold the orbital distance fixed, although potential orbital migration could move planets into, or out of, the habitable zone during their evolution. Further, although we assume a pure water vapour atmosphere throughout our simulations, the atmospheric composition will actually change over time as water molecules are photodissociated into their components; although the lighter H will predominantly be lost, the heavier O could potentially build up in the atmosphere, becoming a significant component and slowing the loss of H to space. Atomic cooling of the atmosphere may also suppress atmospheric escape rates. Further, Johnstone et al. (2019) note that the energy-limited escape formalism may be inappropriate for early atmospheres (primarily composed of H/He) which lack the necessary molecules to absorb XUV radiation, such as ozone within the Earth's atmosphere. Although our box model results are robust, they are merely the tip-of-the-iceberg in investigating the complex and highly-coupled nature of planetary habitability.

3.6 Conclusions

The orbital distance of a terrestrial planet around its host M-dwarf will determine the duration of the runaway greenhouse phase. In principle, M-Earths could lose 3-11 Earth Oceans if energy-limited loss operates only during the runaway greenhouse; the loss could be up to 20 Earth Oceans if energy-limited loss operates for the first 5 Gyr of the M-Earth's lifetime. These amounts are modest compared to the expected water inventories of M-Earths, and through coupling interior-atmosphere water evolution, we find that desiccation of these planets may have been overstated in previous studies.

The runaway greenhouse is coeval with the surface magma ocean phase, during which most water is safely hidden below the surface; hence, the actual loss rates are even lower than the values stated above (unless energy-limited loss operates for the entire planetary lifetime, which seems unlikely). Further, if an order-of-magnitude lower XUV absorption efficiency is assumed, as suggested by recent literature, the amount of water lost is extremely small and planets remain habitable throughout the simulations. Again, the desiccation problem appears to have been overstated.

Our results indicate that a basal magma ocean helps keep the mantle hydrated at late times, and hence could help keep planets geologically active, but it is unlikely to help replenish surface liquid water (once again, barring the strange case of energy-limited loss throughout). In general, water in the system tends to migrate into the solid mantle as it cools, which means that basal magma oceans and other deep water reservoirs will help hold onto water, but not easily bring that water up to the surface. Hence, to first-order, little to no water is lost during the magma ocean stage, and only a modest amount is lost in the remaining Gyrs, regardless of the deep-water cycle and the presence of basal magma oceans.

If this result holds, it would bode well for the habitability of M-Earths — most should have surface water even if they do not have operating plate tectonics or a basal magma ocean. Future studies should revisit the atmospheric loss of M-Earths using higher-complexity models (e.g., Krissansen-Totton & Fortney 2022; Lichtenberg et al. 2022), and observers should empirically establish whether any M-Earths have atmospheric water vapour. If M-Earths do not have water, it might suggest that they either form drier than expected, magma oceans have a smaller water capacity, or that atmospheric loss is more efficient than we believe.

Acknowledgements

KM and NBC acknowledge Colin Goldblatt for useful discussions and critical input on this study and manuscript. KM thanks Yi Huang for conversations about stratospheric moisture and convection, and Lena Noack and Tim Lichtenberg for valuable discussions about the scientific background and model results. NBC acknowledges insightful discussions with Joe O'Rourke, Leslie Rogers, and Chen Sun at the Signature of Life in the Universe Scialog workshop. KM acknowledges support from a McGill University Dr. Richard H. Tomlinson Doctoral Fellowship, and from the Natural Sciences and Engineering Research Council of Canada (NSERC) Postgraduate Scholarships-Doctoral (PGS D) Fellowship.

Data Availability

The simulation results presented within this manuscript are available in the following Zenodo repository: 10.5281/zenodo.8334934. The model is available from the corresponding author at reasonable request.

Interlude II

This chapter presented the results of our improved coupled box model, beginning from a magma ocean phase before transitioning to deep-water cycling, for simulations with and without a residual basal magma ocean. We determined that habitability prospects can be improved through dissolution of water within a magma ocean, although the benefit depends on when exactly the water is degassed to the surface. Although a significant improvement over Moore & Cowan (2020), there were still many aspects that could be improved or added to our 0-D model.

During the writing process of the paper, I was fortunate to participate in a 3-month internship at the Freie Universität Berlin in Berlin, Germany, working with Lena Noack to further improve the model geophysics by accounting for a stagnant lid tectonic mode, instead of the thus-far assumed plate tectonics, within the coupled model. This provided an invaluable experience, as I met prominent European researchers in the field. I am still working with one of Lena's students, Julia Schmidt, to implement atmospheric loss into her 2-D interior convection model. However, addition of a stagnant lid mode — and transitioning between stagnant lid and plate tectonics — did not seem feasible for our 0-D model. This will instead be addressed in future work.

Upon returning from Berlin, we decided to instead focus on testing the impact of planetary mass on the thus-far promising habitability prospects of terrestrial planets. Since many of our model parameters were already explicitly mass-dependent, extending the results from Earth-mass planets to super-Earths seemed logical. This low-hanging fruit seemed ripe to write a shorter third manuscript for my thesis, and could be done in concert with enhancing the box model to be more user-friendly. Since the analysis and writing process for this chapter was still underway, Nick suggested that we co-supervise undergraduate students on their senior thesis, mentoring and guiding them through understanding the model and producing mass-dependent simulation results to assess the habitability of various mass terrestrial planets. This plan came to fruition when we found two interested undergraduates, and the project began in September 2022.

Chapter 4

The Impact of Planetary Mass on the Surface Water Inventories of Terrestrial Planets Around M-Dwarfs

This thesis chapter presents an in-preparation manuscript written after co-supervising two undergraduate students on their senior thesis.

Authors

Keavin Moore [1], Benjamin David [2], Albert Yian Zhang [2], Nicolas B. Cowan [1,2]

[1] Department of Earth & Planetary Sciences, McGill University, 3450 rue University, Montréal, QC, H3A 0E8, Canada

[2] Department of Physics, McGill University, 3600 rue University, Montréal, QC, H3A 2T8, Canada

Preface

The final manuscript, presented within this chapter, was produced through co-supervision of two undergraduate students on their senior thesis, Benjamin David and Albert Yian Zhang. This chapter presents simulation results for Earth-mass and super-Earth planets to determine how planetary mass affects habitability prospects. I was able to teach the students about the project, the box model and its code. I provided guidance as the model was cleaned and upgraded to be accessible through open-source Github. The work was carried out from September 2022 to April 2023, and during this time, the students determined all sources of mass-dependence within the code before running and analyzing simulations of super-Earths. From May to August 2023, I performed the final simulations, analyzed the results, and completed the manuscript that had been started nearly a year earlier.

Through these new mass-dependent simulations, we were able to compare the evolution and partitioning of planetary water inventories throughout the early lifetime of these terrestrial planets around active M-dwarf host stars, and compare with our expectations based on the students' investigation. We also further explore the effect of the solid-melt magma ocean water partition coefficient, expected to increase with mass as interior pressures increase. Interestingly, depending on the treatment of the initial planetary water inventory, although the amount of water lost to space roughly increases with mass due to the long diffusion-limited escape during deep-water cycling, more water becomes sequestered and potentially trapped within the mantle as planetary mass increases.

Abstract

Terrestrial planets orbiting M-dwarf stars may be the most common habitable planets in the Universe. However, their surface habitability is in jeopardy due to intense irradiation from their host stars, which drives the escape of water to space and can lead to surface desiccation. We present simulation results of a 0-D box model, coupling water cycling between interior and atmosphere and loss to space, for terrestrial planets of mass 1–8 $M_\oplus$. We find that the energy-limited loss rate during the magma ocean phase decreases with planetary mass, while diffusion-limited loss during deep-water cycling increases with mass. The surface gravity of super-Earths is a critical parameter governing the cycling and escape rates, and hence water partitioning, within our box models. When planets begin with the same water mass fraction, many more uninhabitable waterworlds arise for larger planetary masses; when initiated with the same mass of water, however, more massive planets are more likely to have uninhabitable, desiccated surfaces. Further, we find that more water becomes sequestered within the solid mantle for greater planetary masses, even if the amount of surface water is comparable at simulations' end. While this may be beneficial to ongoing plate tectonics, it is uncertain if or when the water in the mantle could be brought to the surface to recover habitable conditions.

4.1 Introduction

4.1.1 Habitability of Earth-like Planets

The habitability of planets like the Earth — rocky and orbiting a G-dwarf host star — has been questioned and investigated since the first exoplanet detections. It is only in recent years, with wider surveys and improved observational techniques, that rocky planets around M-dwarfs have become prime targets. These stars are the most abundant in the Galaxy and are expected to host many rocky planets (e.g., Dressing & Charbonneau 2015; Sabotta et al. 2021), but M-dwarfs are significantly more active across the electromagnetic spectrum than G-dwarf stars. As a result, the habitability of rocky planets orbiting M-dwarfs is at risk due to higher irradiation and the extended early evolutionary periods of M-dwarfs (for a review, see Shields et al. 2016).

The significant radiation impinging on the atmospheres of these rocky planets can lead to rapid and significant loss of water to space, or even surface desiccation. Two previous studies (Moore & Cowan 2020; Moore et al. 2023) used box models to investigate the fate of planetary surface water as a proxy for habitability. These models include atmospheric loss to space, and track water evolution between various planetary reservoirs during an early magma ocean stage and a plate-tectonics-driven deep-water cycling phase. These results led to the conclusion that sequestering water in an interior reservoir — away from loss to space for prolonged periods — can improve the habitability prospects of Earth-mass planets.

4.1.2 Habitability of Super-Earths

Rocky planets larger than the Earth are expected to be more common than Earth-like planets around M-dwarfs (e.g., Dressing & Charbonneau 2015; Mulders et al. 2015; Hsu et al. 2020; Chachan & Lee 2023) and as such, their water evolution must be investigated (e.g., Kruijver et al. 2021). These "super-Earths" have masses in the range $1\ M_{\oplus} < M_p \leq 10\ M_{\oplus}$, and super-Earths orbiting low-mass stars may be the most common habitable planets. How will water evolution and partitioning vary over time as planetary mass is increased?

Super-Earths form with greater accretional energy than their Earth-mass counterparts, and likely have deeper magma oceans (Stixrude et al. 2020). Super-Earths have greater surface areas (related to, e.g., the thermal evolution of the planet) and greater volumes (related to, e.g., the size and capacity of water reservoirs). Both the extent and the water capacity of the early magma ocean should increase with increasing mass (cf. Cowan & Abbot 2014). The interplay between surface area and volume means a more massive planet will cool slower since volume scales more rapidly than surface area (e.g., Seales & Lenardic 2021). This could prolong the magma ocean phase, and maintain a hotter solid mantle during deep-water cycling. However, the slower cooling could mean that super-Earths take longer to achieve temperate/habitable surface conditions, if at all (O'Neill & Lenardic 2007; Korenaga 2010; Stamenković et al. 2012). As in the current study, recent studies (Krissansen-Totton et al. 2021b,a; Krissansen-Totton & Fortney 2022) have also tied the solidification of the magma ocean to the runaway greenhouse phase due to the exceedingly hot surface temperatures leading to a molten surface.

Due to the higher planetary radius, more water may be dissolved within the deeper magma ocean and protected from loss to space. The water saturation limit of the magma ocean controls the timing of atmospheric degassing, and will be different due to the higher internal pressures. Super-Earths will have higher surface gravity than Earth-mass planets as well, which should presumably suppress loss.

The surface of a super-Earth should accommodate more water before becoming inundated. Based on Cowan & Abbot (2014) and the scaling relations of Valencia et al. (2006), the waterworld limit of an 8 $M_\oplus$ super-Earth is $\sim$20 Earth Oceans. Plate tectonics requires water dissolved in the mantle, but also moderate surface temperatures, which may be significantly delayed or never arise on super-Earths. Super-Earths may not experience plate tectonics at all, perhaps being restricted to a stagnant-lid mode (e.g., O'Neill & Lenardic 2007; Korenaga 2010). Regardless, we restrict this study to a plate-tectonic regime.

A hotter mantle following surface solidification will lead to increased early degassing from mantle to surface, and this water may then be lost to space. While it has been previously predicted that super-Earth atmospheres are likely stable against XUV-driven thermal escape (Tian 2009), planetary interior reservoirs were neglected. The comparison between cycling rates — degassing and regassing — and the rate of water loss to space is critical. If regassing is not substantial during the earliest stages of deep-water cycling, the mantle could become rapidly desiccated and cease plate tectonics. The degassing rate and initial water inventory will be very important, since water may become trapped within the solid mantle as the mantle cools (Moore et al. 2023).

How will these competing, coupled effects alter the fate of surface water on super-Earths orbiting M-dwarf stars? These results will provide an assessment of surface habitability as a function of planetary mass. The manuscript continues as follows. In Section 4.2, we reiterate important aspects of our box model from Moore et al. (2023) before emphasizing mass dependence and our expectations. Section 4.3 then presents temporal water evolution and parameter space results for various terrestrial planets. These results are then discussed in Section 4.4 along with the nuances and exclusions of our super-Earth box model.

4.2 Methods

The model used in this study is a modified version of that in Moore et al. (2023), without a persistent basal magma ocean. We avoid explicitly repeating the details of the previous study here. Significant changes to the model and the mass dependence in certain equations are outlined below.

The overall planetary evolution pathway remains the same: the planet begins in a magma ocean phase, extending from surface to core, which is parameterized to solidify on the same timescale as the calculated duration of the runaway greenhouse phase (see Table 1 of Moore et al. 2023). Following surface solidification, plate tectonics begins, initiating the deep-water cycle. The planetary evolution in each evolutionary stage is coupled with water loss to space, in either the energy-limited (Watson et al. 1981; Luger & Barnes 2015) or diffusion-limited (Walker 1977; Luger & Barnes 2015) regime.

We explicitly detail the mass dependence and its expectations in our simulations. We use the scaling relations of Valencia et al. (2006) to calculate planetary parameters as a function of mass, such as planetary radius, surface area, and mantle volume. The relation between planetary radius, R_{p}, and mass, M_{p}, is:

$$R_{\mathrm{p}} = R_{\oplus} \left(\frac{M_{\mathrm{p}}}{M_{\oplus}} \right)^{0.27}, \tag{4.1}$$

where $R_{\oplus}$ and $M_{\oplus}$ are the radius and mass of the Earth, respectively.

We can substitute this relation into the equations for water loss to space. The energy-limited escape rate with planetary mass dependence is then:

$$\dot{M}_{\mathrm{energy-limited}} \propto \frac{R_{\mathrm{p}}^3}{M_{\mathrm{p}}} = M_{\mathrm{p}}^{-0.19}, \tag{4.2}$$

This equation states that the energy-limited escape rate will decrease with increasing planetary mass. Note, however, that the Valencia et al. (2006) do not explicitly account for molten phases, and thus do not fully represent the magma ocean stage; we leave this improvement to future work.

Again using the Valencia et al. (2006) scaling relations, the mass dependence of diffusion-limited escape is:

$$\dot{M}_{\mathrm{diffusion-limited}} \propto R_{\mathrm{p}}^2 = M_{\mathrm{p}}^{0.54}, \tag{4.3}$$

so diffusion-limited escape will increase with planetary mass. Given each potential water loss regime, we calculate the expected loss throughout 5 Gyr for each planetary mass in Table 4.1.

Table 4.2 shows the parameter space explored to investigate the effect of planetary mass on magma ocean evolution, deep-water cycling, and water inventories (including water partitioning) for the first 5 Gyr of the lifetime of super-Earths orbiting M-dwarfs. Four planetary masses — $M_\mathrm{p} = 1\ M_\oplus$, $2\ M_\oplus$, $4\ M_\oplus$, and $8\ M_\oplus$ — are explored. While the upper mass limit on super-Earths is closer to $10\ M_\oplus$, we test a lower value to avoid the mass transition from super-Earths to sub-Neptunes, i.e., from rocky to icy. The magma ocean water partition coefficient, D, should change with time as the magma ocean solidifies from the core-mantle boundary towards the surface, as it is a function of pressure (Papale 1997, 1999); internal pressures of super-Earths will also be higher than for Earth-mass planets. We hence test $D = 0.001$, 0.01, and 0.1, since we cannot fully represent this pressure-dependence in our 0-D box model. Four initial water mass fractions are explored, ranging from 4.7×10^{-4} to 1.9×10^{-3}; these presume that water delivery is a consequence of accretion, and hence, the initial planetary water inventory will scale with mass. Further, we also run a set of simulations that instead begin with the same initial water inventory, 2, 4, 6, and 8 Earth Oceans, which instead assumes that the planetary water inventory is instead delivered later by e.g., comets, and hence planets will begin with the same water inventory regardless of planetary mass. Three fixed orbital distances within the habitable zone (HZ) are simulated — Inner HZ, Mid HZ, and Outer HZ — calculated using the HZ relations of Kopparapu et al. (2013) and assuming an M8 host star. The water saturation limit of the magma, which controls the timing of atmospheric degassing during magma ocean, is held constant at $C_\mathrm{sat} = 0.01$.

We note that the water capacity of the mantle will increase as the planetary mass increases. As such, adopting the 12 Earth Ocean limit on mantle water capacity for a $1\ M_\oplus$ planet from Moore & Cowan (2020) and Moore et al. (2023), we assume the mantle water capacity scales as $(M_\mathrm{p}/M_\oplus) \times 12$ Earth Oceans. We do this for

Planetary Mass	Location Within Habitable Zone (HZ)	Maximum Water Loss [Earth Oceans]			
		EL during RG	DL rest of sim	Total	Max, EL only
1 $M_\oplus$	Hot, Inner Edge	7.72	2.82	10.5	19.7
	Middle (Mid)	2.18	2.95	5.13	8.64
	Cold, Outer Edge	0.83	2.99	3.83	4.83
2 $M_\oplus$	Hot, Inner Edge	6.77	5.64	12.4	17.3
	Middle (Mid)	1.91	5.91	7.82	7.58
	Cold, Outer Edge	0.73	5.98	6.71	4.23
4 $M_\oplus$	Hot, Inner Edge	5.93	11.3	17.2	15.2
	Middle (Mid)	1.67	11.8	13.5	6.64
	Cold, Outer Edge	0.64	12.0	12.6	3.71
8 $M_\oplus$	Hot, Inner Edge	5.20	22.5	27.8	13.3
	Middle (Mid)	1.47	23.6	25.1	5.82
	Cold, Outer Edge	0.56	23.9	24.5	3.25

Table 4.1: Expected amount of water that will be lost by each planetary mass at each orbital distance, neglecting a magma ocean and deep-water cycle. Here, "EL" refers to energy-limited loss, "RG" is the runaway greenhouse, and "DL" is diffusion-limited loss. Although these values are high — sometimes higher than the initial water inventory of the planet — these planets lose much less water, in practice, due to the highly coupled nature of water cycling between interior, surface, and atmosphere.

Name	Parameter	Values Tested
Planetary mass	M_p [$M_\oplus$]	1, 2, 4, 8
Initial water mass fraction	$(M_\mathrm{init}/M_\mathrm{p})$	4.7×10^{-4}, 9.4×10^{-4}, 1.4×10^{-3}, 1.9×10^{-3}
Initial water inventory	M_init [Earth Oceans]	2, 4, 6, 8
Magma ocean water partition coefficient	D	0.001, 0.01, 0.1
Orbital distance/location within HZ	a_orb	Inner HZ, Mid HZ, Outer HZ
Host stellar type	—	M8

Table 4.2: Parameter space explored in this study. Planetary mass is expressed in units of Earth masses, where $M_\oplus \approx 5.97\times10^{24}$ kg. Initial water mass fraction is based on [2, 4, 6, 8] Earth Oceans on a 1 $M_\oplus$ planet, where 1 Earth Ocean $\approx 1.4\times10^{21}$ kg. We run two sets of simulations: in the first, planets begin with the same initial water mass fraction, while the second initializes planets with the same water inventory, in Earth Oceans. The value of a_orb varies depending on the combination of host star and location within the habitable zone.

simplicity, and note that the planetary mantle does not become saturated within any of the present simulations; we leave realistic water capacity limits (such as those of, e.g., Guimond et al. 2023) to future work. Further, the different surface water regimes — waterworld, Earth-like (i.e., exposed continents & oceans), Dune planet, and desiccated — will also vary with planetary mass (see Fig. 4.1). A planet is a waterworld if $W_\mathrm{s} \leq 3.7(M_\mathrm{p}/M_\oplus)^{0.08}$ Earth Oceans (Cowan & Abbot 2014), Earth-like if $0.01(M_\mathrm{p}/M_\oplus)^{0.54} < W_\mathrm{s} < 3.7(M_\mathrm{p}/M_\oplus)^{0.08}$ Earth Oceans, a Dune planet if $10^{-5}(M_\mathrm{p}/M_\oplus)^{0.54} \leq W_\mathrm{s} \leq 0.01(M_\mathrm{p}/M_\oplus)^{0.54}$ (Abe et al. 2011), and desiccated if $W_\mathrm{s} < 10^{-5}(M_\mathrm{p}/M_\oplus)^{0.54}$ Earth Oceans, where 10^{-5} is the amount of water currently in the Earth's atmosphere (Gleick 1993).

4.3 Results

We begin by presenting results for simulations beginning with the same water mass fraction, $(M_\mathrm{init}/M_\mathrm{p}) = 4.7 \times 10^{-4}$, 9.4×10^{-4}, 1.4×10^{-3}, 1.9×10^{-3}. In doing so, we assume the water inventory is set during planetary accretion, and the initial amount of water contained in a planet will scale with mass: 1 $M_\oplus$ begins with [2, 4, 6, 8] Earth Oceans, while 8 $M_\oplus$ begins with [16, 32, 48, 64] Earth Oceans. We can then compare these results with simulations beginning with the same initial water inventory — [2, 4, 6, 8] Earth Oceans — regardless of planetary mass.

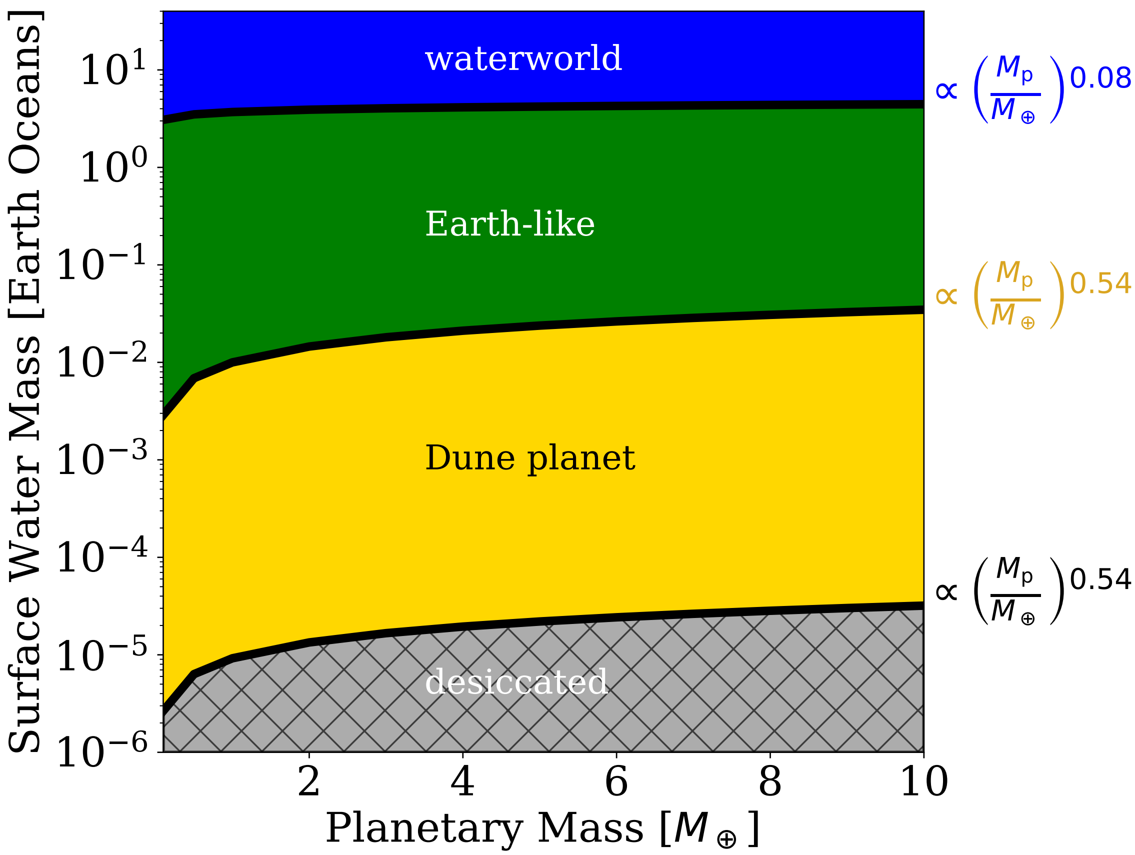

Figure 4.1: Surface water regimes for terrestrial planets ranging from 0.1 $M_\oplus$ to 10 $M_\oplus$. Each limit between regimes is explained in the text. The colours are later used in Fig. 4.4 to show the surface water regime at the end of the 5 Gyr simulations. Note that planets in either the Earth-like or Dune planet regime may be habitable, while the inundated waterworlds and desiccated surfaces are uninhabitable.

4.3.1 Same Initial Water Mass Fraction

Temporal Evolution

Fig. 4.2 displays the results of the 5 Gyr simulations for $M_\mathrm{p} = 1$ to 8 $M_\oplus$ (top to bottom). Within a given panel, the water evolution during the magma ocean stage is indicated by the shaded grey background on the left, while the deep-water cycling phase is on the right. Each simulation begins with 2 Earth Oceans, and the planet orbits at the inner edge of the habitable zone (Mid HZ). The top panel of Fig. 4.2 shows that the 1 $M_\oplus$ planet loses ~1/5 of the initial amount of water to space through energy-limited loss during the magma ocean phase, with continued diffusion-limited loss during deep-water cycling desiccating the planet by ~3 Gyr. The 2 $M_\oplus$ planet loses less water during magma ocean, but the enhanced diffusion-limited loss still leads to surface desiccation.

As planetary mass increases further, so too does the surface gravity, a parameter intrinsically tied to our deep-water cycling parameterization and the rate of water loss to space. For all four planetary masses, a small amount of water is partitioned into the solid mantle during the magma ocean phase, governed by solid-melt water partition coefficient, $D = 0.001$. During deep-water cycling, in the competition between degassing and regassing — both of which depend on surface gravity through seafloor pressure P — regassing prevails, and more water becomes sequestered in the mantle with increasing planetary mass. Although more water ends up locked within the mantle with increasing planetary mass, the 4 $M_\oplus$ planet is in a habitable surface regime by 5 Gyr, while the 8 $M_\oplus$ planet is an inundated waterworld (although both have a hydrated mantle, permitting ongoing plate tectonics). Fig. 4.2 also shows that the energy-limited loss rate decreases with mass, while diffusion-limited loss increases with increasing mass; indeed, both of these findings echo the expectations outlined in Section 4.2.

Next, we vary the magma ocean water partition coefficient, D, since its value may increase with mass as surface gravity increases. We test three orders-of-magnitude to investigate its effect on the water partitioning throughout the planet's evolution. Fig. 4.3 shows the water evolution results of simulations with $D = 0.001$, 0.01, and 0.1 for 1 $M_\oplus$ (left) and 2 $M_\oplus$ (right). Recall that D governs the water partitioning during the magma ocean phase only (i.e., the grey panels in Fig. 4.3), and that the partitioning during deep-water cycling involves the balance between rates of degassing, regassing, and loss to space.

As D is increased by a factor of 10, the amount of water sequestered within the solid mantle also increases. However, because of the much longer period of deep-water cycling, the final partitioning for a given mass at 5 Gyr is almost unchanged. This is apparent in the bottom panels: although nearly 1/3 of the initial water can become sequestered in the solid mantle, the majority is rapidly degassed to the surface once the magma ocean solidifies and deep-water cycling begins. Although the temporal evolution of water inventories may differ, the final water inventories and partitioning are not directly impacted by different values of D for the vast majority of our simulations. For 2 $M_\oplus$ and $D = 0.1$ (bottom right panel of Fig. 4.3), the planet barely avoids desiccation, while the lower values of D are desiccated by 5 Gyr. This is the only instance seen of this occurrence in the parameter space exploration, and for all other simulations, the results by 5 Gyr are unchanged.

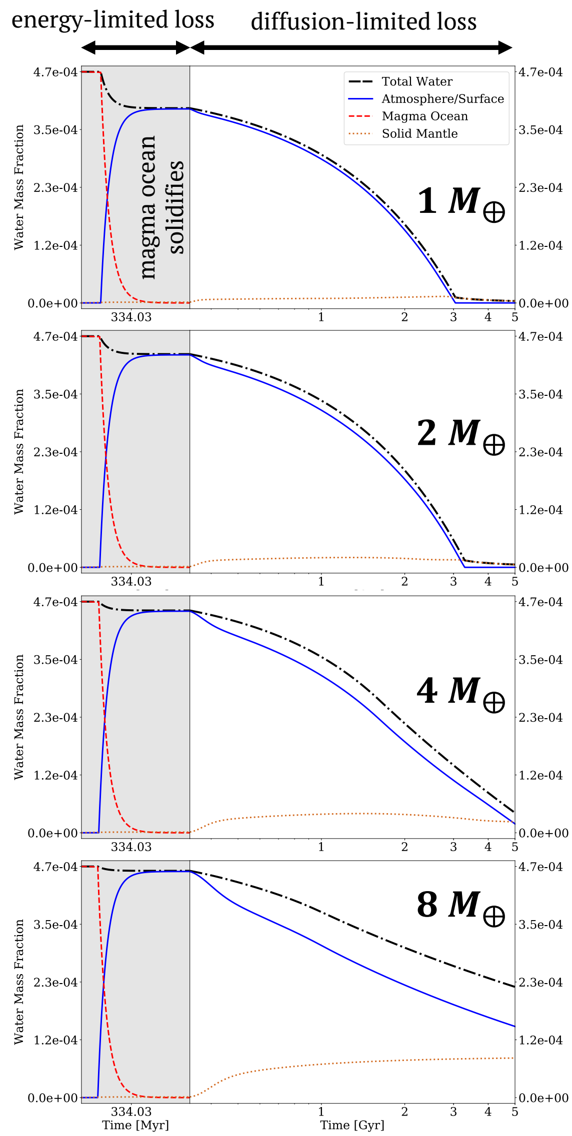

Figure 4.2: Comparison of evolution of water inventories for terrestrial planets of masses 1 $M_\oplus$ to 8 $M_\oplus$. Each simulation corresponds to a planet orbiting at the inner edge of the habitable zone (Inner HZ) initialized with a water mass fraction of 4.7×10^{-4}, and assumes a magma ocean water partition coefficient of $D = 0.001$. Although the two least massive planets become desiccated, the 4 $M_\oplus$ and 8 $M_\oplus$ planets retain a habitable surface by 5 Gyr. The final surface water inventory decreases with mass, while the total amount of water lost to space decreases with mass when desiccation is avoided. More massive planets have a higher surface gravity, so more water becomes sequestered (and trapped) within the mantle as planetary mass is increased.

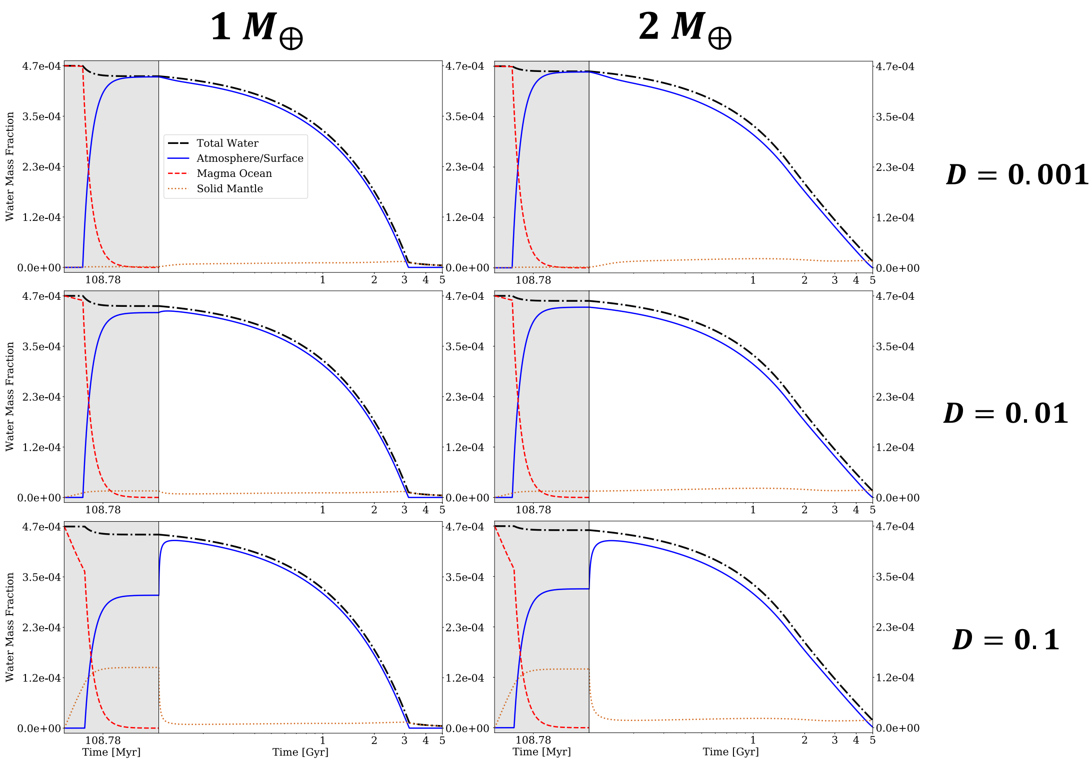

Figure 4.3: Comparison of three different magma ocean water partition coefficients — $D = 0.001$, 0.01, and 0.1 — for two different planetary masses: 1 $M_\oplus$ (left) and 2 $M_\oplus$ (right). Each planet is initialized with a water mass fraction of 4.7×10^{-4}, and orbits in the middle of the habitable zone (Mid HZ). As D is increased from 0.001 (top) to 0.1 (bottom), more water is sequestered within the solid mantle during the magma ocean phase (shaded grey). Recall also that more water becomes sequestered in the mantle with increasing M_p. All final water inventories and water partitioning for a given mass are nearly identical regardless of D, mainly because D governs the water partitioning during magma ocean only. For $D = 0.1$ (bottom panels), although substantial water is partitioned into the solid mantle, the majority of this water is rapidly degassed to the surface once the magma ocean solidifies due to our deep-water cycling parameterization. Interestingly, the 2 $M_\oplus$, $D = 0.1$ simulation barely avoids surface desiccation, while the corresponding $D = 0.01$ and $D = 0.001$ become desiccated; this is the only scenario in our parameter space exploration where this occurs, since the aforementioned slight difference between final water inventories normally does not change the results at 5 Gyr.

Parameter Space Exploration

Fig. 4.4 presents water evolution results for 1, 2, 4 and 8 $M_{\oplus}$, for a single $D = 0.001$, as Initial Water Mass Fraction vs. orbital position within the habitable zone (Location within HZ). As planetary mass is increased, the initial amount of water on the planet also increases. For 1 $M_{\oplus}$ seven simulations end in an Earth-like surface water regime, two end as waterworlds, and three become desiccated. The number of planets with desiccated surfaces decreases with mass, along with planets with Earth-like surfaces, while the number of waterworlds drastically increases; indeed, for 8 $M_{\oplus}$, all simulated planets are waterworlds by 5 Gyr.

However, since substantial water may be sequestered within the solid mantle — with the amount increasing with increasing mass due to the increasing surface gravity — we further include brown circles representing the final mantle water inventory, scaled to the initial water inventory. Indeed, this reveals that although surfaces may be desiccated, there could still be substantial water present within the solid mantle. While this permits ongoing plate tectonics, the cooling mantle degasses less water over time, and hence much of this water may remain trapped within the cooling mantle, providing no benefit to habitable surface conditions.

Fig. 4.4 also includes purple boxes to indicate planets that, if a deep-water cycle were neglected, would be expected to lose more water to space than their initial water inventory (see Table 4.1), with expected loss displayed either above or below the corresponding panel for a given planetary mass. These represent surface water "survivors" of our coupled modelling approach, and if coloured green, will be in habitable, Earth-like surface water regime. Interestingly, the number of survivors is roughly the same for each mass, although whether these survivors are Earth-like and habitable by 5 Gyr depends on both the initial water mass fraction/planetary mass, as well as the surface water limits shown in Fig. 4.1.

Fig. 4.4 is hence a further testament to the importance of coupling planetary interiors and surfaces/atmospheres: although we can make predictions based on physical processes and parameterized equations, our expectations likely do not incorporate the complexities of coupling planetary water exchange and atmospheric loss.

4.3.2 Same Initial Water Inventory

We now show results for simulations that begin with the same initial water inventory regardless of mass: [2, 4, 6, 8] Earth Oceans, i.e., assuming water is delivered after planetary formation is complete. These simulations provide a distinct comparison with those of the previous section, and elucidate the differences in water evolution and surface habitability prospects by beginning from the same initial conditions for all four planetary masses.

Temporal Evolution

Fig. 4.5 is the same as Fig. 4.2, but now all four planets begin the simulation with the same water inventory of 2 Earth Oceans. Although the two most massive planets retain some surface water when initiated with the same water mass fraction, all four simulations of Fig. 4.5 result in a desiccated, uninhabitable planet. By beginning with the same water inventory of 2 Earth Oceans, we can make clear distinctions regarding the effects of planetary mass on water cycling and loss to space.

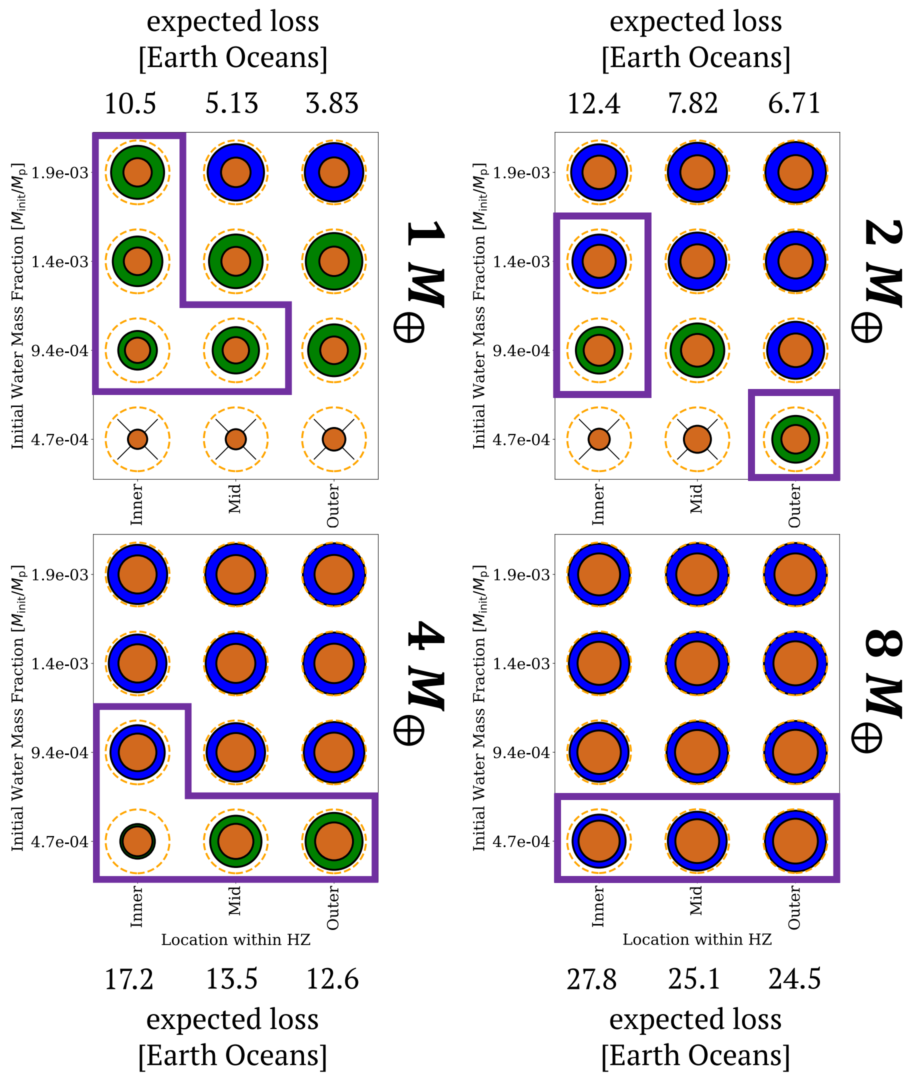

Figure 4.4: Parameter space exploration results for four planetary masses. Within each panel, the results are plotted as Initial Water Inventory vs. Location within HZ. The initial water inventory is indicated by a dashed orange circle, and the final water inventory by a thick black circle, coloured based on the surface water regimes in Fig. 4.1. Additionally, the final mantle water inventory is plotted — again scaled to the initial inventory — as a filled brown circle. Planets that were initiated with less water than they were expected to lose neglecting a deep-water cycle, but ended in a non-desiccated surface water regime due to our coupled modelling approach, are surrounded by purple boxes. As mass is increased, so too is the amount of water sequestered in the mantle, and the number of habitable planets decreases. Further, although all planets begin with the same water mass fraction, fewer planets become desiccated within increasing mass, but the majority of the simulated planets are uninhabitable waterworlds.

As mass is increased from top to bottom in Fig. 4.5, water loss to space in the energy-limited regime during the magma ocean phase decreases, while diffusion-limited loss during the longer deep-water cycling phase substantially increases. More massive planets become desiccated earlier, and although larger mantles sequester more water early in the deep-water cycling phase, this water is degassed to the surface and rapidly lost to space. Although the 1 $M_{\oplus}$ planet survives for nearly 3 Gyr before becoming desiccated, the 8 $M_{\oplus}$ planet is desiccated within only 100s of Myr after magma ocean solidification. The overall results — i.e., with increasing mass, decreased energy-limited loss during magma ocean, increased diffusion-limited loss during deep-water cycling, and more water sequestered in the mantle — are reiterated for simulations initialized with the same water inventory as with those beginning instead with the same initial water mass fraction. To further explore this relation, we present the entire parameter space exploration results in the following section.

Parameter Space Exploration

The results of the parameter space exploration in Fig. 4.6 are now presented as Initial Water Inventory [Earth Oceans] vs. Location within HZ. As planetary mass is increased, the loss of water to space also increases, and more simulations result in a desiccated surface, as indicated by a black X. However, substantial water may be sequestered within the solid mantle, with the final mantle water inventory represented by scaled brown circles. This reiterates that there may be significant water present — and potentially trapped — within the mantle below a desiccated surface.

Fig. 4.6 also includes purple boxes around surface water "survivors". These rep-

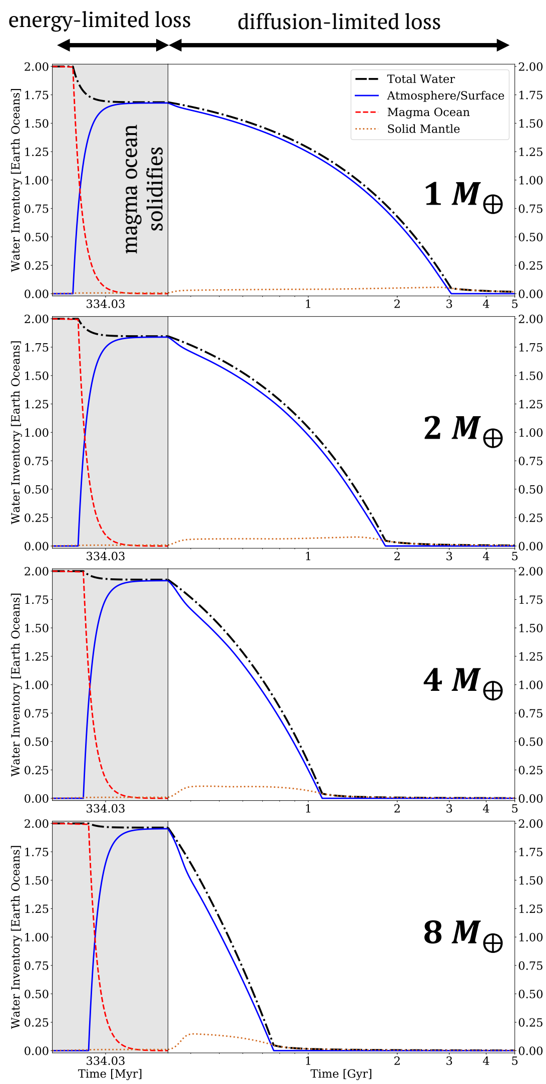

Figure 4.5: Comparison of evolution of water inventories for terrestrial planets of masses 1 $M_\oplus$ to 8 $M_\oplus$. Each simulation corresponds to a planet orbiting at the inner edge of the habitable zone (Inner HZ) initialized with a water inventory of 2 Earth Oceans, and assumes a magma ocean water partition coefficient of $D = 0.001$. At the closest orbital distance and lowest water inventory, all planetary masses become desiccated. However, due to the lower energy-limited loss rates and higher diffusion-limited loss rates with increasing mass, the timing of surface desiccation varies: the 1 $M_\oplus$ planet has some surface water until ∼3 Gyr, while the 8 $M_\oplus$ becomes desiccated before even 1 Gyr. Further, the effect of surface gravity on mantle water inventory is visible near the beginning of the deep-water cycling period, where it is clear that more water becomes sequestered in the mantle with increasing planetary mass. However, this water does not change the final outcome of complete desiccation for all four simulated planets.

resent planets that began the simulations with less water than they would naively be expected to lose, and so would become desiccated without a deep-water cycle (see Table 3.1), but through our coupled modelling approach, these planets are in a habitable surface water regime by 5 Gyr. Although loss roughly increases with planetary mass, there are still survivors for the most massive planets simulated, but more simulations become desiccated as planetary mass is increased. Regardless, over half of the simulated planets in Fig. 4.6 are in a habitable, Earth-like surface water regime by 5 Gyr. Although more planets become desiccated in Fig. 4.6 than in Fig. 4.4, more planets also remain habitable throughout the 5 Gyr simulations. It appears then that, all else remaining the same, initiating planets with the same mass of water leads to habitable surface conditions much more often than when planets are initiated with water inventories scaled to their mass, i.e., the same water mass fraction.

4.4 Discussion

We have extended the 1 $M_\oplus$ models of Moore & Cowan (2020) and Moore et al. (2023) to investigate water evolution on super-Earths ranging from 2 $M_\oplus$ to 8 $M_\oplus$. We briefly describe additional mass-dependent parameters in our model. Many aspects, although important, are not feasible for implementation within a 0-D box model, and as such, should be further explored in future studies. We merely provide examples of other mass dependencies within the model without providing an exhaustive list.

Planetary parameters within our model, such as mantle thickness $h(M_\mathrm{p})$ and surface gravity $g(M_\mathrm{p})$, along with the thermal evolution are calculated using the Valencia et al. (2006) scaling relations, assuming a "bulk silicate Earth" composition

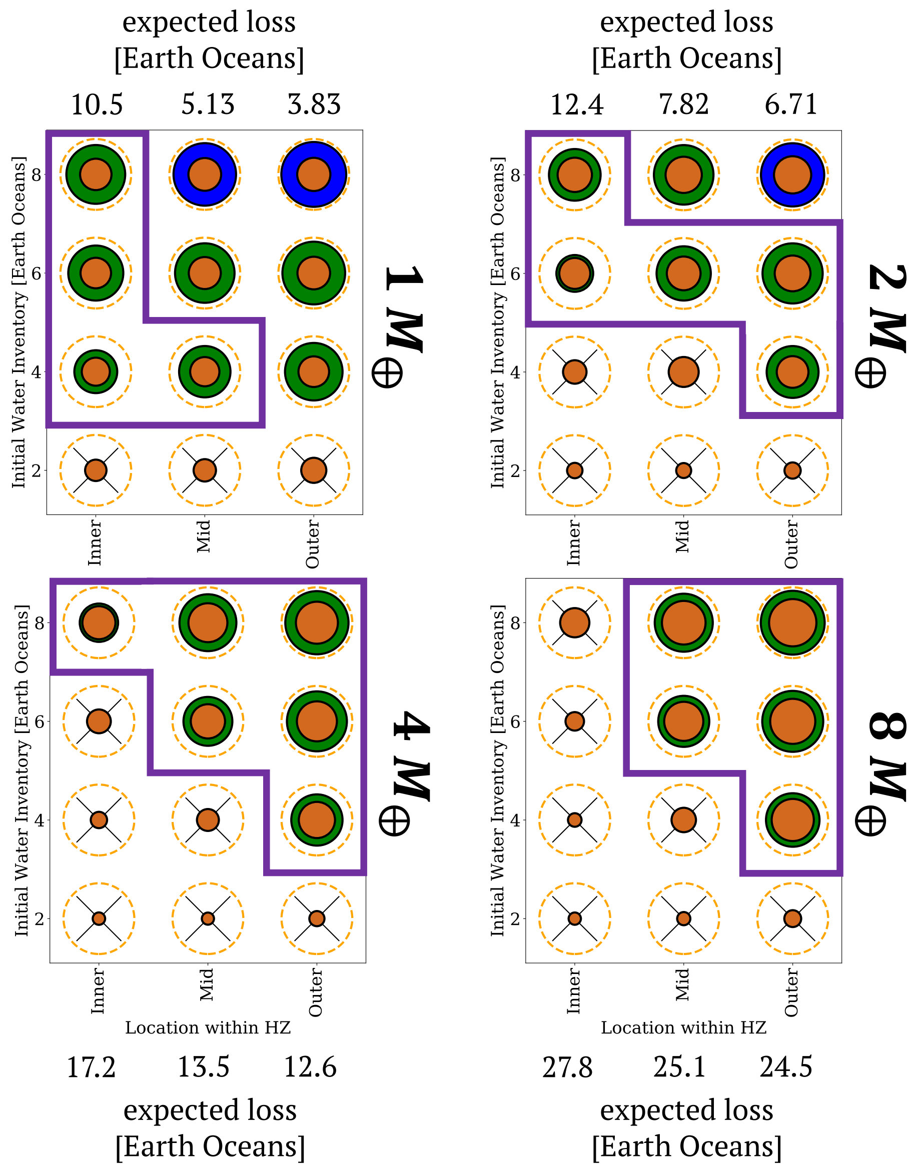

Figure 4.6: Same as Fig. 4.4, but initializing planets with the same water mass instead of the same water mass fraction. Planets that were initiated with less water than they were expected to lose are again surrounded by purple boxes to indicate habitable "survivors" due to the coupled model. As mass is increased, more planets have desiccated surfaces by 5 Gyr; both the number of waterworlds and habitable planets decrease.

(Schaefer & Sasselov 2015; also see Eqn. (A1) of Moore & Cowan 2020) and assumes the same layering as Earth — surface, mantle, core. The higher internal pressures and temperatures of super-Earths will probably lead to different heat fluxes than included in our Earth-dependent model, and could result in additional reservoirs due to a different internal structure. A different planetary internal structure would lead to different solidus/liquidus curves within the interior. Note, however, that we calculate the wet solidus temperature accounting for its depression due to the incorporation of water (Katz et al. 2003).

The length of mid-ocean ridges, $L_{\mathrm{MOR}} = 3\pi R_{\mathrm{p}}$, will increase with increasing M_{p}. The related mid-ocean spreading rate, $S(T_{\mathrm{m}})$, is a function of mantle temperature, which should cool slower for more massive planets. However, this rate is also dependent on the mantle thickness and surface gravity. The degassing and regassing rates are directly impacted through their dependence on seafloor pressure, P, and mantle temperature, T_{m}, and their effect on water evolution is visualized in Fig. 4.2 and Fig. 4.5. The temporal water evolution results of these two figures allow us to compare water cycling rates, loss rates, and water partitioning for different M_{p}, as well as compare results when beginning all simulations with the same initial water mass fraction or with the same initial water inventory, in units of Earth Oceans. Energy-limited loss was expected to decrease with increasing mass, and diffusion-limited loss was expected to increase with increasing mass. Both of these behaviours are apparent in Figs. 4.2 and 4.5. Because of the longer duration of diffusion-limited loss, the amount of water lost should increase with increasing M_{p}, when considering the same initial water inventory for all planets; indeed, we see this in Fig. 4.6. This behaviour is still apparent in the water mass fraction simulations of Fig. 4.4, albeit less intuitive due to the amount of initial water becoming larger for more massive planets.

The magma ocean water partition coefficient D controls the amount of water partitioned between solid mantle and the magma ocean as the magma ocean solidifies from the bottom–up. As expected, increasing this value — as would be expected with increasing mass — leads to more substantial water sequestered in the solid mantle during the magma ocean phase, as shown in Fig. 4.3. Further, due to the higher surface gravity of super-Earths, more water becomes sequestered (and potentially trapped) within the solid mantle during deep-water cycling with increasing mass. Because of this, less of the total water inventory may be lost to space than expected, but at the cost of sequestered water being of little to no help to a diminishing surface water inventory.

Importantly, however, as its name implies, the magma ocean water partition coefficient D only governs water partitioning during the magma ocean phase. The amount of water present within the solid mantle by 5 Gyr is nearly identical regardless of D due to the short lifetime of the magma ocean compared to the much longer deep-water cycling phase, so varying D has nearly no effect on the final planetary water inventories, their surface water regime, and habitability prospects. A higher $D = 0.2$ was chosen to mimic a basal magma ocean by Moore et al. (2023), and the resulting rapid degassing seen in Fig. 4.3 occurs due to the exemption of a parameterized constant injection from basal magma ocean to solid mantle during deep-water cycling.

Our parameter space exploration allows us to compare the results for four initial water mass fractions/four initial water inventories, three orbital distances, and four planetary masses. Fig. 4.4 shows that, when considering the same water mass fraction, more massive planets are likely to avoid surface desiccation and become uninhabitable waterworlds with substantial water inventories trapped in their mantle. Fig. 4.6, instead initializing all planets with 2 to 8 Earth Oceans, provides a clear picture that surface habitability prospects are reduced as planetary mass is increased due to the enhanced diffusion-limited loss during deep-water cycling, but mainly because more water becomes sequestered in the solid mantle. Still, 13/48 of the super-Earth simulations in Fig. 4.4 and half of the simulations in Fig. 4.6 end in a habitable, Earth-like surface water regime. Based on our current box model and our parameter space exploration, it seems that 1 $M_{\oplus}$ may still be the sweet spot for surface habitability in the face of water loss to space.

We initiate every deep-water cycling simulation with the same solid mantle temperature of $T_{\mathrm{m},0} = 3000$ K. This value should scale with planetary mass, and a hotter mantle would presumably lead to more intense early degassing during deep-water cycling and, if the mantle remains hydrated, an extended period of plate tectonics (if plate tectonics begins at all on super-Earths, see, e.g., Korenaga 2010; Foley et al. 2012). We can estimate $T_{\mathrm{m},0} = 4880$ K for an 8 $M_{\oplus}$ planet by extrapolating Table 5 of Schaefer & Sasselov (2015). Using this as the initial solid mantle temperature for deep-water cycling indeed leads to more early degassing in our model, which slightly offsets the amount of water loss to space for a period; however, the final water inventories and partitioning remain unchanged by 5 Gyr regardless of $T_{\mathrm{m},0}$. Indeed, as noted by Schaefer & Sasselov (2015) and McGovern & Schubert (1989), the effect of initial mantle temperature is minimal after a few hundred Myrs.

Our model is restricted to the plate-tectonic mode, although it is likely that super-Earths are instead in a stagnant lid regime similar to modern-day Venus, especially if surface oceans are not formed through magma ocean degassing (O'Neill & Lenardic 2007; Miyazaki & Korenaga 2022). The potentially exotic internal structure of super-Earths may be what locks the planet into a stagnant lid mode and could provide further water reservoirs beyond what is represented within our box model. However, we leave these improvements to future model iterations.

Acknowledgments

KM and NBC thank the Trottier Space Institute at McGill and the Trottier Institute for Research on Exoplanets (iREx).

Data Availability

The models and data presented within this manuscript are available from the corresponding author at reasonable request.

Interlude III

This chapter describes the influence of planetary mass on surface water inventories of terrestrial planets, which may have their atmospheres eroded or become desiccated through interaction with their host M-dwarf star. While much of the initial data analysis was performed by Benjamin David and Albert Yian Zhang, I took the lead in running the simulations presented within this manuscript, analyzing the final results, creating the figures, and writing the manuscript itself. Although this chapter has not been submitted to a journal, it is in preparation and will be submitted for peer review by end of year.

Collectively, the three chapters presented within this dissertation provide robust first-order predictions for the habitability of terrestrial planets orbiting M-dwarfs through temporal evolution of surface and interior water inventories. Further improvements, such as increasing the model's dimensionality and tracking additional volatiles, are left to future work.

Chapter 5

Discussion and Conclusion

This thesis began from a simple question: can water stored in a planetary mantle restore habitable surface conditions on highly-irradiated terrestrial planets orbiting M-dwarfs? Using a coupled model combining stellar evolution and atmospheric loss with geophysical cycling, the chapters of this thesis have explored the water inventories — especially the surface water, a requirement for habitability — of M-dwarf terrestrial planets with progressively more complexity. The overall results support the idea that geophysical cycling during various stages of a terrestrial planet's lifetime — including the early, concurrent runaway greenhouse/surface magma ocean phase and the plate-tectonics mediated deep-water cycling period — can substantially reduce the amount of water lost to space, sometimes making the difference between a desiccated planet and an Earth-like, habitable surface with oceans and exposed continents. Further, depending on how exactly water is delivered to terrestrial planets, more massive planets tend to sequester and trap significant water within their mantle, usually to the detriment of surface habitability. This final mass-dependent study brings the project full circle with the those that formed the basis of this thesis: Cowan & Abbot (2014), Schaefer & Sasselov (2015), and Komacek & Abbot (2016). Indeed, this thesis posits that the negative habitability prospects for terrestrial planets around M-dwarfs often seen in the literature has been overstated; these abundant planets are more likely to be habitable than previously thought.

5.1 Model Limitations & Future Model Improvements

The question of habitability is and will continue to be an ongoing debate in planetary science due to the many-dimensional, high-complexity nature of the definition of habitability. Because of this, there are multiple avenues for future improvement and continuation of this work, whether by myself or others. Our box model neglects many details due to its simple zero-dimensional presentation, focusing solely on the cycling of water between planetary reservoirs and its loss to space. However, some stochastic processes are neglected for further simplicity: young M-dwarfs are not only temporally active, but can emit sporadic flares and superflares capable of stripping large portions, or sometimes the entirety, of the atmosphere (Loyd et al. 2018; Yamashiki et al. 2019; Howard et al. 2020). The impact of flares (and atmospheric loss in general) could potentially be mitigated by a planetary magnetic field, such as the one generated by Earth today. Interestingly, it has been recently noted that stellar flares could lead to planetary interior heating; volcanism and outgassing could then potentially mitigate flare-associated atmospheric erosion (Grayver et al. 2022).

Impact-driven loss, as well as volatile delivery by impacts, is another stochastic process that may be important, and could be low-hanging fruit for a future model iteration. Indeed, Childs et al. (2022) focus on the delivery of volatiles by asteroid impacts and determine that gas giant planets are required to stabilize an asteroid belt during planet formation. However, based on observations of M-dwarf systems, there seems to be a lack of giant planets in multi-planet systems with terrestrial planets, e.g., TRAPPIST-1, and although stable asteroid belts may be possible, the origin of life through asteroid delivery is probably unlikely. A magma ocean may also be created following a giant impact, as occurred on Earth following the Moon-forming impact.

A clear path forward is to increase the model dimensionality to 1-D, 2-D, or in the long-term, 3-D. Increasing the dimensionality would resolve the internal structure of planets; the magma ocean water partition coefficient, D, could then be treated as a function of internal pressure, with low values in the lower and upper mantle, but high values in the transition zone which can — and does — hold onto a lot of water. Further, this improvement would allow the model to account for alternate tectonic modes, such as the non-mobile, single-plate stagnant lid (Reese et al. 1998; O'Neill & Lenardic 2007; Noack & Breuer 2014), which may be the most common state for terrestrial planets and currently exists on nearby Venus and Mars. A stagnant lid would significantly alter the cycling parameterization, effectively making cycling in one direction more efficient: degassing through volcanism may be unaffected, but regassing would be much slower through processes such as volcanic resurfacing. It would then be important to determine when the stagnant lid forms and how long it persists, either with a magma ocean below the lid, a solid mantle, or a combination of the two. Continued degassing would imply a steady state where the majority of volatiles end up in the atmosphere (Spaargaren et al. 2020), i.e., water may not be retained in the interior; this could be beneficial for super-Earths, for which our modelling indicates that too much water is soaked up in the mantle.

Creating an M-Earth model for a stagnant lid mode would provide comparison with the plate-tectonics M-Earth model presented within this thesis. Alternatively, to implement this idea into our 0-D box model, we could treat the lifetime of the stagnant lid as a free parameter which would permit an additional transition in our model: the M-Earth would begin in a surface magma ocean phase, transition to a Myr/Gyr-lived stagnant lid, before allowing the lid to become mobile, initiating plate-tectonics-mediated deep-water cycling. This would effectively represent what is thought to be the Earth's geophysical history, although the exact timing of the initiation of plate tectonics is hotly debated (Langmuir & Broecker 2012; Debaille et al. 2013; Bédard 2018). Since there are many factors influencing plate tectonics (e.g., rock hydration, mantle rheology, mantle/surface temperatures, planetary size; see Spaargaren et al. 2020), a parameterized transition between regimes, void of any free parameters, may be exceedingly difficult to model without extending our model to 2-D or 3-D like stagnant lid models investigating habitability within the literature (e.g., Foley & Smye 2018; Dorn et al. 2018a,b).

An improvement that could be made in concert with the above is accounting for different reservoirs — such as surface ices, or the mantle transition zone "sink" (Hirschmann 2006; Hirschmann & Kohlstedt 2012) – and/or different atmospheric and planetary compositions. For example, higher internal pressures may lead to exotic mantle compositions in super-Earths, potentially providing additional reservoirs for water and other volatiles. However, accounting for CO_2 may be required first, since interior water solubility and atmosphere/surface equilibrium are functions of a combined CO_2-H_2O system as well as internal pressure (Papale 1997, 1999). Since solubility will tend to decrease with decreasing temperature, within our box model we underestimate solubility early in the surface magma ocean phase, and overestimate it as the surface magma ocean cools (Salvador & Samuel 2023). Further, atmospheric carbon dioxide should be gradually removed to form carbonates, regulating the planetary climate through the carbonate-silicate cycle (see Fig. 1.2).

Planets on very close orbits may become tidally-locked to their host star, which could prolong habitability through climate stabilization due to clouds (Yang et al. 2013; Shields et al. 2016). Tidal heating (whether by the host star, or by other planets, such as in the seven-planet TRAPPIST-1 system) could increase volcanic activity, prolong the concurrent magma ocean/runaway greenhouse phase, or drive plate tectonics on a cooled planet, i.e., one without internal heating (e.g., Shields et al. 2016; Barnes 2017; McIntyre 2022). This is especially important for the closest orbiting planets detected, which are the prime targets for ongoing studies and observations with the James Webb Space Telescope (JWST).

It should be noted that most magma ocean studies focus specifically on oxidized species (particularly, H_2O and CO_2) and their effect on the degassing of an atmosphere (e.g., Elkins-Tanton 2008; Lebrun et al. 2013; Hier-Majumder & Hirschmann 2017; Barth et al. 2021). The redox state of the interior (i.e., the oxygen fugacity) will control the composition and degassing rate of the atmospheric volatiles (Grott et al. 2011; Dehant et al. 2019), with more reduced mantles producing H_2- or CO-rich atmospheres (Schaefer & Fegley 2010). The oxygen fugacity of the mantle will also have important effects on deep-water cycling, especially with respect to water storage within the mantle. Bower et al. (2022) find that decreasing oxygen fugacity significantly increases the degassing rate and allows more rapid cooling — the former potentially increasing the amount of water lost to space, while the latter could increase water retention within the interior at earlier times — and that an atmosphere is able to transition between redox states as the surface magma ocean cools. However, Bower et al. (2022) also note that fractional crystallization of a surface magma ocean — i.e., precipitated solids will be removed from the melt through, e.g., gravitational settling, forming the underlying solid mantle, and commonly assumed in magma ocean studies (e.g., Elkins-Tanton 2008, Hamano et al. 2013, Lebrun et al. 2013, Schaefer et al. 2016) — will produce oxidized atmospheres which are H_2O-rich, supporting a critical assumption of our parameterized surface magma ocean model. The redox states of a terrestrial planet's interior, surface, and atmosphere are extremely important and should be included in future coupled models.

Schaefer et al. (2016) note that following surface magma ocean solidification, the majority of the water inventory should be stored in the mantle for planets with low water abundances. Although we assume the basal magma ocean within our model is a substantial reservoir for water after being isolated from the surface, a "wet basal magma ocean" may in fact be contradictory; it is more likely that a *dry* magma ocean enriched in iron would be required for the existence of a basal magma ocean (L. Noack, priv. comm.). An alternative mechanism, instead of a residual basal magma ocean remaining below a solid mantle, may exist to sequester water away from the surface and loss to space. It is possible that, as the surface magma ocean cools, a crust may form at the surface, isolating the interior magma ocean from the atmosphere. This could also be represented with the basal ocean box model shown in Fig. 3.1(c), albeit with "solid mantle" replaced with "crust", and "basal magma ocean" replaced simply with the now-isolated magma ocean. In this scenario, it is possible that ∼10% of the magma could remain isolated below the crust (L. Noack, priv. comm.), conserving a significant amount of water. Indeed, a magma ocean may solidify from both the bottom and top depending on the composition of the melt. Other reservoirs exist within the Earth which may lock-in and gradually release water, such as the mantle transition zone (e.g., Hirschmann 2006; Guimond et al. 2023) and the liquid outer core. Therefore, the basal magma ocean within our model could also represent volatiles sequestered in the core. Indeed, the style of magma ocean — whether surface or basal — impacts the partitioning of volatiles throughout the planet's core, mantle, and atmosphere (e.g., Grewal et al. 2022, who refer to "external" and "internal" magma oceans during Solar System terrestrial planet formation, respectively).

Recent literature appears to disfavour Ribas et al. (2005) which used solar analogs to model XUV, but did not model the exact ionizing flux in the XUV range of 0.1–120 nm. Howe et al. (2020) find a better estimate of XUV flux but also use solar analogs, while Melbourne et al. (2020) predicted UV emission from M-dwarfs using Ca II and Hα emission lines. King & Wheatley (2021) determined the decline in stellar extreme UV is much slower than X-rays (with $\beta_X \approx -1.18$), such that the total combined XUV emission of stars mostly occurs after the saturated phase. The results of Fleming et al. (2020) disfavour $t_{\rm sat} \leq 1$ Gyr, instead suggesting $t_{\rm sat} \gtrsim 4$ Gyr for loss from planets orbiting ultracool dwarfs; indeed, Birky et al. (2021) find saturation times of ∼3–5 Gyr for TRAPPIST-1. Regardless, since we test various host stars spanning the M-stellar class, we adopted the Ribas et al. (2005) prescription of $t_{\rm sat} = 1$ Gyr. As such, our results could underestimate energy-limited escape rates if the XUV saturation timescale is different between host stars.

5.2 Complementary Studies

There have been various complementary studies, with interesting and related results, published during the research project detailed in this thesis. Some of these studies include a few of the aforementioned model improvements, with evidence supporting our overall hypothesis of enhanced habitability prospects for rocky planets orbiting M-dwarf stars when combining geophysical cycling with atmospheric loss, compared to the bleak outlook previously seen within the literature.

Krissansen-Totton & Fortney (2022) coupled atmosphere-interior evolution of the TRAPPIST-1 planets from (surface) magma ocean through to deep-water cycling, including atmospheric loss, for a substantially larger parameter space (21 model parameters are varied), building on their highly-coupled model (Krissansen-Totton et al. 2021b). The results of Krissansen-Totton et al. (2021b) indicated that initial conditions can change Earth's evolutionary pathway: it may be permanently stuck in a runaway greenhouse, or become a waterworld or a Dune planet (see Fig. 4.1). Krissansen-Totton et al. (2021a) find two states for Venus, a terrestrial planet interior to the Solar System habitable zone: either Venus was never habitable, or experienced several Gyr of habitability.

Krissansen-Totton & Fortney (2022) then focused on TRAPPIST-1, and use the measured stellar parameters of the host star (Birky et al. 2021) to determine the redox state and composition of each of the seven rocky planets' atmospheres. The authors' primary concern is oxygen build-up through hydrogen loss, and hence the model tracks volatile partitioning/fluxes of H_2O and CO_2 along with O_2 buildup. The model of Krissansen-Totton & Fortney (2022) includes processes and aspects currently beyond the scope of our model, such as crustal oxidization and a radiative-convective climate model, while varying initial water inventory from 0.7–300 Earth Oceans, accounting for substantial atmospheric CO_2 and carbonate weathering, and varying other parameters which we hold constant such as the planetary albedo. In doing so, the authors thoroughly investigate the habitability prospects of the TRAPPIST-1 planets. The results are promising for M-dwarf rocky planet habitability, indicating that some of the planets can build up CO_2 or CO_2-O_2 atmospheres with a non-JWST-detectable amount of water vapour, and that some planets, such as TRAPPIST-1e and 1g, may have liquid surface oceans at the present day. The results of Krissansen-Totton & Fortney (2022) support the potential habitability of terrestrial planets orbiting M-dwarf stars. Recent formation simulations for planets orbiting G- and M-dwarf stars indicate even larger water inventories, with $\sim$100–800 Earth Oceans of water available to M-dwarf terrestrial planets, depending on the ^{26}Al content of the star-planet system (Lichtenberg et al. 2019).

Seales & Lenardic (2021) created a water cycling model that aims to determine the temporal habitability throughout a planet's evolution. The authors find that deep-water cycling and planetary habitability is strongly dependent on tectonic mode and efficiency of tectonic cooling, the latter of which we hold fixed throughout the model presented in this thesis. Further, the authors determine that, due to the strong dependence on tectonic mode, an uninhabitable planet may become habitable later in its lifetime, similar to the initial hypothesis of this thesis, but the timing of the onset of habitable surface conditions may vary by Gyrs. Interestingly and importantly, however, Seales & Lenardic (2021) neglect atmospheric loss which, as shown in this thesis, would impact the results. Their study provides a complementary result to this thesis, investigating an aspect limited by our own modelling approach.

Bonney & Kennefick (2022) instead neglect the deep-water cycle, and use VPLanet simulations to investigate the liquid surface water inventory, and potential desiccation, of three Earth-like TESS targets orbiting M-dwarf hosts ∼1 Gyr after their formation, chosen based on the highly active early flaring & XUV-emitting period of M-dwarfs. VPLanet is another coupled model of atmosphere-surface-interior evolution independent of our model in the current study (Barnes et al. 2020). Of the three targets, one always becomes desiccated, one has a ∼50% chance of desiccation, and one retains surface water. The different modelling approach presented by Bonney & Kennefick (2022), lacking a deep-water cycle but accounting for tidal effects, and an initial water inventory of 10 Earth Oceans for all simulated cases, precludes direct comparison with our results, but the overall qualitative conclusions are similar: the habitability of terrestrial planets orbiting M-dwarf hosts is strongly dependent on the planet's stellar environment, which affects the retention of liquid surface water through irradiation-induced water loss, and these planets may become desiccated or remain habitable throughout their lifetime. Indeed, the above two studies support the importance of a completely coupled model of deep-water cycling and water loss to space.

Li et al. (2022) find two stable magnesium hydrosilicates at the high pressures indicative of the early basal magma ocean on Earth, which may have contained up to 11.4 wt% water. Since magnesium hydrosilicates are likely the water carriers within the Earth's upper mantle and transition zone today, these would have contributed significantly to Earth's water budget throughout its lifetime. Substantial water would have been released to the surface and mantle when these hydrosilicates decomposed

$\sim$30 Myr after formation, hiding up to 8 Earth Oceans in the deep interior. This would also extend to super-Earths, which may contain these large Mg-hydrosilicate reservoirs throughout their histories in their high-pressure mantles. Cowan & Abbot (2014) found that a terrestrial planet will have exposed continents (critical for climate stabilization through the carbonate-silicate cycle) for water mass fractions $\lesssim 0.2\%$. With the significantly higher 11.4 wt.% reservoir of Li et al. (2022), then, super-Earths should be able to sustain much higher water inventories without surface inundation, which may result in a large field of potentially habitable terrestrial planets.

In a separate study, Guimond et al. (2023) explore the mantle mineralogy of Earth-like and super-Earth planets to determine the mantle water storage, a typical uncertainty in the literature, and find that larger planets will have smaller mantle water capacities due to the transition zone which causes a bottleneck in water transport. However, the water budgets of these planets indicate that the surface magma ocean will be water-saturated, and oceans may condense immediately following its solidification. While this is a benefit for our treatment of surface water as a proxy for habitability, it may preclude the presence of land and topography, which could negatively impact the climate and its stability due to the lack of a carbonate-silicate cycle akin to the Earth (see Fig. 1.2). It should be noted that our "box model" parameterization assumes a 0-D mantle with average values for water capacity and mantle temperature instead of directly modelling separate reservoirs within the mantle itself. Regardless, the results of Guimond et al. (2023) are important for future studies and provide a starting point for deep-water cycling.

A recent study by Dorn & Lichtenberg (2021) focused on water which can be hidden within planets that experience an early surface magma ocean phase. The authors note that water may be chemically produced during the magma ocean stage through redox reactions involving primordial hydrogen and the magma ocean; this is especially important if accretion and/or delivery of water to the planet is insufficient (as noted by, e.g., Childs et al. 2022). The authors also find that water partitions most efficiently of all considered volatile species within their model when mixing within the magma ocean. For this reason, magma oceans can be huge reservoirs for large amounts of water — supporting our initial condition of beginning with all water dissolved in the surface magma ocean — which can provide robust protection against atmospheric loss during this (potentially long-lived) stage.

Emphasizing the extended runaway greenhouse phase of terrestrial planets orbiting M-dwarfs, Yoshida et al. (2022) focus on hydrodynamic escape of an H_2-H_2O atmosphere for a 1 $M_\oplus$ M-Earth, assuming a 0.1 Gyr runaway greenhouse duration, longer than many of our tested cases in Table 3.1. By accounting for radiative cooling of H_2O and its byproducts — an aspect of escape beyond the scope of this thesis — the authors find that the atmospheric escape rate is suppressed compared to escape from a pure H_2 atmosphere. The timescale of H_2 escape is found to be longer than the runaway greenhouse for the tested planets, so retained water may form surface oceans during temperate conditions. Although the deep-water cycle is again neglected, the authors determine that enough water may be retained following the end of runaway greenhouse for surface oceans to condense, providing additional support for the potential habitability of terrestrial planets around M-dwarf stars.

A study by Johnstone (2020) focused on the chemical, thermal, and hydrodynamical processes governing escape of water from the upper atmosphere of planets with water-dominated atmospheres, for planets orbiting within the habitable zone of highly active stars. Higher stellar activity will result in enhanced photodissociation and escape of both hydrogen and oxygen to space. Interestingly, the authors find that atmospheric O_2 buildup is unlikely for an HZ planet around a low-mass M-dwarf, unless water loss continues after the star becomes less active. Indeed, this provides a counterpoint to the negative habitability prospects and extreme water loss rates of e.g., Luger & Barnes (2015), which emphasized the issue of atmospheric O_2 buildup due to photodissociation of water and its loss to space.

Bower et al. (2022) study atmospheres outgassed from magma oceans for terrestrial planets, finding that massive H_2O-CO_2 atmospheres should form. Although the authors consider an Earth-twin planet, they neglect the partitioning of volatiles into the solid mantle, noting that the value is small compared to that in the magma ocean-atmosphere system, a result also found in our analysis. However, Bower et al. (2022) include the escape of hydrogen to space (though neglect photodissociation). For their critical melt fraction of ∼30%, the authors determine that the style of magma ocean convection changes, which could lead to the formation of a surface (stagnant) lid when surface temperature $\lesssim 1650$ K (note, however, that since we fix the surface temperature during runaway greenhouse to $T_{\rm surf} = 1800$ K, we cannot achieve this temperature in our model), sequestering water within the interior and promoting a carbon-rich atmosphere through equilibrium crystallization. This stored water is protected from not only XUV-induced loss during the earliest, most active phase of the host star, but also against impact-driven loss. In contrast, fractional crystallization — as assumed in our surface magma ocean parameterization — could prolong the surface magma ocean and thus promote a water-rich atmosphere instead. Further, Bower et al. (2022) find that increasing the water inventory from 1 to 10

Earth Oceans extends the surface magma ocean lifetime by two orders-of-magnitude; earlier degassing of an atmosphere from the surface magma ocean or a deeper magma ocean would also extend the surface magma ocean solidification timescale (Lebrun et al. 2013). Although we treat the timescales of runaway greenhouse and magma ocean solidification as one-and-the-same, it is possible to self-consistently determine the latter using higher-complexity models.

The timescale of loss to space is shown to have a critical impact on surface water, and thus planetary habitability, in the three manuscripts presented within this thesis. Kodama et al. (2015) find a somewhat contrary result through modelling water loss for various initial water inventories and orbital distances of Earth-sized planets orbiting Sun-like stars. The authors find that rapid water loss can transition an Earth-like planet to a Dune planet (Abe et al. 2011; also see Fig. 4.1) with $\sim$0.05 Earth Oceans on its surface, which would actually extend the period of planetary habitability. This result is similar to our sequestered mantle water hypothesis but through a different mechanism that avoids surface desiccation. Predictably, this outcome is more likely for planets with lower initial water inventories. Moreover, Katyal et al. (2020) study atmospheric escape from a terrestrial planet during the surface magma ocean phase, and note that diffusion-limited escape may be dominant during this highly irradiated early phase instead of energy-limited, the latter of which we assume throughout this thesis. Adopting diffusion-limited escape for the duration of our simulations would lead to a significantly lower amount of water lost by 5 Gyr, so long as the thermospheric temperature remained low enough that the diffusion-limited rate did not exceed the energy-limited rate.

5.3 Observational Prospects

The M-dwarf opportunity (Charbonneau & Deming 2007) indicates that M-dwarf planets are prime targets for ongoing observation and characterization; indeed, the James Webb Space Telescope (JWST) is observing many M-dwarf planets. Although the model in this thesis theoretically predicts the existence and persistence of surface water on terrestrial planets around M-dwarf stars, this can be tested *right now* using JWST transit spectra.

Uninhabitable atmospheres will be detectable this decade, with a few potential habitable atmosphere detections as well (Krissansen-Totton 2023). Indeed, two TRAPPIST-1 planets have already been observed in thermal emission with JWST. TRAPPIST-1b, the closest orbiting planet and the most susceptible to substantial atmosphere erosion, was determined to be lacking any significant atmosphere (Greene et al. 2023). Further, TRAPPIST-1c, the next closest planet, was also found to be absent of an atmosphere, although one may exist that is extremely tenuous (Zieba et al. 2023). Because of its unique seven-rocky-planet structure, the TRAPPIST-1 system is a prime target for present and upcoming studies — especially for habitable zone planets TRAPPIST-1d and e — providing insight into the stellar environment around M-dwarf host stars and its impact on orbiting planets, some of which may be presently orbiting in the habitable zone. Other ideal M-dwarf habitable zone targets include TOI-700 d (Gilbert et al. 2020) and TOI-700 e (Gilbert et al. 2023).

Regardless, it will be difficult to unambiguously observe and characterize the atmospheric composition of terrestrial exoplanets in the near-future (for a more extensive overview of observational challenges, see Shields et al. 2016 and Paradise et al. 2022). Moreover, unambiguous observations of the geophysical aspects of our predictive model are even further away, although strong volcanic activity has been recently inferred for the temperate super-Earth LP 791-18d (Peterson et al. 2023). Even with JWST, molecules will require a minimum concentration of ∼100 ppm to be detectable (Krissansen-Totton et al. 2019; Sousa-Silva et al. 2020). The detection of atmospheric water alone will not itself establish a planet's habitability, although we treat the presence of persistent liquid surface water as such throughout this thesis. It is also important to note that since there are many possible climate states for Earth-like planets orbiting a variety of host stars, it may be difficult to detect surface water directly through spectral observations, although there will be some statistical connection (Paradise et al. 2022).

There are other challenges with linking theoretical predictions to observations. Most models of terrestrial planets presume a dry, solid interior underlying a steam atmosphere; however, assuming a liquid magma ocean below the atmosphere would increase the observed radius of a terrestrial planet by ∼5% (Bower et al. 2019; Dorn & Lichtenberg 2021). Since the steam atmosphere would preferentially dissolve into the magma ocean, assuming a wet melt-solid interior would instead decrease R_p. This may lead to up to one order-of-magnitude discrepancies in inferred water budgets from observations (Dorn & Lichtenberg 2021), although this may not be an issue for terrestrial planets currently in the habitable zone of their host M-dwarf.

Although we focus solely on a pure water atmosphere (including an early steam atmosphere), Bower et al. (2022) note that steam atmospheres may be less ubiquitous in terrestrial planets than assumed in the literature, and state that a focus on other atmospheric components may be the logical next step in studying the atmospheric evolution of terrestrial planets. Moreover, waterworlds can provide oxygen false positives when initiated with 10s-100s of Earth Oceans (Krissansen-Totton et al. 2021b), but this ambiguity may be distinguished if exposed continents can be observed (Cowan et al. 2009).

5.4 Conclusion

The prospect of life on a planet other than Earth has long fascinated academics and non-academics alike. Although we may still be many years from unambiguous detection of extraterrestrial life, we can study many aspects and processes governing the definition of "habitable conditions" on rocky planets much like our own, but orbiting smaller M-dwarf stars. Theoretical predictions can be used to guide present and upcoming studies, and in the future, these models will become interpretative. The study of planetary habitability, especially rocky planets similar to the Earth, is important and requires collaboration between the astronomy and planetary science communities, as well as collaboration between theorists and observers.

In this thesis, I have presented three manuscripts — two published and one in-preparation — exploring the surface water on and water partitioning of terrestrial planets orbiting M-dwarf stars using models of increasing complexity. We first determined, using parameterized atmospheric loss, that water sequestered in a planetary mantle through geophysical deep-water cycling can be degassed to recover habitable conditions on a desiccated surface once the activity of the host decreases as the star-planet system evolves. Next, we found that water may be protected from the most significant period of loss to space through dissolution in a magma ocean, and that a short-lived residual basal magma ocean can maintain surface habitability. Through coupling of stellar evolution, water loss to space, and water exchange between surface and interior, we found that the amount of water lost to space was substantially lower than previous extreme estimates within the literature. Finally, we explored the impact of planetary mass on water and its partitioning. Depending on the treatment of initial water inventory, more massive planets either become uninhabitable waterworlds or sequester significant water in their mantle below desiccated surfaces. This thesis hence supports continued study of the habitability of terrestrial planets around M-dwarf hosts, prime targets for observations with, e.g., the James Webb Space Telescope. Moreover, this thesis emphasizes the importance of coupling geophysics, atmospheric science, and astronomy to investigate the many-faceted question of terrestrial planet habitability, especially around young, active host stars whose planets will be susceptible to immense atmospheric loss to space and, potentially, surface desiccation.

References

Abbot, D. S., Cowan, N. B., & Ciesla, F. J. 2012, ApJ, 756, 178

Abe, Y. 1993, Lithos, 30, 223

Abe, Y., Abe-Ouchi, A., Sleep, N. H., & Zahnle, K. J. 2011, Astrobiology, 11, 443

Airapetian, V. S., Glocer, A., Khazanov, G. V., et al. 2017, ApJ, 836, L3

Alibert, Y. 2014, A&A, 561, A41

Anglada-Escudé, G., Amado, P. J., Barnes, J., et al. 2016, Nature, 536, 437

Baraffe, I., Homeier, D., Allard, F., & Chabrier, G. 2015, A&A, 577, A42

Barnes, R. 2017, Celestial Mechanics and Dynamical Astronomy, 129, 509

Barnes, R., Deitrick, R., Luger, R., et al. 2016, arXiv e-prints, arXiv:1608.06919

Barnes, R., Luger, R., Deitrick, R., et al. 2020, PASP, 132, 024502

Barth, P., Carone, L., Barnes, R., et al. 2021, Astrobiology, 21, 1325

Batalha, N. M., Borucki, W. J., Bryson, S. T., et al. 2011, ApJ, 729, 27

Bédard, J. H. 2018, Geoscience Frontiers, 9, 19

Bercovici, D., & Karato, S.-i. 2003, Nature, 425, 39

Birky, J., Barnes, R., & Fleming, D. P. 2021, Research Notes of the American Astronomical Society, 5, 122

Blanc, N. A., Stegman, D. R., & Ziegler, L. B. 2020, Earth and Planetary Science Letters, 534, 116085

Bolmont, E., Selsis, F., Owen, J. E., et al. 2017a, MNRAS, 464, 3728

—. 2017b, MNRAS, 464, 3728

Bonfils, X., Astudillo-Defru, N., Díaz, R., et al. 2018, A&A, 613, A25

Bonney, P., & Kennefick, J. 2022, Planetary Science Journal, 3, 202

Boukaré, C. E., Parman, S. W., Parmentier, E. M., & Anzures, B. A. 2019, Journal of Geophysical Research (Planets), 124, 3354

Boukaré, C. E., & Ricard, Y. 2017, Geochemistry, Geophysics, Geosystems, 18, 3385

Boukaré, C. E., Ricard, Y., & Fiquet, G. 2015, Journal of Geophysical Research (Solid Earth), 120, 6085

Boukrouche, R., Lichtenberg, T., & Pierrehumbert, R. T. 2021, ApJ, 919, 130

Bower, D. J., Hakim, K., Sossi, P. A., & Sanan, P. 2022, Planetary Science Journal, 3, 93

Bower, D. J., Kitzmann, D., Wolf, A. S., et al. 2019, A&A, 631, A103

Caracas, R., Hirose, K., Nomura, R., & Ballmer, M. D. 2019, Earth and Planetary Science Letters, 516, 202

Chachan, Y., & Lee, E. J. 2023, arXiv e-prints, arXiv:2305.00803

Charbonneau, D., & Deming, D. 2007, arXiv e-prints, arXiv:0706.1047

Charbonneau, D., Berta, Z. K., Irwin, J., et al. 2009, Nature, 462, 891

Childs, A. C., Martin, R. G., & Livio, M. 2022, ApJ, 937, L41

Cowan, N. B., & Abbot, D. S. 2014, ApJ, 781, 27

Cowan, N. B., Agol, E., Meadows, V. S., et al. 2009, ApJ, 700, 915

Cowan, N. B., Greene, T., Angerhausen, D., et al. 2015, PASP, 127, 311

Debaille, V., O'Neill, C., Brandon, A. D., et al. 2013, Earth and Planetary Science Letters, 373, 83

Dehant, V., Debaille, V., Dobos, V., et al. 2019, Space Sci. Rev., 215, 42

Delfosse, X., Forveille, T., Mayor, M., et al. 1998, A&A, 338, L67

Dorn, C., & Lichtenberg, T. 2021, ApJ, 922, L4

Dorn, C., Noack, L., & Rozel, A. B. 2018a, A&A, 614, A18

—. 2018b, A&A, 614, A18

Doyle, A. E., Young, E. D., Klein, B., Zuckerman, B., & Schlichting, H. E. 2019, Science, 366, 356

Dressing, C. D., & Charbonneau, D. 2015, ApJ, 807, 45

Elkins-Tanton, L. T. 2008, Earth and Planetary Science Letters, 271, 181

Ercolano, B., & Clarke, C. J. 2010, MNRAS, 402, 2735

Erkaev, N. V., Kulikov, Y. N., Lammer, H., et al. 2007, A&A, 472, 329

Farihi, J. 2016, New Astronomy Review, 71, 9

Fleming, D. P., Barnes, R., Luger, R., & VanderPlas, J. T. 2020, ApJ, 891, 155

Foley, B. J. 2015, ApJ, 812, 36

Foley, B. J., Bercovici, D., & Landuyt, W. 2012, Earth and Planetary Science Letters, 331, 281

Foley, B. J., & Driscoll, P. E. 2016, Geochemistry, Geophysics, Geosystems, 17, 1885

Foley, B. J., & Smye, A. J. 2018, Astrobiology, 18, 873

France, K., Arulanantham, N., Fossati, L., et al. 2018, ApJS, 239, 16

France, K., Duvvuri, G., Egan, H., et al. 2020, AJ, 160, 237

Franck, S., & Bounama, C. 1995, Advances in Space Research, 15, 79

—. 1997, Physics of the Earth and Planetary Interiors, 100, 189

Gaillard, F., & Scaillet, B. 2014, Earth and Planetary Science Letters, 403, 307

Garcia-Sage, K., Glocer, A., Drake, J. J., Gronoff, G., & Cohen, O. 2017, ApJ, 844, L13

Gilbert, E. A., Barclay, T., Schlieder, J. E., et al. 2020, AJ, 160, 116

Gilbert, E. A., Vanderburg, A., Rodriguez, J. E., et al. 2023, ApJ, 944, L35

Gillon, M., Triaud, A. H. M. J., Demory, B.-O., et al. 2017, Nature, 542, 456

Gillon, M., Meadows, V., Agol, E., et al. 2020, in Bulletin of the American Astronomical Society, Vol. 52, 0208

Gleick, P. H. 1993, Water in crisis: A guide to the world's Fresh Water Resources (Oxford University Press)

Goldblatt, C. 2016, arXiv e-prints, arXiv:1608.07263

Goldblatt, C., Robinson, T. D., Zahnle, K. J., & Crisp, D. 2013, Nature Geoscience, 6, 661

Graham, S. 2010, The water cycle

Grayver, A., Bower, D. J., Saur, J., Dorn, C., & Morris, B. M. 2022, ApJ, 941, L7

Greene, T. P., Bell, T. J., Ducrot, E., et al. 2023, Nature, 618, 39

Grewal, D. S., Seales, J. D., & Dasgupta, R. 2022, Earth and Planetary Science Letters, 598, 117847

Gronoff, G., Arras, P., Baraka, S., et al. 2020, Journal of Geophysical Research (Space Physics), 125, e27639

Grott, M., Morschhauser, A., Breuer, D., & Hauber, E. 2011, Earth and Planetary Science Letters, 308, 391

Guimond, C. M., Shorttle, O., & Rudge, J. F. 2023, MNRAS, 521, 2535

Hakim, K., Bower, D. J., Tian, M., et al. 2020, in European Planetary Science Congress, EPSC2020–58

Hamano, K., Abe, Y., & Genda, H. 2013, Nature, 497, 607

Harsono, D., Persson, M. V., Ramos, A., et al. 2020, A&A, 636, A26

Hart, M. H. 1978, Icarus, 33, 23

Hauri, E. H., Gaetani, G. A., & Green, T. H. 2006, Earth and Planetary Science Letters, 248, 715

Henry, T. J. 2004, in Astronomical Society of the Pacific Conference Series, Vol. 318, Spectroscopically and Spatially Resolving the Components of the Close Binary Stars, ed. R. W. Hilditch, H. Hensberge, & K. Pavlovski, 159–165

Hier-Majumder, S., & Hirschmann, M. M. 2017, Geochemistry, Geophysics, Geosystems, 18, 3078

Hirschmann, M., & Kohlstedt, D. 2012, Physics Today, 65, 40

Hirschmann, M. M. 2006, Annual Review of Earth and Planetary Sciences, 34, 629

Höning, D., Tosi, N., & Spohn, T. 2019, A&A, 627, A48

Howard, W. S., Corbett, H., Law, N. M., et al. 2020, ApJ, 902, 115

Howe, A. R., Adams, F. C., & Meyer, M. R. 2020, ApJ, 894, 130

Hsu, D. C., Ford, E. B., & Terrien, R. 2020, MNRAS, 498, 2249

Huang, S.-S. 1959, American Scientist, 47, 397

Hunten, D. M. 1973, Journal of the Atmospheric Sciences, 30, 1481

Hynes, A. 2001, Earth and Planetary Science Letters, 185, 161

Ikoma, M., Elkins-Tanton, L., Hamano, K., & Suckale, J. 2018, Space Sci. Rev., 214, 76

Ingersoll, A. P. 1969, Journal of the Atmospheric Sciences, 26, 1191

Johnstone, C. P. 2020, ApJ, 890, 79

Johnstone, C. P., Khodachenko, M. L., Lüftinger, T., et al. 2019, A&A, 624, L10

Kasting, J. F. 1988, Icarus, 74, 472

Kasting, J. F., & Holm, N. G. 1992, Earth and Planetary Science Letters, 109, 507

Kasting, J. F., Whitmire, D. P., & Reynolds, R. T. 1993, Icarus, 101, 108

Katyal, N., Ortenzi, G., Lee Grenfell, J., et al. 2020, A&A, 643, A81

Katz, R. F., Spiegelman, M., & Langmuir, C. H. 2003, Geochemistry, Geophysics, Geosystems, 4, 1073

Kimura, T., & Ikoma, M. 2022, Nature Astronomy, 6, 1296

King, G. W., & Wheatley, P. J. 2021, MNRAS, 501, L28

Kite, E. S., Manga, M., & Gaidos, E. 2009, ApJ, 700, 1732

Kodama, T., Genda, H., Abe, Y., & Zahnle, K. J. 2015, ApJ, 812, 165

Komacek, T. D., & Abbot, D. S. 2016, ApJ, 832, 54

Kopparapu, R. K., Ramirez, R., Kasting, J. F., et al. 2013, ApJ, 765, 131

Korenaga, J. 2010, ApJ, 725, L43

—. 2011, Journal of Geophysical Research (Solid Earth), 116, B12403

Korenaga, J., Planavsky, N. J., & Evans, D. A. D. 2017, Philosophical Transactions of the Royal Society of London Series A, 375, 20150393

Krenn, A. F., Fossati, L., Kubyshkina, D., & Lammer, H. 2021, A&A, 650, A94

Krissansen-Totton, J. 2023, arXiv e-prints, arXiv:2306.05397

Krissansen-Totton, J., & Fortney, J. J. 2022, ApJ, 933, 115

Krissansen-Totton, J., Fortney, J. J., & Nimmo, F. 2021a, Planetary Science Journal, 2, 216

Krissansen-Totton, J., Galloway, M. L., Wogan, N., Dhaliwal, J. K., & Fortney, J. J. 2021b, ApJ, 913, 107

Krissansen-Totton, J., Arney, G. N., Catling, D. C., et al. 2019, BAAS, 51, 158

Kruijver, A., Höning, D., & van Westrenen, W. 2021, Planetary Science Journal, 2, 208

Labrosse, S., Hernlund, J. W., & Coltice, N. 2007, Nature, 450, 866

Langmuir, C. H., & Broecker, W. S. 2012, How to Build a Habitable Planet. The Story of Earth from the Big Bang to Humankind - Revised and Expanded Edition (Princeton University Press), doi:10.1515/9781400841974

Lebrun, T., Massol, H., ChassefièRe, E., et al. 2013, Journal of Geophysical Research (Planets), 118, 1155

Lenardic, A. 2018, Philosophical Transactions of the Royal Society of London Series A, 376, 20170416

Li, H.-F., Oganov, A. R., Cui, H., et al. 2022, Phys. Rev. Lett., 128, 035703

Li, Z.-X. A., Lee, C.-T. A., Peslier, A. H., Lenardic, A., & Mackwell, S. J. 2008, Journal of Geophysical Research (Solid Earth), 113, B09210

Lichtenberg, T., Golabek, G. J., Burn, R., et al. 2019, Nature Astronomy, 3, 307

Lichtenberg, T., Schaefer, L. K., Nakajima, M., & Fischer, R. A. 2022, arXiv e-prints, arXiv:2203.10023

Lissauer, J. J. 2007, ApJ, 660, L149

Loomis, R. A., Öberg, K. I., Andrews, S. M., et al. 2020, ApJ, 893, 101

Lopez, E. D. 2017, MNRAS, 472, 245

Lourenço, D. L., Rozel, A. B., Ballmer, M. D., & Tackley, P. J. 2020, Geochemistry, Geophysics, Geosystems, 21, e08756

Loyd, R. O. P., Shkolnik, E. L., Schneider, A. C., et al. 2018, ApJ, 867, 70

Luger, R., & Barnes, R. 2015, Astrobiology, 15, 119

Lustig-Yaeger, J., Meadows, V. S., Tovar Mendoza, G., et al. 2018, AJ, 156, 301

Mayor, M., & Queloz, D. 1995, Nature, 378, 355

McDonough, W. F., & Sun, S. s. 1995, Chemical Geology, 120, 223

McGovern, P. J., & Schubert, G. 1989, Earth and Planetary Science Letters, 96, 27

McIntyre, S. R. N. 2022, A&A, 662, A15

Melbourne, K., Youngblood, A., France, K., et al. 2020, AJ, 160, 269

Miyazaki, Y., & Korenaga, J. 2022, Astrobiology, 22, 713

Moore, K., & Cowan, N. B. 2020, MNRAS, 496, 3786

Moore, K., Cowan, N. B., & Boukaré, C.-É. 2023, MNRAS, 526, 6235

Mulders, G. D., Pascucci, I., & Apai, D. 2015, ApJ, 798, 112

Nakajima, S., Hayashi, Y.-Y., & Abe, Y. 1992, Journal of the Atmospheric Sciences, 49, 2256

Nakayama, A., Kodama, T., Ikoma, M., & Abe, Y. 2019, MNRAS, 488, 1580

Noack, L., & Breuer, D. 2014, Planet. Space Sci., 98, 41

O'Brien, D. P., Izidoro, A., Jacobson, S. A., Raymond, S. N., & Rubie, D. C. 2018, Space Sci. Rev., 214, 47

O'Neill, C., & Lenardic, A. 2007, Geophys. Res. Lett., 34, L19204

O'Rourke, J. G. 2020, Geophys. Res. Lett., 47, e86126

Owen, J. E., & Wu, Y. 2017, ApJ, 847, 29

Papale, P. 1997, Contributions to Mineralogy and Petrology, 126, 237

—. 1999, American Mineralogist, 84, 477

Paradise, A., Menou, K., Lee, C., & Fan, B. L. 2022, MNRAS, 512, 3616

Pass, E. K., Charbonneau, D., Irwin, J. M., & Winters, J. G. 2022, ApJ, 936, 109

Pearson, D. G., Brenker, F. E., Nestola, F., et al. 2014, Nature, 507, 221

Pecaut, M. J., & Mamajek, E. E. 2013, ApJS, 208, 9

Peixoto, J. P., & Oort, A. H. 1992, Physics of climate (American Institute of Physics)

Peterson, M. S., Benneke, B., Collins, K., et al. 2023, Nature, 617, 701

Petrovich, C. 2015a, ApJ, 805, 75

—. 2015b, ApJ, 799, 27

Pierrehumbert, R. T. 2010, Principles of Planetary Climate (Cambridge University Press)

Ranjan, S., Wordsworth, R., & Sasselov, D. D. 2017, ApJ, 843, 110

Raymond, S. N., O'Brien, D. P., Morbidelli, A., & Kaib, N. A. 2009, Icarus, 203, 644

Raymond, S. N., Quinn, T., & Lunine, J. I. 2004, Icarus, 168, 1

Raymond, S. N., Scalo, J., & Meadows, V. S. 2007, ApJ, 669, 606

Reese, C. C., Solomatov, V. S., & Moresi, L. N. 1998, J. Geophys. Res., 103, 13643

Ribas, Á., Merín, B., Bouy, H., & Maud, L. T. 2014, A&A, 561, A54

Ribas, I., Gregg, M. D., Boyajian, T. S., & Bolmont, E. 2017, A&A, 603, A58

Ribas, I., Guinan, E. F., Güdel, M., & Audard, M. 2005, ApJ, 622, 680

Ribas, I., Bolmont, E., Selsis, F., et al. 2016, A&A, 596, A111

Rimmer, P. B., Xu, J., Thompson, S. J., et al. 2018, Science Advances, 4, eaar3302

Robinson, T. D., Meadows, V. S., & Crisp, D. 2010, ApJ, 721, L67

Sabotta, S., Schlecker, M., Chaturvedi, P., et al. 2021, A&A, 653, A114

Salvador, A., & Samuel, H. 2023, Icarus, 390, 115265

Samuel, H., Ballmer, M. D., Padovan, S., et al. 2021, Journal of Geophysical Research (Planets), 126, e06613

Sanchez-Lavega, A. 2011, An Introduction to Planetary Atmospheres (Taylor & Francis)

Sandu, C., Lenardic, A., & McGovern, P. 2011, Journal of Geophysical Research (Solid Earth), 116, B12404

Scalo, J., Kaltenegger, L., Segura, A. G., et al. 2007, Astrobiology, 7, 85

Schaefer, L., & Fegley, B. 2010, Icarus, 208, 438

Schaefer, L., & Sasselov, D. 2015, ApJ, 801, 40

Schaefer, L., Wordsworth, R. D., Berta-Thompson, Z., & Sasselov, D. 2016, ApJ, 829, 63

Schubert, G., Turcotte, D. L., & Olson, P. 2001, Mantle Convection in the Earth and Planets (Cambridge University Press)

Seales, J., & Lenardic, A. 2021, Icarus, 367, 114560

Shah, O., Alibert, Y., Helled, R., & Mezger, K. 2021, A&A, 646, A162

Shields, A. L., Ballard, S., & Johnson, J. A. 2016, Phys. Rep., 663, 1

Sleep, N. H., & Zahnle, K. 2001, J. Geophys. Res., 106, 1373

Solomon, S. C. 1979, Physics of the Earth and Planetary Interiors, 19, 168

Sousa-Silva, C., Seager, S., Ranjan, S., et al. 2020, Astrobiology, 20, 235

Spaargaren, R. J., Ballmer, M. D., Bower, D. J., Dorn, C., & Tackley, P. J. 2020, A&A, 643, A44

Stamenković, V., Noack, L., Breuer, D., & Spohn, T. 2012, ApJ, 748, 41

Stixrude, L., Scipioni, R., & Desjarlais, M. P. 2020, Nature Communications, 11, 935

Taylor, F. 2010, Planetary Atmospheres (OUP Oxford)

Tian, F. 2009, ApJ, 703, 905

Tian, F., Kasting, J. F., Liu, H.-L., & Roble, R. G. 2008, Journal of Geophysical Research (Planets), 113, E05008

Turbet, M., Bolmont, E., Chaverot, G., et al. 2021, Nature, 598, 276

Turbet, M., Ehrenreich, D., Lovis, C., Bolmont, E., & Fauchez, T. 2019, A&A, 628, A12

Turcotte, D. L., & Schubert, G. 2002, Geodynamics (Cambridge University Press)

Valencia, D., O'Connell, R. J., & Sasselov, D. 2006, Icarus, 181, 545

van Thienen, P., Benzerara, K., Breuer, D., et al. 2007, Space Sci. Rev., 129, 167

Veras, D., Carter, P. J., Leinhardt, Z. M., & Gänsicke, B. T. 2017a, MNRAS, 465, 1008

Veras, D., Georgakarakos, N., Dobbs-Dixon, I., & Gänsicke, B. T. 2017b, MNRAS, 465, 2053

Walker, J. C. G. 1977, Evolution of the atmosphere (Macmillan)

Walker, J. C. G., Hays, P. B., & Kasting, J. F. 1981, J. Geophys. Res., 86, 9776

Walterová, M., Běhounková, M., & Efroimsky, M. 2023, arXiv e-prints, arXiv:2301.02476

Watson, A. J., Donahue, T. M., & Walker, J. C. G. 1981, Icarus, 48, 150

West, A. A., Bochanski, J. J., Hawley, S. L., et al. 2006, AJ, 132, 2507

Wetherill, G. W. 1990, Annual Review of Earth and Planetary Sciences, 18, 205

Williams, D. R., & Pan, V. 1992, J. Geophys. Res., 97, 8937

Wolszczan, A., & Frail, D. A. 1992, Nature, 355, 145

Wood, J. A., Dickey, J. S., J., Marvin, U. B., & Powell, B. N. 1970, Geochimica et Cosmochimica Acta Supplement, 1, 965

Wordsworth, R., & Pierrehumbert, R. 2014, ApJ, 785, L20

Wordsworth, R. D., & Pierrehumbert, R. T. 2013, ApJ, 778, 154

Wordsworth, R. D., Schaefer, L. K., & Fischer, R. A. 2018, AJ, 155, 195

Yamashiki, Y. A., Maehara, H., Airapetian, V., et al. 2019, ApJ, 881, 114

Yang, J., Cowan, N. B., & Abbot, D. S. 2013, ApJ, 771, L45

Yoshida, T., Terada, N., Ikoma, M., & Kuramoto, K. 2022, ApJ, 934, 137

Youngblood, A., France, K., Loyd, R. O. P., et al. 2016, ApJ, 824, 101

Zieba, S., Kreidberg, L., Ducrot, E., et al. 2023, Nature, 620, 746